ENDOLUMINAL COILS FOR INTERVENTIONAL MRI PROCEDURES

A THESIS

SUBMITTED TO THE DEPARTMENT OF ELECTRICAL AND ELECTRONICS ENGINEERING

AND THE INSTITUTE OF ENGINEERING AND SCIENCES

OF BILKENT UNIVERSITY

IN PARTIAL FULLFILMENT OF THE REQUIREMENTS

FOR THE DEGREE OF

MASTER OF SCIENCE

By

V. Nikolay Viskuşenko

September 2010

I certify that I have read this thesis and that in my opinion it is fully adequate, in scope and in quality, as a thesis for the degree of Master of Science.

Prof. Dr. Ergin Atalar (Supervisor)

I certify that I have read this thesis and that in my opinion it is fully adequate, in scope and in quality, as a thesis for the degree of Master of Science.

Prof. Dr. Y. Ziya İder

I certify that I have read this thesis and that in my opinion it is fully adequate, in scope and in quality, as a thesis for the degree of Master of Science.

Prof. Dr. A. Muhteşem Ağıldere

Approved for the Institute of Engineering and Sciences:

Prof. Dr. Levent Onural

Director of Institute of Engineering and Sciences

ABSTRACT

ENDOLUMINAL COILS FOR INTERVENTIONAL MRI PROCEDURES

V. Nikolay Viskuşenko
M.S. in Electrical and Electronics Engineering
Supervisor: Prof. Dr. Ergin Atalar

September 2010

In this study we designed endoluminal magnetic resonance imaging (MRI) coils to be used for interventional procedures under the guidance of MRI. The first coil we developed is a two-channel endocervical coil for the treatment of cervical cancer. The coil was embedded into the brachytherapy applicator without interfering with its functions. It provides magnetic resonance (MR) images of the cervix with high signal-to-noise ratio (SNR) that is required for a more accurate radiation dose calculation in the treatment of cervical cancer with high dose rate brachytherapy (HDRB). The performance of this coil was tested with phantom experiments and the results proved that the design worked properly.

Second, we developed an MRI guidewire and an MR EP catheter for the treatment of atrial fibrillation (AF). The MRI guidewire had similar mechanical properties with the common cardiovascular guidewires and it was proved successful in obtaining high SNR images of the heart. The MR EP catheter could also provide high SNR images as well as clean intracardiac electrocardiogram (IECG) signal during the MR scan. Due to the loopless antenna embedded inside both of these catheters, they could be navigated in the body under the MRI. They may be used to guide complex interventional procedures such as RF ablation. The performance of these catheters was tested and confirmed with in *vitro* experiments.

To sum up, these two technologies can play a significant role in the treatment of cervical cancer and AF as well as contributing to the development of interventional MRI.

Keywords: MRI, endoluminal coils, endocervical coil, Atrial Fibrillation (AF). Interventional MRI, Intracardiac Electrocardiogram (IECG), High Dose Rate Brachytherapy (HDRB).

ÖZET

MRG PROSEDÜRLERI İÇİN VÜCUT BOŞLUKLARINA GİREBİLEN SARGILAR

V. Nikolay Viskuşenko
Elektrik ve Elektronik Mühendisliği Yüksek Lisans
Tez Yöneticisi: Prof. Dr. Ergin Atalar

Eylül 2010

Bu tez çalışmasında MRG gözetiminde girişimsel prosedürlerin gerçekleştirilebilmesi için vücut boşluklarına girebilen sargılar üretilmiştir. İlk olarak serviks kanseri tedavisinde kullanılmak üzere iki kanallı endoservikal manyetik rezonans (MR) sargısı tasarlanmıştır. Bu sargı brakiterapi aplikatörünün içine (onun asli fonksiyonlarını etkilemeden) yerleştirilmiştir ve böylelikle yüksek doz hızlı brakitherapy yöntemi kullanılarak yapılan serviks kanseri tedavileri için yüksek çözünürlükte MR görüntüleri sağlamıştır. Bu görüntüler daha doğru radyasyon doz hesaplamalarının yapılmasında kullanılmıştır. Bu sargının performansı fantom deneyleriyle test edilmiş ve sargının doğru bir şekilde çalıştığı gösterilmiştir.

İkinci olarak, Atrial Fibrilasyon (AF) hastalığının MRG kılavuzluğunda gerçekleştirilebilmesi için MRG kılavuz teli ve MR elektrofizyoloji (EF) ölçüm kateteri geliştirilmiştir. Geliştirilen MRG kılavuz teli piyasada yaygın olarak kullanılan kardiovasküler kılavuz telleriyle benzer mekanik özellikler taşımakta ve kalbin yüksek çözünürlükte MR görüntülerinin alınmasını sağlamaktadır. Geliştirilen MR EF ölçüm kateteri MR cihazı çalışıyorken kalbin yüksek çözünürlükte görüntülenmesini ve aynı anda kalbin içinden temiz bir EKG

sinyalinin elde edilebilmesini sağlamaktadır. Bu kateterlerin içine yerleştirilen sargısız anten sayesinde bu kateterler vücut içerisinde navige edilebilmektedir. Bu kateterler Radyo Frekans (RF) ablasyonu gibi karmaşık girişimsel MRG prosedürleri için de kullanılabilir. Bu kateterlerin performansları insan modeli deneyleriyle test edilmiş ve bu kateterlerin doğru bir şekilde çalıştıkları gösterilmiştir.

Özetle, bu iki yeni teknoloji serviks kanseri ve AF hastalıklarının tedavisinde önemli bir rol oynayabilir ve girişimsel MRG'nin gelişmesine katkıda bulunabilir.

ACKNOWLEDGEMENTS

First and foremost I offer my sincerest gratitude to my supervisor, **Prof. Dr. Ergin Atalar,** who supports me in every stage of my Master's study. Beyond his gracious academic support, he supports me in every stage of my life being not only an excellent supervisor but also a very good friend. I attribute the level of my Master degree to his encouragement and effort, and without him I would never be able to complete this thesis. Besides all, he taught me how to be a decent man. One simply could not wish for a better or friendlier supervisor.

I owe my deepest gratitude to **Aslıhan Örs,** without her endless support I would never be able to finish this thesis. She supports and encourages me in my most difficult times. Her excellent English increase the quality of this thesis. It is a big pleasure to know such a fantastic person and friend who is always ready to help me. I could not thank you enough.

My grateful thanks to Mr. Sinan Kobaoğlu and the entire staff of the Ministry of Industry for providing the financial support. Without their support, it wouldn't be possible to startup this project.

I would also like to thank Muratcan Alkan, for his endless help and support in writing my thesis. Without his amazing help I would never shape this thesis.

I would like to thank Prof. Dr. Yusuf Ziya İder and Prof. Dr. Ahmet Muhteşem Ağıldere for accepting to evaluate my thesis and to be a member of my jury.

My special thanks go to Emre Kopanoğlu for providing me academic support during my thesis. I would also like to express my sincere gratitude to Selman Özbayatlı, Volkan Açıkel, Yiğitcan Eryaman and all the technical and academic staff at the National Magnetic Resonance Research Center (UMRAM) for their great assistance and support during this project.

I would like to thank all the people that contributed with their expertise and work to the realization of this research. Especially I want to thank Dr. Özcan Ertürk and all the Bayındır Hospital staff, particularly the "Radiology Department" for providing me access to the MR scanner.

My special thanks go to Dr. Oktay Algın, Doç. Dr. Çağdaş Oto and the entire staff of Ankara University Faculty of Veterinary Medicine for offering their support for the animal experiments.

Most importantly I would like to thank my mom whom I owe everything in my life. Thank you very much for believing in me whatever it was and supporting me in all stages of my life.

Table of Contents

List of Figures

Chapter 1

1. INTRODUCTION

The Magnetic Resonance Imaging (MRI) has been regarded as one of the most preferred imaging techniques for the past 20 years. MRI relies on the fact that the hydrogen atoms (with some few other atoms having an odd mass or odd atomic number) found in the human tissues resonate under a large and uniform static magnetic field. Under this static field, the spins of the hydrogen atom aligns with the main magnetic field. The excitation with a radio-frequency (RF) pulse disturbs the alignment of the spins and they return to their original position by precessing about the axis of the main magnetic field. During this process, they emit an RF signal at a certain frequency called Larmor frequency. Using an RF receiver coil, the MRI instrument receives this signal and then converts it to an MR image. Therefore, the quality of the MR image is strictly dependent on the performance of the RF coil.

MRI has a lot of advantages over the other imaging modalities. It provides high quality soft tissue contrast and thus it is especially beneficial for the visualization of brain, cardiovascular and cancer tissue imaging. The MRI also doesn’t have any known permanent side effects on the patients and the physicians, since image acquisition by the MRI does not involve ionizing radiation.

The advantages of the MRI make it a promising technology for image guided interventional procedures. Although today usage of MRI in guiding interventional procedures (this is called interventional MRI) is uncommon in clinical practice, its popularity is expected increase in the near future. Interventional MRI enables accurate navigation and image guidance during the minimally invasive operations. Hence, with the advancements in the interventional MRI technology, the surgeons will be able to conduct very difficult surgical operations with the visual help of the MRI. With accurate navigation, the surgical instruments can be delivered safely into the deep locations of the body; and with the image guidance, lesions can be safely removed (ablated) without harming healthy tissues. One of the current problems in the interventional MRI is to accurately localize surgical or treatment devices such as catheters or radioactive leads inside the body. Different studies have been conducted to address this issue.

In 1997, Ocali and Atalar used a loopless antenna based cardiovascular coil for navigation of the catheter inside the arterial vessels [1]. This catheter antenna is essentially a dipole antenna, which is a coaxial cable with extended inner conductor. The design of this structure makes it possible to construct the antenna with a very small diameter. Its electrical circuitry was placed outside the blood vessels without any performance loss. Images of the abdominal aorta of a canine, obtained by a loopless antenna are shown in Figure 1. This catheter provides high SNR images of the local region in the cardiovascular system, which can also be used to guide the electrophysiological procedures by imaging the ablation lesions.

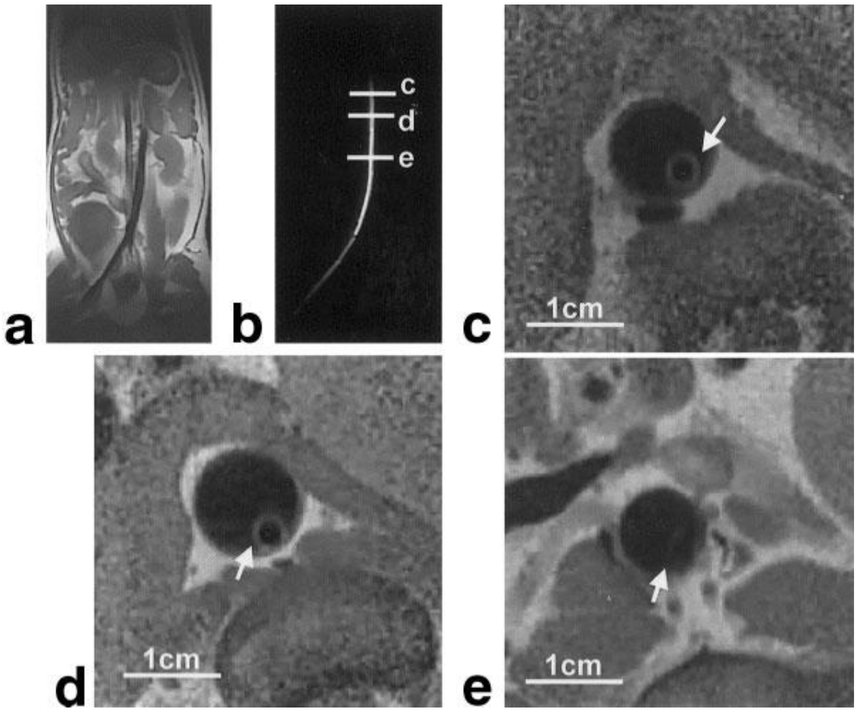

Figure 3 (a) anatomical scout image obtained by a surface phased array coil (b) projection image obtained by a loopless antenna (c-e) axial FSE images obtained without moving the imaging antenna (This image is taken from [37] with the permission of the author)

In 2004, Susil et al., developed an interventional MRI technique for high-dose-rate prostate brachytherapy and needle biopsy in a conventional MRI scanner. The device allowed taking a biopsy sample from specific sites within the prostate that were accurately registered with the MR image data. And at the same time, it provided accurate MR-image guided placement of brachytherapy treatment catheters.

Although interventional MRI coils could be used alone, they can also be used in combination with other internal or external coils. In 2003, Yung [2] used four channel arrays, one as a surface coil, two as endorectal coils and one as a flexible endourethral coil for the MRI of canine prostate. Figure 2 shows an imaging of the canine prostate obtained by 4 channel phased array coils.

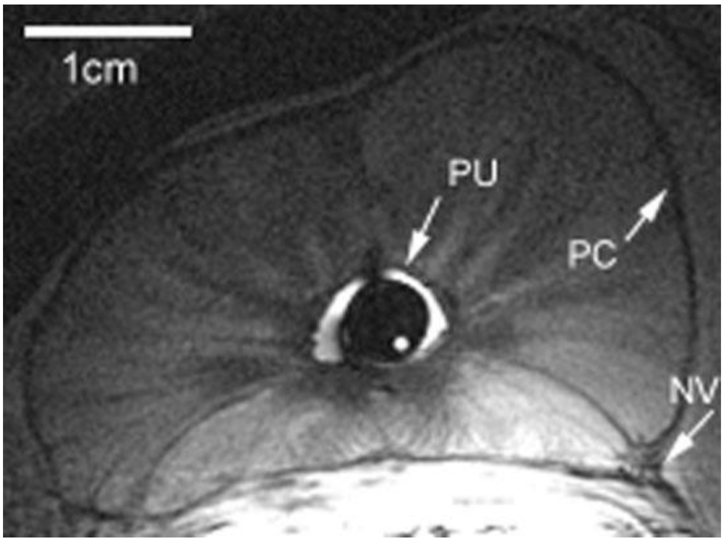

Figure 4: Axial image of a dog prostate using the flexible endourethral loop coil and dual-coil endorectal probe. (This image was taken from [2] with the permission of the author).

In this study we developed MRI coils for interventional procedures to be used in the treatment of cervical cancer and atrial fibrillation (AF). These two common diseases pose some challenges in the process of treatment. In case of cervical cancer treatment with HDR brachytherapy, accurate radiation dose calculation is only possible with precise visualization of the tumors. Currently available imaging techniques do not provide sufficient imaging quality for this procedure. To this end, we developed a two channel endocervical coil, which could be embedded into the brachytherapy applicator without interfering with its function and provide high quality MR images for accurate radiation dose calculation Moreover, since the images are obtained while the applicator is in place, the inaccuracies caused by the replacement of the tumor during the insertion of the applicator is eliminated. In case of the AF treatment, X-Ray fluoroscopy guided ablation is the most prevalent technique nowadays. However, because of the poor visualization of soft tissues, difficulties are experienced in creating linear and continuous lesions. Hence, we designed electrophysiological (EP) catheters for MRI guided procedures. The catheters not only provide high quality images but also navigate the treatment.

Chapter 2

2. TWO CHANNEL ENDOCERVICAL COIL FOR HIGH DOSE RATE BRACHYTHERAPY (HDRB)

2.1 INTRODUCTION

2.1.1 Cervical cancer

Cervical cancer is a very common disease in the developing countries despite its low incidence in Western Europe and North America [3]. Furthermore, an increase in rapidly growing tumors was noticed among young women in recent years [4]. Human papilloma virus is the major cause of the cervix cancer, which is observed in 90% of the women with the disease [5]. The most important prognostic factors of the cervical cancer are tumor size, tumor extension, and nodal involvement [6].

The cervix is located in the lower part of the uterus between the bladder and rectum and connected to the pelvic soft tissues and bones by several ligaments and muscles. The cervix has a central orifice (the external os) with an anterior and a posterior lip, and an internal orifice (isthmus) with the endocervical canal between the two (Figure 2.1). The diameter of the cervix varies from 2 to 5 cm, with a width of 2.5 to 5 cm and a thickness of 2 to 4 cm. Its length varies from 2 and 5 cm (as the length of the endocervical canal). The length of the uterine cavity varies somewhere between 4 to 10 cm [7].

The whole uterus including the cervix and the vaginal wall are densely vascularized and their tolerance to radiation is very high. In contrast, critical organs which are directly adjacent to the cervix like the rectum or the bladder are more radiosensitive. In some cases, the highly radiosensitive small and large bowel (sigmoid) may be in direct contact with the uterine wall as well. The vagina must also be considered as an organ at risk [7].

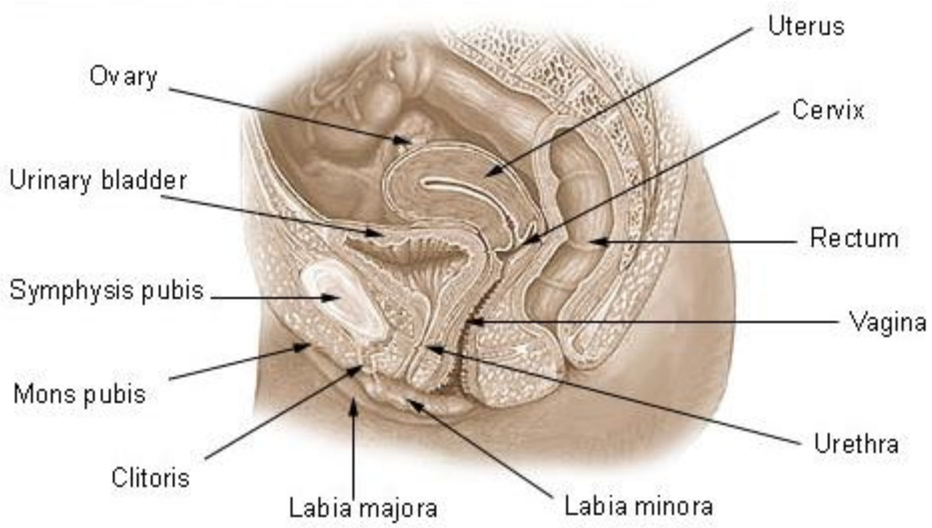

Figure 2.1: An image showing organs of female reproductive system (This image is taken from Wikipedia).

2.1.2 Treatment Methods

Depending on the stage of the disease, hysterectomy (surgical removal of the uterus and cervix), radiotherapy (radioactive source treatment) and chemotherapy (treatment of disease by chemicals) methods are used to treat cervical cancer. It is suggested to use concentrated radiotherapy such as High Dose Rate (HDR) brachytherapy if the disease has not spread to the whole body.

Brachy is Greek word for “short distance” and brachytherapy, also known as internal radiotherapy, means delivering the radiation sources inside or next to the target region. The radiation sources are placed directly or with endoluminal applicator at the site of the cancerous tumor. This placement ensures that only the localized region will be affected by the radiation and the healthy tissues are kept away from the radiation. This principle is the main advantage of brachytherapy over the external beam therapy [8,9].

During the application of HDR brachytherapy, radio-oncologists are interested in working with images of the cervix with as much SNR and resolution as possible, to increase the accuracy of the radiation dose planning. Computer Tomography (CT) imaging method, which is widely used nowadays, does not provide sufficient imaging quality to serve this purpose [10,11]. Even though MRI does not provide the ideal resolution for radiation dose planning, this technique provides the best imaging contrasts [12]. In a study of radiation dose calculation for the treatment of cervical cancer, images obtained from MRI and CT were compared and CT was found to show the region of treatment erroneously large [13]. Despite being more reliable than the CT image, the resolution of the MRI images does not have the optimum resolution due to the existence of external coils in MRI [14]. Furthermore, it is favorable to obtain the images of the region while the applicator is in place. Hence, we designed a two-channel RF coil, which is embedded inside a commercially available cervical applicator, enabling high resolution imaging of cervix.

The Nucletron (Veenendaal, Netherlands) CT-MR ring applicator, which consists of a loop and a tandem applicator, is developed for the cervical brachytherapy procedure (Figure 2.2). In brachytherapy procedures, the loop applicator is located adjacent to the cervix and the tandem applicator goes through the loop into the cervix. In this study, however, the applicator was modified by placing a loop coil inside the loop applicator. A loopless coil [1] is inserted into the tandem applicator during the MRI, which can be later removed during the brachytherapy, leaving its place to the radiation source.

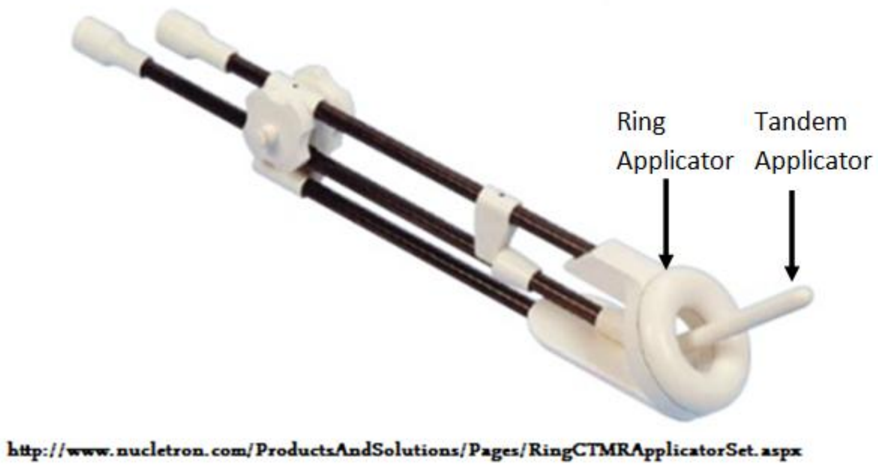

Figure 2.2: The Nucletron (Veenendaal, Netherlands) CT-MR ring applicator, which is developed for the gynecologic brachytherapy procedures. The applicator is MR-compatible. Composite fiber tubing and plastics were used in its design to eliminate distortion on CT or MR imaging.

2.2 THEORY

2.2.1 Loop Coil

Loop coils can be used in various applications. They can be used as surface coils or they can be inserted into the vessels or body cavities if built in small diameter. The small loop coils not only enable access to the body cavities but also increase the SNR [15]. In the first step of a loop coil preparation, a loop is tuned to a desired frequency and then matched. Next, this coil is decoupled from the transmit coil via an active decoupling circuit. And finally, with the construction of a balun circuit to prevent unbalanced currents, the loop coil is ready to be used in the MRI scan.

A magnetic field distribution of the loop coil is shown in Figure 2.3. Although the anatomical structure of the cervix varies from patient to patient, the most common place for the loop coil is when its surface normal is parallel to the static magnetic field. In that situation, a null region occurs in front of the loop which coincides with the region of interest. Despite this null region, however, the coil provides sufficiently high SNR in the image. A small experiment was conducted in order to prove this phenomenon. In Figure 2b, the null region of the loop coil is depicted. The image at the left was obtained using a loop coil with 4cm in diameter, which is placed inside a saline solution so that surface of the coil is perpendicular to static magnetic field.

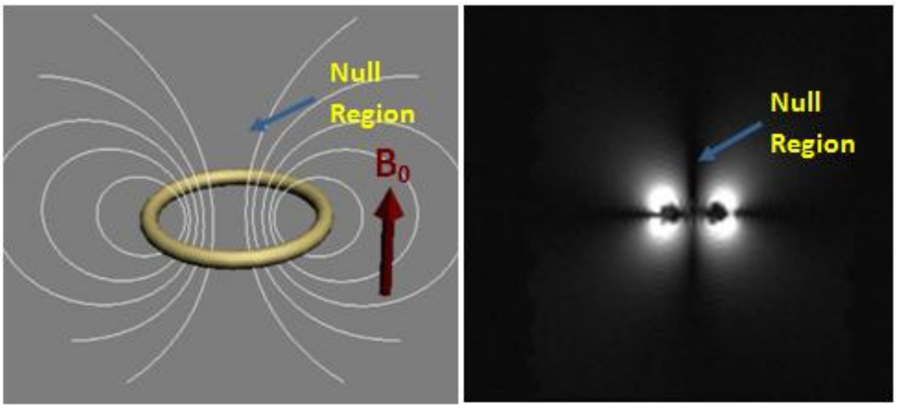

Figure 2.3: The left image gives a simple drawing of the field distribution of the loop coil when it is placed in a way that its surface normal would be parallel to the static magnetic field. The right image gives a simple MR image obtained by a simple loop under the explained condition. The null region in the image could be easily observed.

It is assumed that during the reception of the free induction decay (FID), signal induced currents on the loop has a uniform distribution along the loop. Then, the reciprocity principle was used to obtain sensitivity map of the coil [16]. A uniform current distribution assumed on the coil and magnetic field distribution was calculated. Then sensitivity map is obtained using the transverse components of the field. In Figure 2.4 a simple model problem is depicted. The magnetic field created at an arbitrary point P(x,y,z) by a differential current element with length *dl*, is calculated as follows [17].

$$\boldsymbol{B_x} = \frac{C\,x\,z}{2\,\alpha^2\,\beta\,\rho^2}[(\alpha^2 + r^2)\,E(k^2) - \alpha^2 K(k^2)] \tag{1}$$

$$\boldsymbol{B_y} = \frac{C\, y\, z}{2\, \alpha^2\, \beta\, \rho^2}[(\alpha^2 + r^2)\, E(k^2) - \alpha^2 K(k^2)] = \boldsymbol{B_x}\frac{\boldsymbol{y}}{\boldsymbol{x}} \qquad (2)$$

$$\boldsymbol{B_z} = \frac{C}{2\, \alpha^2\, \beta}[(\alpha^2 - r^2)\, E + \alpha^2 K(k^2)] \qquad (3)$$

Where E and K are elliptic integrals,$C\ = \frac{\mu_{\circ} I}{\pi}$, $\rho^2 = x^2 + y^2$, $r^2\ = x^2 + y^2 + z^2$, $\alpha^2 = a^2 + r^2 - 2a\rho$, $\beta^2 = a^2 + r^2 + 2a\rho$. The magnetic field intensity is calculated from the B field ($H = \frac{B}{\mu}$).

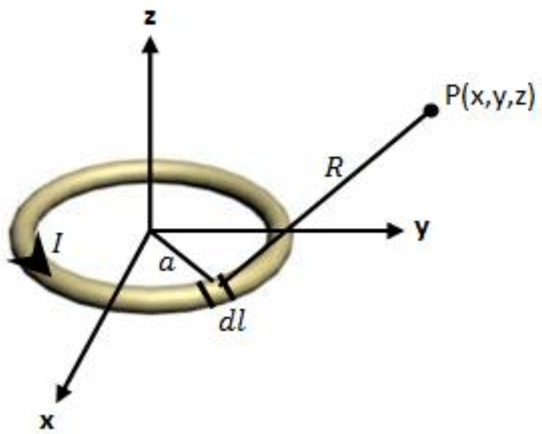

Figure 2.4: A simple drawing showing the magnetic field composed dl at the arbitrary P(x,y,z) point.

Using the calculation above, the magnetic field intensity of the loop coil with a 4 cm diameter was plotted using MatLab (MathWorks, Natick, MA). The simulation results are shown in Figure 2.5. This simulation was obtained in collaboration with Hüseyin Kılınç.

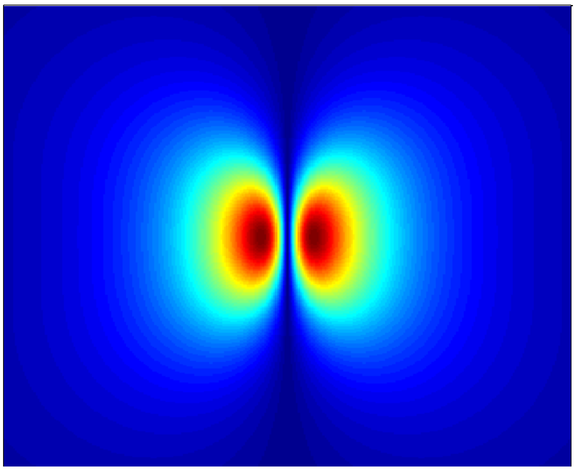

Figure 2.5: Transverse field profiles of a loop coil with a 4 cm diameter, which is placed in a way that the surface normal of the loop would be in the static field direction. The field-of-view (FOV) of the image is 25cm x 25cm. The coronal plane is obtained 1 cm away from the center of the loop coil.

In Figure 2.5, there are regions with very low signal level, which make it quite hard to get a high quality image with the loop coil. Unfortunately, these areas happen to have crucial importance in the cervix imaging. A solution to overcome this problem will be suggested in the following section.

2.2.2 Loopless Coil

A loopless antenna is a coaxial cable with an extended inner conductor. Matching and active decoupling circuits are placed at the proximal end of the coaxial cable. This enables placement of loopless coils inside catheters. A loopless coil is highly sensitive to its vicinity along the catheter shaft as seen in Figure 2.6-a. Similar to the straight wire antenna (18), its sensitivity is inversely proportional to the distance from the antenna [1]. Figure 2.6-b is obtained with a loopless coil which is placed inside a saline solution in the direction of the main magnetic field. As expected, the signal intensity around the loopless coil rapidly decreases with distance as in Figure 2.6-b.

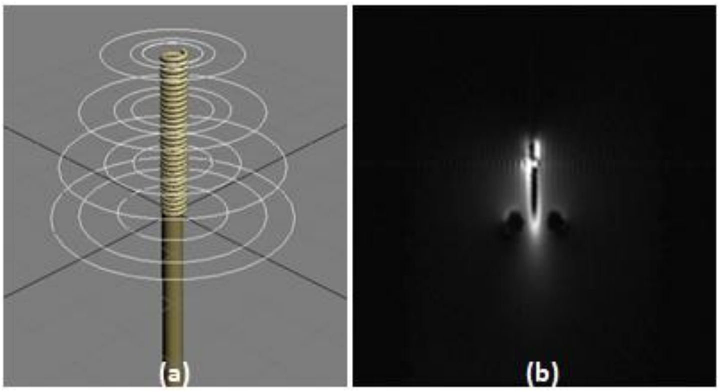

Figure 2.6: a. A simple drawing of magnetic field distribution of the loopless coil. b. MR image of the loopless antenna inside the phantom filled with saline solution.

The structure of a loopless antenna is similar to a straight wire antenna, thus it can be modeled as a simple straight wire. Sensitivity of a loopless coil can be found in a similar way as in the previous section. Assuming a uniform current distribution along the coil, H-field is given by:

$$H = \frac{\mu_{\circ} I}{4 \mu \pi} \oint \frac{dl \times R}{R^3} \quad (4)$$

where R is the distance between the observation point P(x,y,z) and incremental source length dl(Figure 2.7).

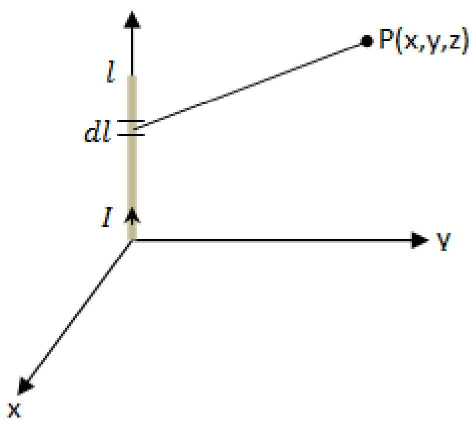

Figure 2.7: Calculation of magnetic field of a rod, of length *l* lying on z axis, on an arbitrary point P

Equation 4 gives the magnetic field intensity of a simple rod everywhere. As the sensitivity is proportional to $|H_x + jH_y|$, transverse component of the magnetic field is utilized to obtain the sensitivity map as in Figure 2.8.

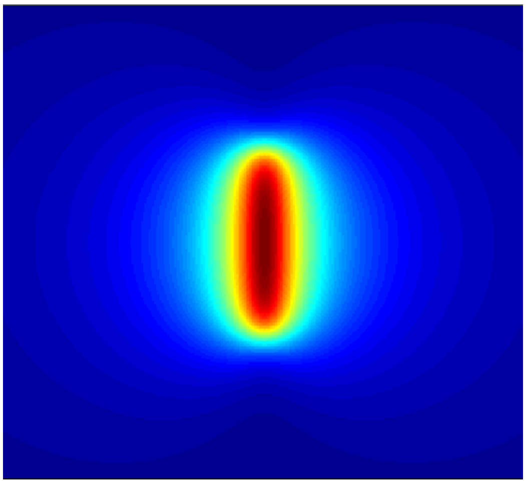

Figure 2.8: Sensitivity map of a loopless coil in coronal plane.

In close proximity, the loopless antenna creates a magnetic field that is strong enough to obtain high quality images. However, as the distance increases, strength of the field decreases with 1/r.

2.2.3 Combined Structure of Loop and Loopless Coils

When the axis of the loop is along the z-direction the loop coil has sufficiently high sensitivity, however, it also has an important disadvantage- a null region at the center of the loop. Since the loop center is placed parallel to the cervix, this null region coincides with the cervix wall and causes data loss. In order to collect the data in the null region a loopless coil is placed through the center of the loop coil inside the cervix and a combined structure is obtained. Figure 2.9-a depicts a simple figure that shows the magnetic field distribution of the combined structure. Figure 2.9-b gives an MR image of the combined structure in a saline phantom. It could easily be seen that the loopless antenna compensates the nullity.

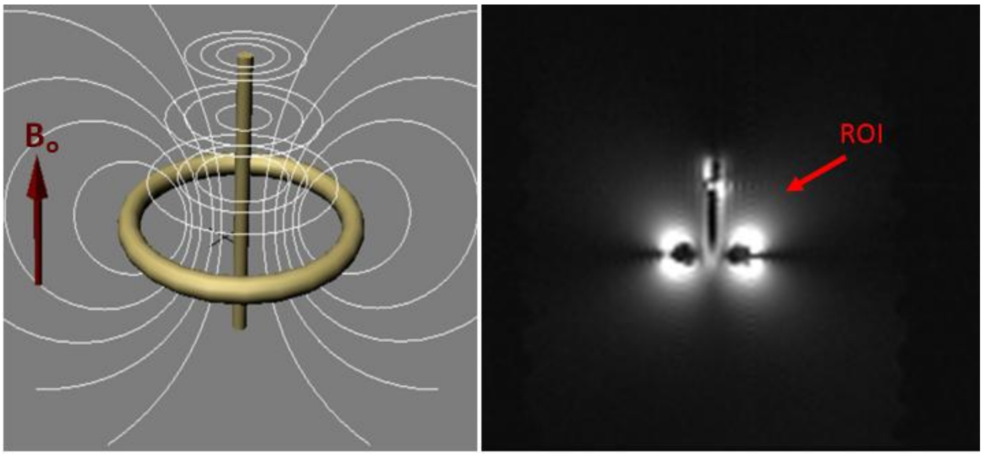

Figure 2.9: a. The magnetic field distribution of combination of loop and loopless coils. b. A simple MR image of the combined coil structure inside a phantom filled with saline solution. The ROI is the assumed place of the cervix. Loopless antenna compensates the null region of the loop coil.

Figure 2.10 shows the simulation results of a combined structure. The result again shows that the loopless coil compensates the null region of the loop coil.

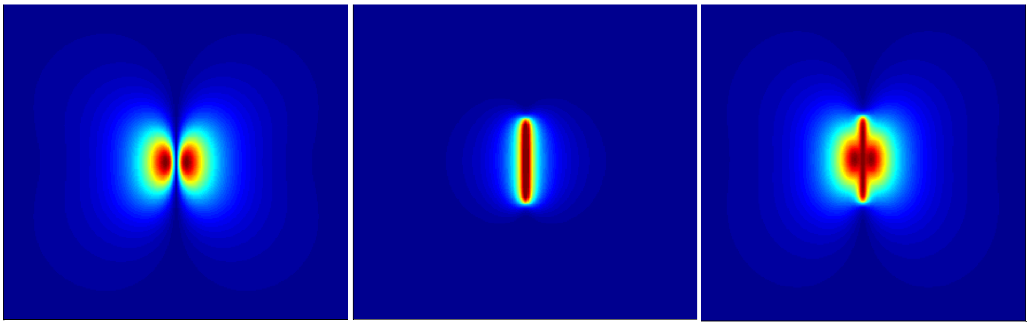

Figure 2.10: a: Simulation results of a loop coil placed in such a way that its surface normal would be parallel to the static magnetic field. b: Simulation result of loopless coil. c: simulation results of a combined structure of loop and loopless coil.

2.3 MANUFACTURING PRINCIPLES OF TWO CHANNEL ENDOCERVICAL COIL

2.3.1 Loop Coil

In this chapter, the production steps of a loop coil, which is manufactured for the Endocervical MRI probe, are explained. Most MRI coils have similar parts such as balun, matching-tuning and decoupling circuitry that are required for the coils to be used in an MRI scanner safely. These parts, their implementations and their functions are explained in detail in this chapter.

The design of a loop coil starts with the investigation of the loop portion of the Nucletron CT-MR ring applicator (Figure 2.11) which is developed for gynecologic brachytherapy procedures. This non-metallic applicator is designed using composite fiber tubing in order to eliminate distortions on CT or MR images. Commercially, there are 3 main versions of this applicator. The main difference between these versions is the angle of the distal end which could be 30, 45 or 60 degrees. Among these three types, 60-degree version is the most widely used one. Hence, 60-degree version is studied in this thesis. The handle of the applicator is 20cm long and the outer diameter of the loop is 38 mm. During the brachytherapy procedure, the applicator is inserted into the vagina such that its surface normal is directed through the cervix canal.

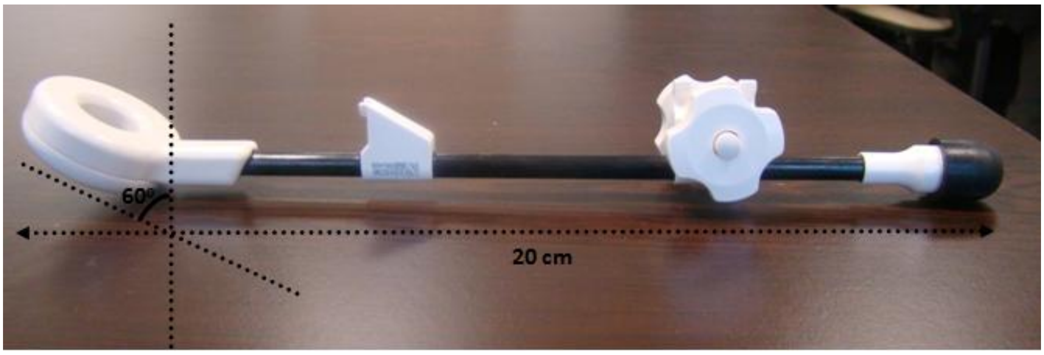

Figure 2.11: a picture of the CT-MR Loop applicator which is developed for gynecologic brachytherapy procedures. The total length of the handle from the distal site to the loop is 20 cm.

Before the loop coil can be designed, the inner structure of the applicator was investigated. As there were no available documents about the inner structure of the applicator, and cutting the applicator randomly was too risky because of its high price, X-Ray was used to investigate the inner structure of the applicator. It was known that the HDR groove extends through the loop portion; hence a 1 mm copper wire was inserted into the groove to make the groove more visible. The applicator was inserted into rubber gloves so that no external material will slip inside. The structure was put into a 15cm-by-15cm rectangular plastic container filled with water and X-Ray images of the structure were obtained. Figure 2.12a shows the obtained image and Figure 2.12b gives a picture of the applicator. In Figure 2.12a, the structure can be seen clearly. The width of the loop is 12mm and relying on observation we realize that there is approximately 7mm blank space between the extension of the radiation groove and the outer wall of the applicator, which is more than enough to place the loop coil. A second image of the applicator, which was transversal, was also obtained (Figure 2.13a) and a side-view picture of the applicator is given in Figure 2.13b. Using a micrometer, the thickness of the loop was measured as 15mm as is clearly seen in Figure 2.13b. The loop consists of two parts, the case and the cap. The thickness of the cap is measured to be 6mm as is shown in Figure 2.13b. By observation, we comment that the groove is approximately 6 mm away from the cap (Figure 2.13a). Hence, the groove is approximately at the intersection plane of the case and the cap. Thus, we decided to cut the loop at this plane. With the help of a CNC machine, the loop was cut into two parts.

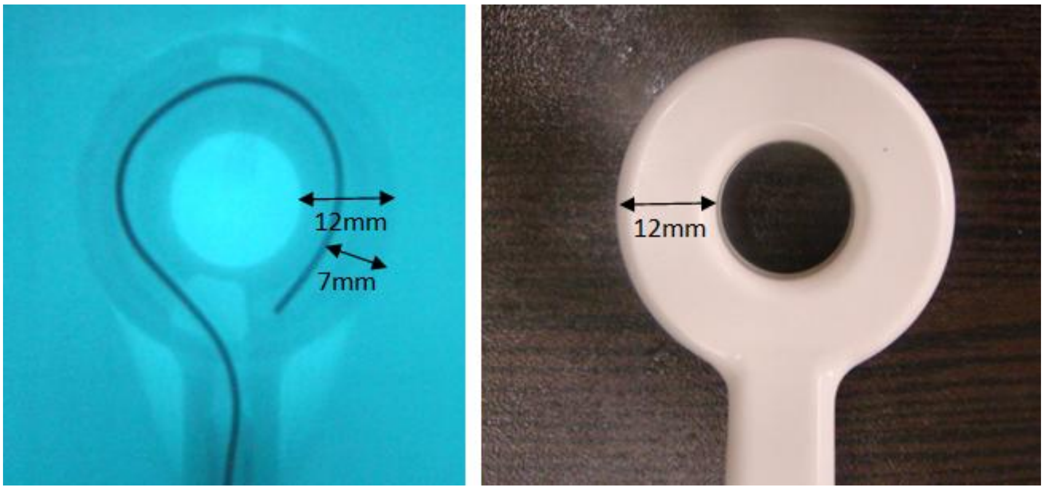

Figure 2.12: a) A coronal X-Ray image of the Nucletron CT-MR ring applicator. b) A coronal picture of the applicator.

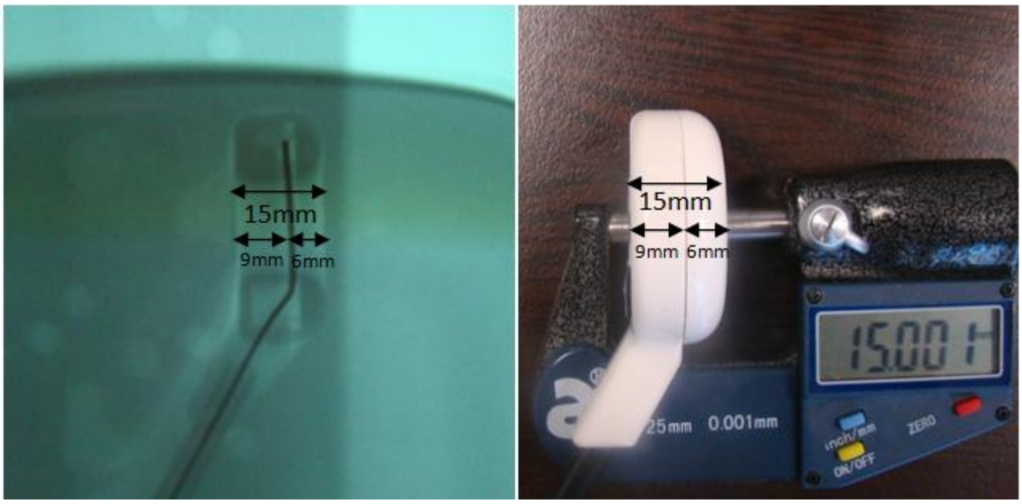

Figure 2.13: a) A transversal X-Ray image of the Nucletron CT-MR ring applicator. b) a coronal picture of the applicator.

After cutting the loop into two parts, a groove was carved for the coil with 1.5mm milling cutter, for which the loop coil was modeled on the applicator using AutoCad. At the distal end of the loop, a 4mm x 4mm x 4mm space was carved for the capacitor. A picture of the resulting structure is given in Figure 2.14.

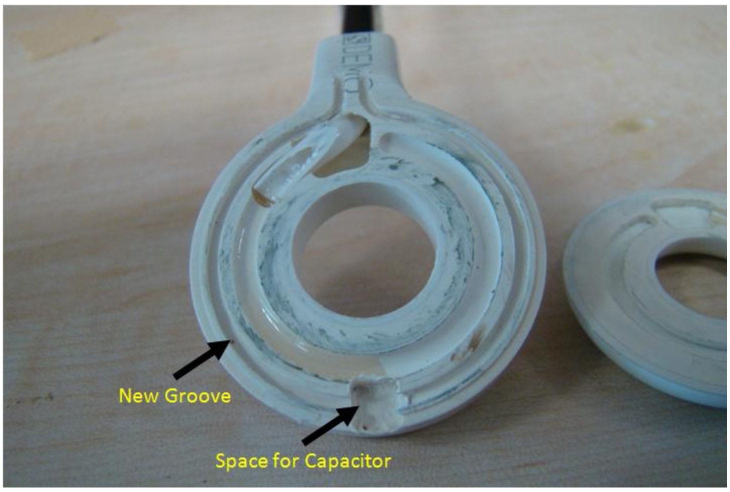

Figure 2.14: a picture of the modified Nucletron CT-MR ring applicator. A new groove of 1.5mm is opened for the loop coil and 4mm x 4mm x 4mm space is opened for the tuning capacitor.

2.3.1.1 CONSTRUCTION OF THE RF LOOP COIL

The RF coil was constructed from a 1mm magnet wire (Newark, Palatine, IL), which has the optimum dimensions considering the space concern caused by the physical features of the applicator. The magnet wire was placed into the groove opened earlier. As mentioned before, the cost of the applicator is very high and we have just one sample in hand. So each time during the tuning, the coil was taken out of the applicator, the capacitor soldered outside of the applicator and then the coil was placed back to the applicator to check its performance. In order to minimize the effect of this procedure on the true shape of the coil, a rigid material is preferable. The wire was placed into the groove and its ends were opened. Then the loop coil was cut in the middle (at the space for the capacitor shown in the Figure 2.14) and ATC B type nonmagnetic tuning capacitors (American Technical Ceramics, NY) were placed. The loop was tuned with two parallel capacitors as shown in Figure 2.15. A stunt matching capacitor (ATC) is placed at the proximal end of the loop. The loop coil was decoupled by placing a small transmission line printed on the PC with one end soldered to the tuning capacitor and the other end soldered with PIN diode. A 3 mm double shield coaxial cable (Suhner, Herisau, Switzerland) with a balun at the proximal end was used to connect the coil to the custom made 2 channel preamplifier interface (UMRAM, Ankara, Turkey). The loop coil was connected to the 3T MR (TIMTrio, Siemens) via this interface box.

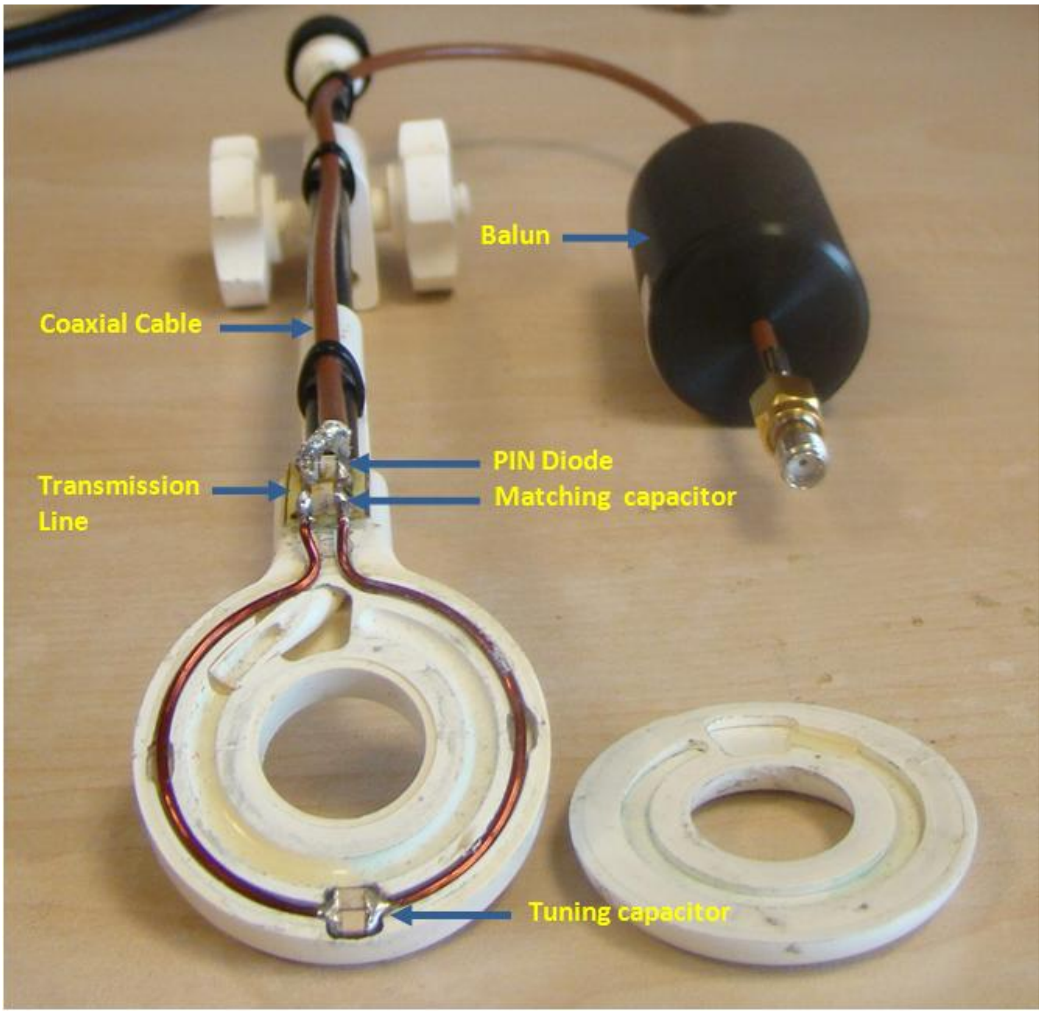

Figure 2.15: A picture of the manufactured loop coil placed inside the Nucletron CT/MR ring applicator.

2.3.1.2 Electrical Circuits Design

BALUN (BALANCED-UNBALANCED TRANSFORMER)

Each MRI coil (including this endocervical Loop coil) should be constructed upon proving that the balun is working properly at the Larmor frequency, 123.23 MHz. When a coil is directly connected to the scanner using a coaxial cable, unbalanced currents flow at the outer conductor of the coaxial cable. The unbalanced currents might have a negative effect on the functioning of the coil in different ways. They might, for example, affect the matching impedance of the circuit. As a current is flowing at the outer conductor, an external body such as the operator's hand close to the coaxial cable, can destabilize the matching condition of the coil by changing the matching impedance. Moreover the unbalanced current might act as a small receiving antenna; therefore any portion of human body touching the coaxial cable will create an artifact on the MR image. The unbalanced currents may also increase the noise level in the system which will decrease the SNR. These negative effects of unbalanced currents can be eliminated by using a balun circuit.

The type of balun which will be used in the endocervical loop coil is similar to bazooka type baluns with some differences [19]. In a bazooka type balun, a quarter-wavelength coaxial cable is covered with a metal shield and then this shield is connected to the outer conductor of the coaxial cable at one end so that the outer shield becomes a transmission line. If the length of the transmission line is adjusted to a quarter of the wavelength, the low impedance of one end of the balun is transformed to high impedance at the other end. The balun is connected to the coil and prevents the unbalanced current flow on the outer conductor. The principle of the bazooka balun is depicted in the Figure 2.16.

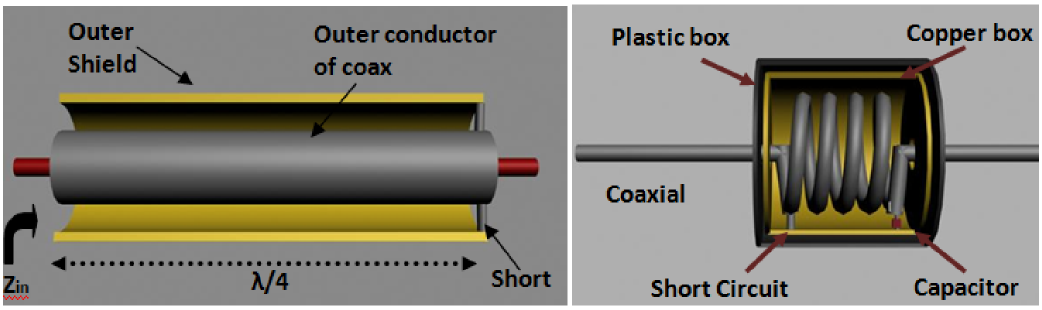

Figure 2.16: Left: The bazooka type balun. Right: The design of a balun circuit. The balun is contained in a cylindrical copper box and this copper box is confined in a plastic box which helps prevent human contact to the electronic circuit.

The principle of the balun used in the endocervical loop coil is very similar to a bazooka balun, except using a bazooka balun with a quarter-wavelength would be too long to use for clinical purposes. For this specific purpose, the whole bazooka balun is shrieked into a small box that is shielded by a cylindrical copper box with closed ends. Also, the coaxial cable is winded and placed inside the box. Similar to the previous method, the outer conductor is connected to the copper shield of the balun at one end. At the other end, a shunt capacitor is placed between the outer conductor and the shield of the balun. As a result, a transmission line is created with the outer conductor of the coaxial cable and the copper shield of the box in this configuration. The short circuit is transformed into inductive impedance at the outer end of the balun so this inductive impedance gets into resonance with the shunt capacitor. The following figure demonstrates this balun type.

The balun is constructed by winding a 3 mm double shielded coaxial (Suhner, Herisau, Switzerland) cable in 4 loops and placing it inside a copper cylindrical box with dimensions of 30 mm diameter and 35mm length. This copper box is housed by a cylindrical plastic box with 40mm diameter and 43 mm length. The balun is tuned using a single ATC MR compatible B type 70pF capacitor (Figure 2.17).

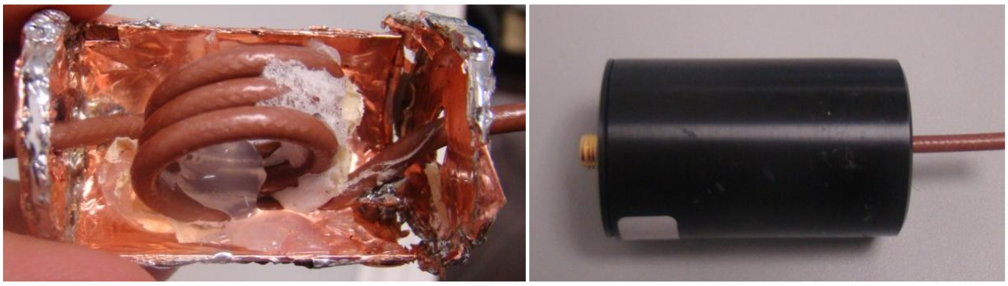

Figure 2.17: On the left shown is the internal structure of the balun explained above. On the right is a picture of the complete balun. Left end of the balun is connected to the MR scanner and right end to the loop coil.

The impedance seen from the shunt capacitor of the balun looking at the balun side is measured using a network analyzer. The resonance curve is plotted in the next figure. The balun impedance was measured as 1.6k ohms at 123.23 MHz.

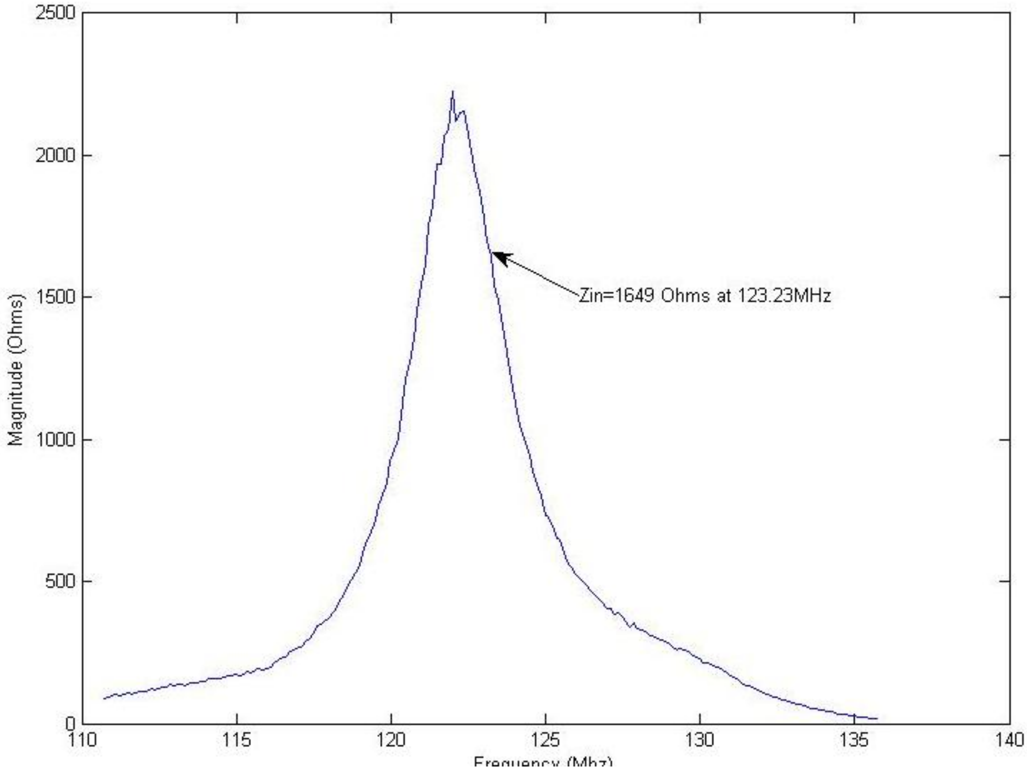

Figure 2.18: Resonance curve of the balun: Impedance seen on the shunt capacitor looking at the balun side.

MATCHING AND TUNING OF THE COIL

A well matched and tuned coil is necessary for a desired, high SNR value. Reflections due to a large non-zero reflection coefficient seen from the coil side may increase the noise. In order to avoid reflections, the wire loop of the coil was matched and tuned to 50 Ohms at 123.23 MHz (Larmor frequency). An L-type matching circuit i.e. a series capacitor at the middle of the loop and a shunt capacitor at the right end of the loop were used. The matching and tuning were performed with these American Technical Ceramics (ATC) 700 B series porcelain and ceramic capacitors. The L type matching circuit was preferred in this project rather than the other types of matching circuits such as Pi type and T type circuits, for two main reasons [20]: Firstly, the calculated capacitor values of the L type circuit are commercially available. Secondly, L type circuit is used to decouple the internal coil from the body coil by letting the shunt capacitor entering to resonance, which will be discussed later. The following figure demonstrates the L-type matching circuit.

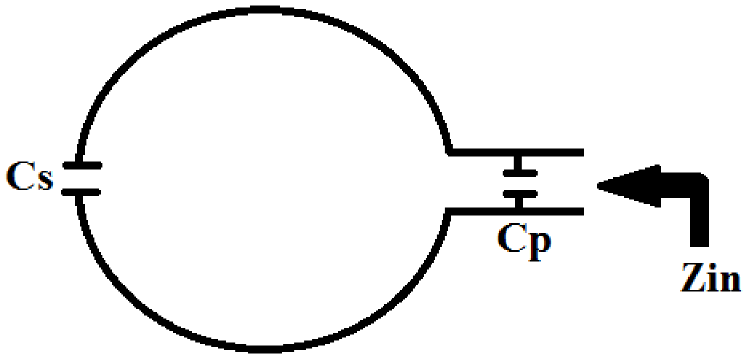

Figure 2.19: Coil diagram with L-type matching and tuning circuit.

The following equations are taken from [38]. In order to perform the matching, the impedance of the coil loop should be determined first. The loop impedance consists of a real and an imaginary part:

$$Z_{coil} = R_{coil} + j\omega L_{coil} \qquad (5)$$

The values R_{coil} and L_{coil} in the equation (5) were calculated experimentally. The two test capacitors, C_s and C_p were connected to the loop and the resulting input impedance Z_{in} was observed from the network analyzer. The results can be interpreted with the following equation:

$$Z_{coil} = ({Z_{in}}^{-1} - j\omega C_p)^{-1} - (j\omega C_s)^{-1} \qquad (6)$$

The frequency used for our experiment (ω) was the Larmor frequency (123.23 MHz for 3 Tesla). When $Z_{coil}$was determined, the required C_p and $C_s$values were calculated by using the set of equations shown below:

$$C_p = \frac{\sqrt{(Z_0 - R_{coil})/R_{coil}}}{Z_0 \omega} \qquad (7)$$

$$C_s = \frac{-1}{\omega\sqrt{R_{coil}(Z_0 - R_{coil})} - \omega 2L_{coil}} \quad (8)$$

In this formula, Z_0 is the characteristic impedance of the coaxial line, which was 50 Ohms in this case. The initial C_p and C_s (the shunt capacitor and the series capacitor) values were then replaced with the newly calculated capacitances. Next, the Zcoil was measured again. If the measured Zcoil value wasn't close to 50 Ohms, Cp and Cs were calculated again with the equations (7) and (8) using the finally measured Zcoil value. This process was repeated iteratively until the coil was matched to 50 Ohms at Larmor frequency.

In this experiment, all of the measurements for matching and tuning were performed when the coil was inside an agar copper sulfate solution (Agar: 4 gr/lt, NaCl: 1gr/lt, $CuSO_4$: 3gr/lt) phantom (Figure 2.20). This solution was identical to the solution used for coil imaging. The load impedance of the coil in the solution medium and in the air are different from each other, therefore they require different matching-tuning circuitry. As these endocervical coils will be placed in the human body, the matching and tuning experiment should be conducted when the coil is placed inside the phantom. A plastic glove helped to isolate the coil each time.

In order to achieve the approximate conductivity of a cervix tissue (0.51 S/m), a certain amount of copper sulfate and salt was added to water which turned out to have a conductivity of 0.56 S/m. The conductivity may alter the input impedance; therefore it should be carefully determined. A picture of the matched coil is shown in Figure 2.20.

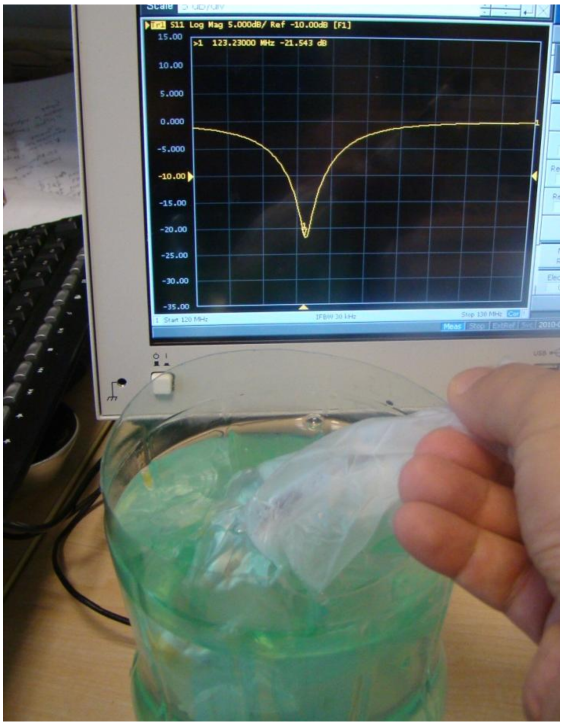

Figure 2.20: A picture of matched coil in agar solution. The coil was matched to 50 ohm and -22 gain db was observed.

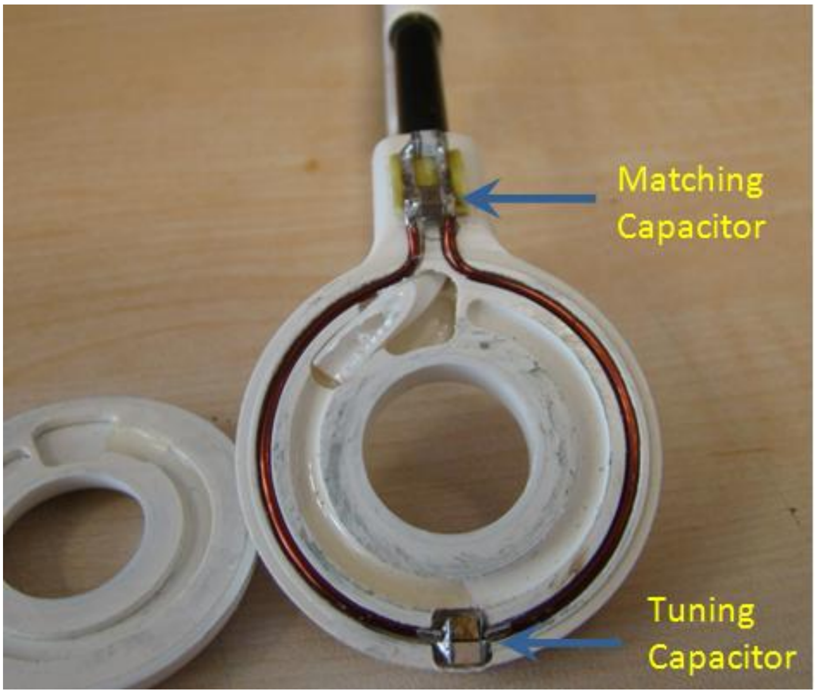

Figure 2.21: A picture of the matched and tuned loop coil used inside endocervical loop coil.

DECOUPLING

During the body scan, the MRI scanner sends RF pulses to adjust the spins of the body in the transmit phase. The echo caused by the recovery of the spins is listened by the scanner to create a conventional MR image. In the transmission phase, RF waves transmitted by the scanner cause some induced currents passing on a tuned and matched coil. These induced currents cause an additional magnetic field and leads to a change in the orientation of the spins in a predictable way. This results in decoupling artifacts on the MR image. To prevent this effect, the coil should be decoupled and the induction of the current in the transmission RF pulses should be eliminated. A simple decoupling mechanism was used for this purpose; a non-magnetic PIN diode (MA4P7461F-1072T, Macom, Lowell, MA) was used to put the shunt capacitor in resonance. In order to do this, a DC voltage was supplied to the coil during the transmission phase of the scanning. This DC voltage turned the PIN diode on and helped it to act almost like a short circuit. The following figure illustrates the matching and tuning capacitors and the diode placed at an L distance away from the shunt capacitor.

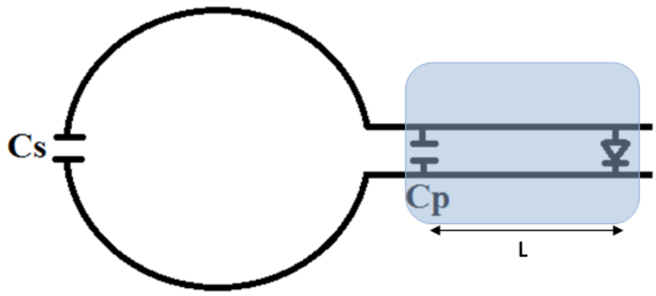

Figure 2.22: Coil diagram with decoupling capacitor in resonance with the tunning capacitors.

The two lines printed on the PCB connecting the diode and the shunt capacitor can be regarded as a small two line transmission line. The impedance of the short circuit was transformed to an inductive value through this small transmission line so that this inductance value was in resonance with the shunt capacitor. The state of resonance can only be reached when the shunt capacitor is in resonance with the inductance value that is caused by the diode end. This causes an increase in the impedance seen from the capacitor side, resulting in a small or no current flow through the loop coil. Finding the exact length of the transmission line is very crucial at this point. This distance was calculated with the following method; a small copper wire was used to short circuit the two lines of the transmission line. With the help of the network analyzer, the impedance seen from the capacitor end looking to diode side was measured on different locations of the wire on the transmission line. The location of the wire on the transmission line, where the maximum impedance was observed, was marked. Then this small wire was replaced with the PIN diode and the impedance was measured continuously, but this time a DC voltage of 0.8 V was supplied from the network analyzer. By the time the resonance is achieved, the decoupling diode accomplishes its task. The Figure 2.23 below shows the orientation of the matching and tuning and decoupling circuitry of the endocervical loop coil.

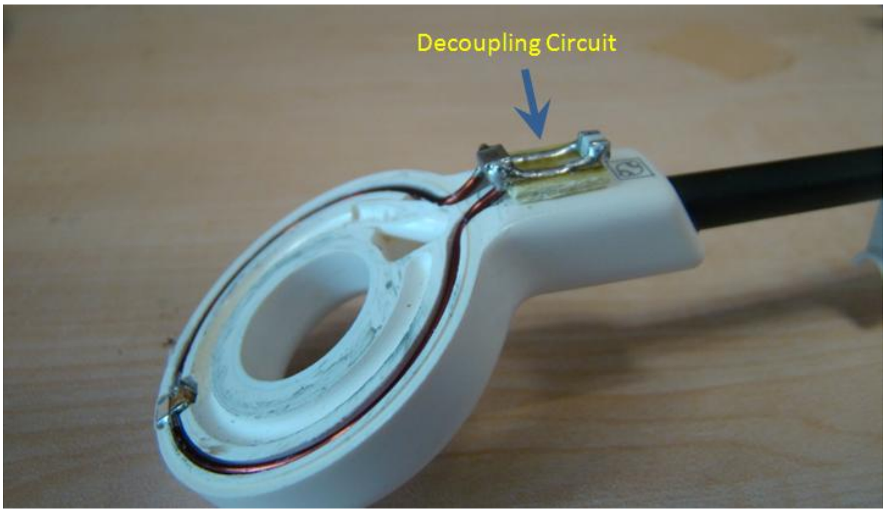

Figure 2.23: Matching-tuning and decoupling circuit of the single loop endocervical loop coil.

The final appearance of the endocervical coil that is ready to be tested in an MRI scanner is shown in the Figure 2.25 .

Figure 2.24 shows the resonance state achieved between the shunt capacitor and the diode used for the decoupling circuit. Impedance value seen by looking from the coil end of the shunt capacitor is plotted in the figure.

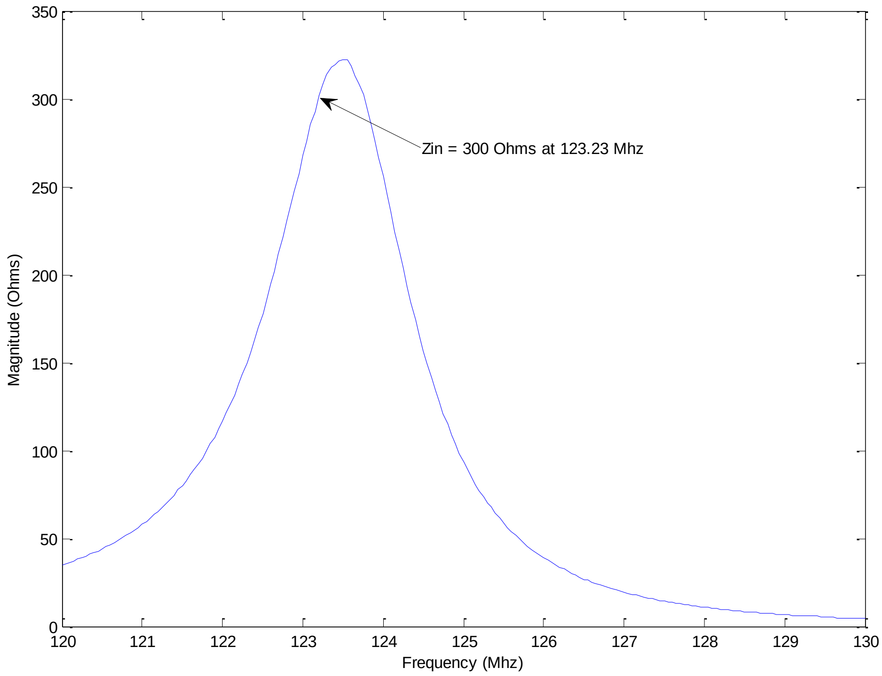

Figure 2.24: A plot showing the resonance curve of the decoupling circuit used for the loop coil

Figure 2.25: A picture of the final l structure of the Nucletron CT/MR ring applicator with a loop coil placed inside.

2.3.2 Endocervical Loopless Probe

The design of an endocervical loopless probe starts with the investigation of the tandem applicator of the Nucletron CT-MR ring applicator (Figure 2.26), which was developed for gynecologic brachytherapy procedures. This non-metallic applicator is also designed using composite fiber tubing in order to eliminate distortions on CT or MR images. The 60-degree version was studied in this work (the reason was explained in the previous section). Figure 2.26 shows the described tandem applicator. The total length of the applicator is 29.5 cm. The longer part of the applicator, which is marked as part A in Figure 2.26, is 24 cm long and 6mm wide. This part is placed inside the vajina during the HDRB procedures. The shorter part, which is marked as part B in Figure 2.26, is 6.5 cm long and 3.8 mm wide. This part, on the other hand, is placed through the ring applicator into the cervical canal. The diameter of the inner lumen of the applicator is measured as 2.5 mm.

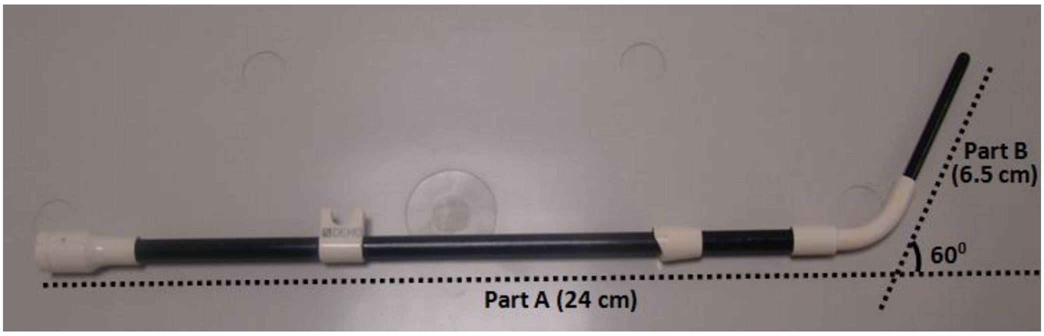

Figure 2.26: A picture of the Nucletron CT-MR tandem applicator which is developed for gynecologic brachytherapy procedures. The exact detentions of the applicator are shown in the picture. The length of the inner lumen is 29.5 cm and the diameter of the inner lumen is 2.5mm.

2.3.2.1 The Materials and Methods

The design of the endocervical loopless probe is shown in Figure 2.27. The probe is designed in a way that it could be housed inside a brachytherapy applicator during the MRI and can be easily removed, giving its place to the radiation source. The design of the endocervical loopless probe is based on the loopless antenna design. Since it has a very small profile, it can be used in the body cavities for the purpose of acquiring high signal-to-noise ratio images in the vicinity of the region it is placed. The endocervical loopless probe consists of a coaxial cable with extended inner conductor, decoupling/ matching circuits and a balun.

The detailed design of the loopless antenna is shown in Figure 2.27. All the dimensions of the material used in the construction of the endocervical loopless probe were chosen in accordance with the tandem applicator inner lumen size of 2.5 mm. So, the loopless coil was designed to be 2.3mm in diameter and 133.2 cm in length, and was constructed using all medical-grade components. Basically, the antenna consists of a coaxial portion and an extended inner conductor. From (12) we know that the length of the inner conductor has to be adjusted to the λ/4 at Larmor frequency. However, this is unreasonable in our case as λ/4 at 123.23 MHz is longer than 30 cm. The highest signal intensity is achieved at the distal end of the coaxial portion and then decreased exponentially. In that situation the cervix (ROI) would be nearly 25 cm far from the coaxial portion and the signal at this region is significantly low. In order to solve this issue, we used a 1.7 mm wide and 5.9 cm long solenoid coil (Figure 2.27-1) instead of the extended inner conductor. The proximal end of this solenoid coil was connected to the 0.4 mm cupper magnet wire (Newark, Palatine, IL) through the entire length of the endocervical loopless probe (Figure 2.27-2). This magnet wire constitutes the inner conductor of the coaxial portion. This magnet wire was inserted through a polytetrafluoroethylene (PTFE, Zeus, Orangeburg, SC) medical tubing with 1.4 mm inner diameter and 0.4 mm wall thickness. This medical tubing acts as an isolator between the inner and outer conductors of the coaxial portion (Figure 2.27-3). The whole coaxial portion was covered with flat braided tinned copper tube (Newark, Palatine, IL) which is the outer conductor of the coaxial portion (Figure2.27-4). The whole assembly including the solenoid coil was covered with polyester heatshrink tubing (Advanced Polymer, Salem, NH) with 0.076 mm wall thickness (Figure 2.27-5). The length of the coaxial portion was adjusted to 3λ / 4 wavelengths - 127.3 cm - at 123.23 MHz Larmor frequency. A non-magnetic SMA connector (Lemo, Ecublens, Switzerland) was placed to the proximal end of the loopless probe (Figure 2.27-7). A balun (Balance Unbalance Transformer) was placed 57 cm away from the distal end of the coaxial portion (Figure 2.27-6) and the endocervical loopless probe was matched and decoupled. These circuits are described in detail in the following sections.

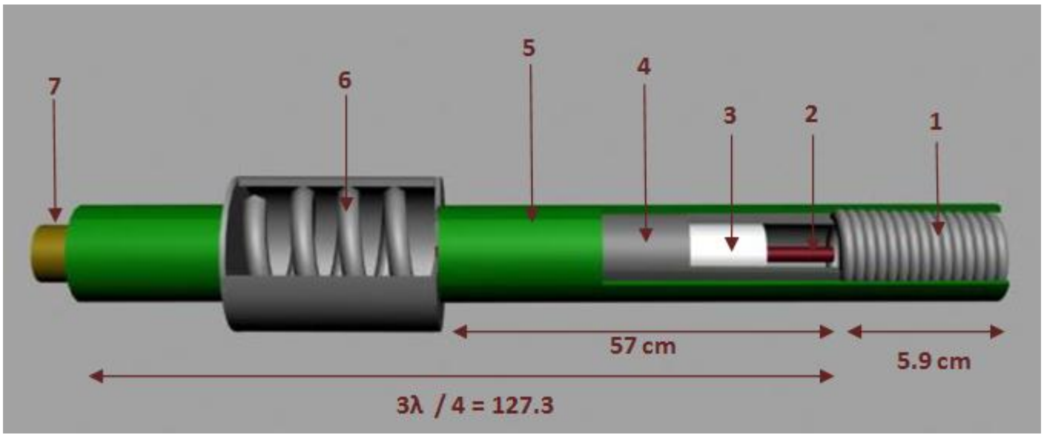

Figure 2.27: Endocervical Loopless probe schematic: (1) Copper Coil. (2) Inner conductor. (3) PTFE tubing. (4) Cupper Breading Shield. (5) Polyester heatshrink tubing. (6) Balun. (7) non-magnetic ASM connector.

Solenoid Distal Coil

A picture of the solenoid distal coil is given in Figure 2.28. This handmade coil is made by tightly winding 0.2 mm (Newark, Palatine, IL) magnet wire around 1 mm nitinol rode. In the beginning the coil was produced 10 cm long, however the coil was then shortened to give an approximate real impedance of 50 ohms. This procedure is explained in detail in matching and tuning section. The length of the coil was adjusted to the 5.9 cm for the sample that is explained in this work.

Figure 2.28: A picture of the solenoid distal coil used for the endocervical loopless probe. the coil is 5.9 cm long and 1.7 mm wide .

Inner Conductor of Coaxial Portion

The inner conductor for the coaxial portion is given on the Figure 2.29. A 0.4 mm copper magnet wire (Newark, Palatine, IL) was used. The diameter of the wire was determined so that the characteristic impedance of the coaxial portion would be around 50 ohms. This procedure will be described in the Matching and tuning sections.

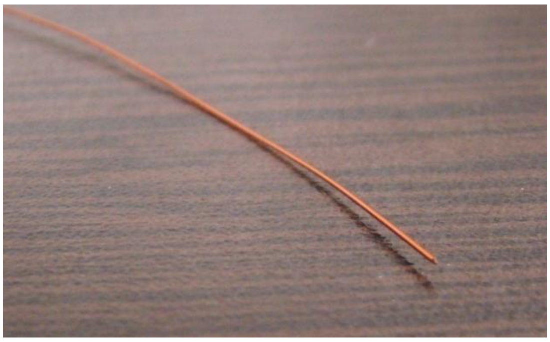

Figure 2.29: A picture of the magnet wire that was used as an inner conductor of the coaxial portion of the endocervical loopless probe.

Medical Tubing (Isolator for coaxial cable)

A polytetrafluoroethylene (PTFE, Zeus, Orangeburg, SC) medical tubing with 1.4 mm inner diameter and 0.4 mm wall thickness was used as an isolator between the inner and outer conductors of the coaxial portion.

A polytetrafluoroethylene tubing (PTFE, Zeus, Orangeburg, SC) with 1.4 mm inner and 0.4 mm wall thickness (Figure 2.30) was used to provide an isolation between the inner and outer conductor of the coaxial portion and provide circuit stability as well as providing the torque transition. PTFE has the desirable dielectric properties (ϵ_r=2 or less). This is especially true for high radio frequencies, making it suitable to be used as an insulator in cables. PTFE has one of the lowest fraction values among solids. This low fraction helps us pass it through the copper breading tube (Figure 2.31) easily. The dimensions of this PTFE tube are determined so that the characteristic impedance of the coaxial portion will be around 5 ohms and at the same time the outer diameter of the coaxial portion could be kept less than 2.4 mm. A picture of the PTFE tube is given in the following figure.

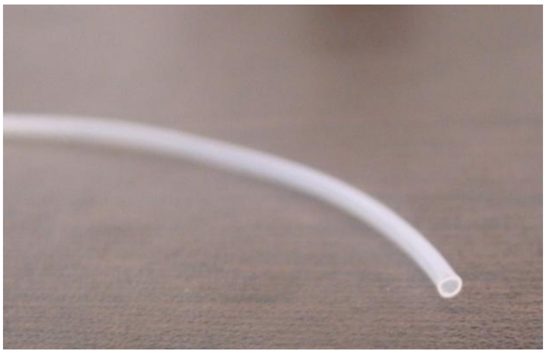

Figure 2.30: A picture of the polytetrafluoroethylene tubing with 1.4 mm inner diameter and 0.4 mm wall thickness. This medical tube is used as an isolator between the inner and outer shells of the coaxial portion.

Cupper Breading Tube

A picture of this copper braided tube is shown in Figure 2.31. This copper breading tube (Newark, Palatine, IL) with 0.2 mm wall thickness was used as an outer conductor of the coaxial portion. Again the dimension of the tube is determined to adjust the characteristic impedance of the coaxial portion to 50 ohm as well as the outer diameter to a value less than 2.4 mm.

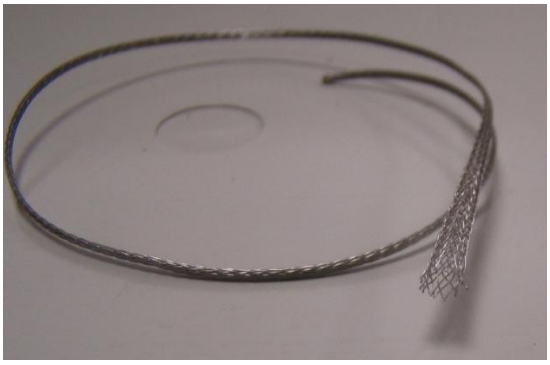

Figure 2.31: A picture of the copper breading tube with 0.2 mm wall thickness that was used as an outer conductor of the coaxial portion.

Heat Shrink

A polyester heatshrink (Advanced Polymer, Salem, NH) with 3.35 mm outer diameter and 0.76 mm wall size with ½ expansion ratio was used as an outer isolator to provide electrical shielding and liquid isolation. This heatshrink brings a unity in the guidewire combining all components together. A picture of the heatshrink is given in Figure 2.32.

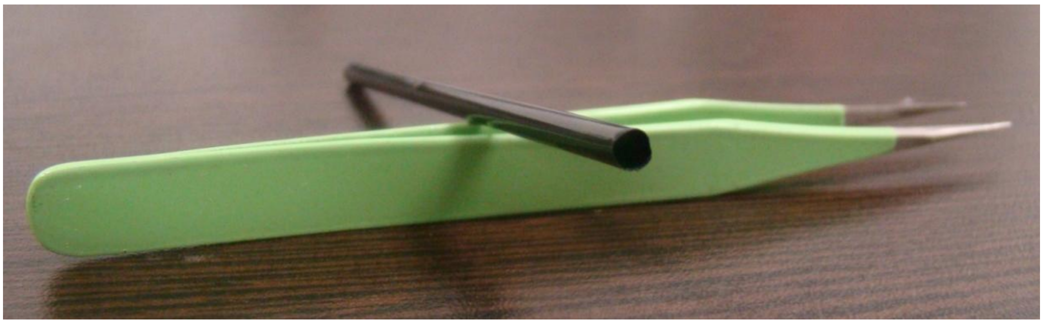

Figure 2.32: A picture of the polyester heatshrink tube with 3.35 mm outer diameter and 0.76 mm wall size before the expansion. This heatshrink was used as an outer isolator to provide electrical shielding and liquid isolation for the endocervical loopless probe.

A photo of the assembled coaxial portion is given in Figure 2.33.

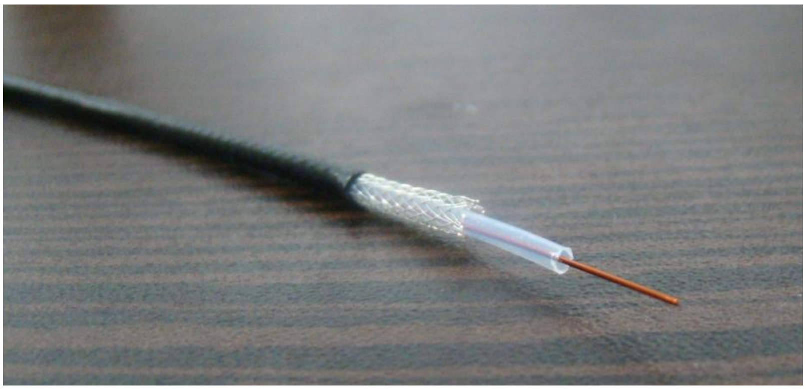

Figure 2.33: A picture assembled coaxial portion of the loopless antenna that was used inside the endocervical loopless probe.

2.3.2.2 Electronic Circuit Design

Balun (Balanced-Unbalanced Transformer)

Each MRI coil (including this endocervical loopless probe) should be built after proving that a balun is properly working at the Larmor frequency, 123.23 MHz. Connecting the coil directly to the scanner would result in unbalanced currents to flow on the outer conductor of the coaxial portion of the probe. The unbalanced currents can cause problems for the coil in three ways. In addition to the effects that were explained in the loop coil section, unbalanced currents may cause excessive heating of the probe and could damage a healthy tissue. This unwanted effect can be prevented by using a balun circuit as well.

The working principle of the balun was explained in detail in the loop coil section. In this application we used a similar method. However, this time the coaxial portion of the endocervical loopless probe was used instead of a commercial coaxial cable. The balun was constructed by winding the coaxial portion of the probe in 4 loops and placing it inside a copper cylindrical box with dimensions of 30 mm diameter and 35mm length. This cupper box is housed by a cylindrical plastic box with 40mm diameter and 43 mm length. The balun is placed 57 cm away from the distal end of the coaxial portion. It is then tuned using a single ATC MR compatible B type capacitor. A picture of the constructed balun is given in Figure 2.34.

Figure 2.34: On the left hand side the internal structure of the explained balun is depicted. On the right side a side-view of the complete balun is given.

The impedance seen from the shunt capacitor of the balun looking at the balun side was measured using a network analyzer. The impedance of the balun was measured as 2.1k ohms at 123.23 MHz.

Matching and Tuning

The loopless antenna's impedance was matched to 50 ohms at 123.23 MHz (Larmor frequency) to avoid reflections. Reflections caused by a large non-zero reflection coefficient seen from the coil side may result in losses on the transmission line and thus increases the noise. To have higher SNR it is crucial that the coil is well matched to the characteristic impedance of the coaxial portion of the probe. In this design no extra tuning circuit is required for matching because the loopless antenna's impedance is optimized to a value close to the characteristic impedance of the coaxial cable.

Antenna impedance is an important parameter for the performance of the loopless antenna. In the manuscript by Ocali [1], it was shown that the square root of the real component of the antenna impedance was inversely proportional to the signal-to-noise ratio. In case of the bare-wire antenna, the minimum observed impedance was 35 ohms. It was shown that when the antenna was insulated because of some practical requirements, the real part of the impedance increased and degraded the SNR performance of the system.

All of the electrical measurements were performed when the probe is placed inside agar copper sulfate solution (Agar: 4 gr/lt, NaCl: 1gr/lt, $CuSO_4$: 3gr/lt) phantom. This solution was identical to the solution used for imaging experiment. The load impedance of the coil in the solution medium and air were different from each other, therefore they require different matching-tuning circuitry. As these endocervical coils will be placed in the human body, the matching and tuning experiment should be conducted when the coil is placed inside the phantom with the similar electrical properties as cervix. A plastic glove helped to isolate the applicator from the liquid solution.

In order to understand the performance of the design, we measured antenna impedance inside the brachytherapy applicator placed in the phantom with the agar solution. The length of the coiled portion of the loopless antenna was optimized to read minimal real impedance. 62 ohms real impedance was obtained when the coil length was kept 5.9 cm at 123.23 MHz (Larmor frequency). Although this impedance is higher than 35 ohms, as obtained by the bare-wire antennas, loss of 33% reduction in SNR ($SNR\ reduction = \sqrt{62/35}$) is acceptable for this application.

When the characteristic impedance of the coaxial cable matches the antenna impedance, the signal transmission is obtained with minimum loss (Figure 2.35). In most coils there is a significant difference between coaxial cable impedance and the antenna impedance, therefore a matching circuit is necessary. In the loopless design, as mentioned above, the antenna impedance was 62 ohms. If the characteristic impedance of the coaxial portion meets this value, there will be no need for a matching circuit.

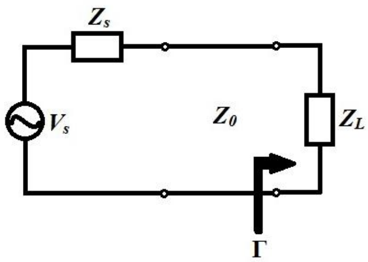

Figure 2.35: Simple circuit configuration of the loopless probe showing measurement location of the reflection coefficient.

In order to measure the characteristic impedance of the coaxial portion, the length of the coaxial portion was adjusted to the λ/4 wavelength and a 50 ohms load was connected to the distal end. Looking from the proximal end of the coaxial portion the impedance was measured as 59 ohms. Therefore the characteristic impedance is calculated as:

$$Z_0 = \sqrt{Z_S \times Z_L} \tag{9}$$

Z_L is the measured impedance and Z_s is the characteristic impedance of the supply (in our case, MRI scanner), which is equal to 50 ohms. From this formula, characteristic impedance of the coaxial portion (Z_0) is calculated as 54 ohms. The antenna impedance was previously measured as 62 ohms above and the reflection coefficient (Γ) was calculated as 0.068 which is acceptable, so no matching circuitry is necessary.

Decoupling

A tuned and matched coil will have some induced current flowing on it as RF waves are transmitted by the scanner (This current flow was described in detail previously). These induced currents create additional magnetic field and change the orientation of the spins around them. This results in decoupling artifacts on the MR images. To avoid this, the coil should be decoupled and no current should be induced during the transmission of RF pulses.

A simple active detuning scheme, a non-magnetic PIN diode (MA4P7461F-1072T, Macom, Lowell, MA), was used for this purpose. During the transmit stage, Siemens TIMTrio 3T scanners provide a DC bias current. In this period PIN diode in the circuit turns on and its RF impedance decreases. Three quarter wavelength coaxial cable transforms this low impedance value to a high value at the distal end of the coaxial portion. Depending on the loss of the coaxial cable, the value of this high impedance may vary. Notably, the effectiveness of the decoupling circuit strongly depends on this impedance value. The Figure 3.36 shows the PIN diode placed inside SMA connector on the proximal end of the three quarter wave length coaxial portion.

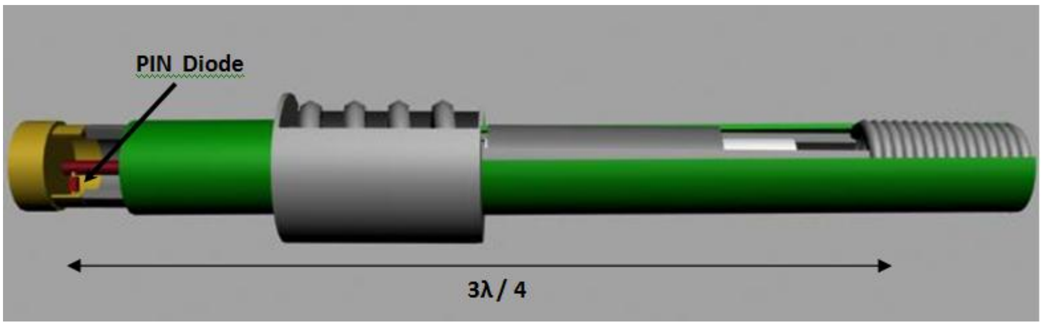

Figure 2.36: Detailed design of the decoupling circuit of the loopless probe of endocervical MRI probe. The decoupling circuit is achieved by adjusting the length of the coaxial shaped body part of the catheter to the quarter wave length and placing the PIN diode to the proximal end of the coax.

In order to evaluate the performance of the decoupling circuit, one end of the $3\lambda/4$ coaxial cable is shorted and the impedance was measured on the other end. A short circuit was placed to the distal end of the coaxial portion and impedance looking from the distal end was measured as 2.8k ohms. This value is significantly higher than the antenna impedance of 62 ohms, suggesting significant suppression of induced currents. Further testing of the decoupling performance was done using imaging experiments.

The final appearance of an endocervical loopless probe that is ready to be tested in an MRI scanner is shown in Figure 2.37. A picture of the complete two channel Endocervix coil for HDRB is given in Figure 2.38.

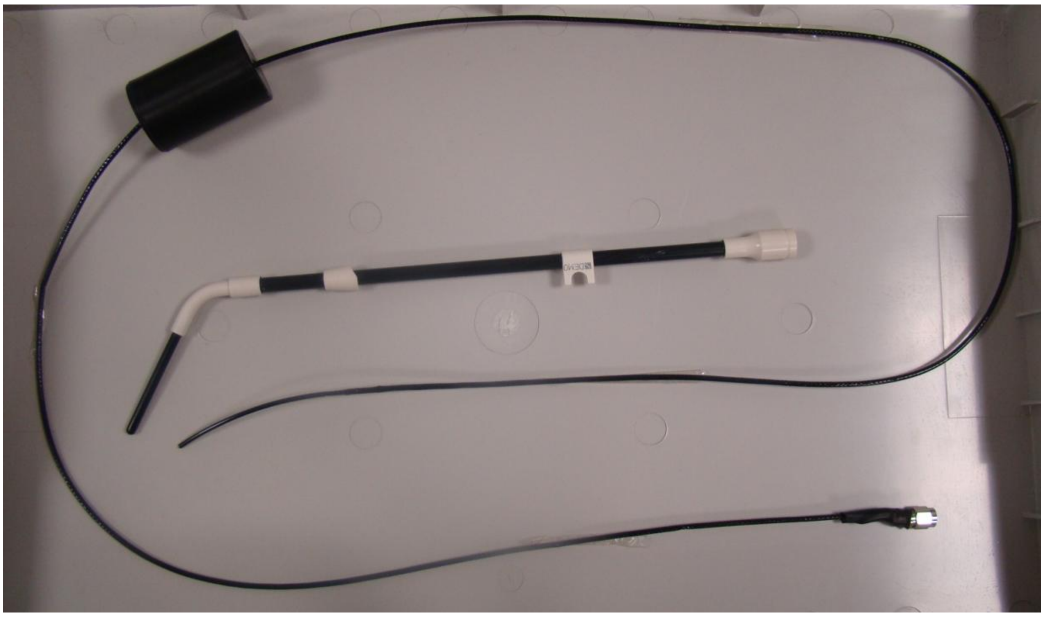

Figure 2.37: A picture of endocervical loopless probe.

Figure 2.38: A picture of the two channel endocervix coil for HDRB

2.4 Experiment and Results

In this section, the experimental methods to test the performance of the proposed two channel endocervix coil are shown. All the imaging experiments were performed on 3T (TIMTrio, Siemens) scanner and the heating test was performed on 1.5 T (Excite, General Electronics Health Care). There is no special reason to use two different scanners. At the time this project started our group had an agreement with Bayindir Hospital (Ankara, Turkey), where all the heating experiments were done in 1.5T GE scanner. As UMRAM (National Magnetic Resonance Research Center) was established, we transferred all the experiment setups to the 3T scanner. Since the electrical test results were consistent for coils constructed for both 1.5 T and 3 T scanners, we didn't repeat the heating experiments on 3T scanner.

All the imaging experiments were performed in 3T (TIMTrio, Siemens) scanner. Both of the coils were used in receive-only mode and connected to the MRI scanner via a custom 2 channel preamplifier interface (UMRAM, Ankara, Turkey) (Figure 2.39).

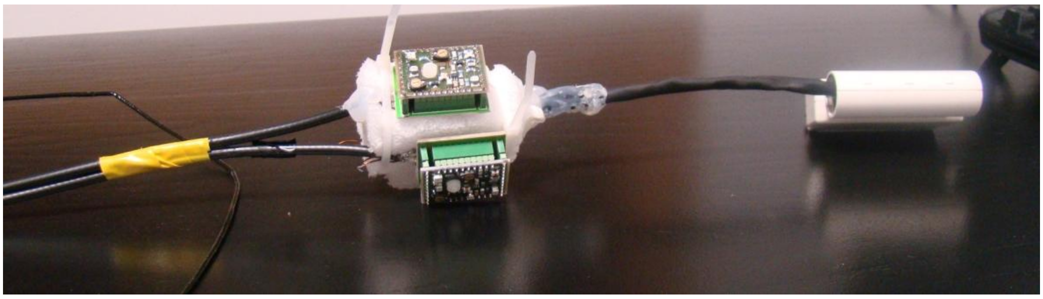

Figure 2.39: A picture of 2 channel custom preamplifier interface that was used to test two proposed coils.

2.4.1Heat Experiments of Endocervical Loopless Probe

In the transmission of body coil in the interventional MRI, the body coil and metallic interventional devices may result in an electromagnetic decoupling. This may cause the concentration of the field and deposition of the consequent power with the high probability of heating the device significantly. The regulatory body in the United States, governing the use of magnetic resonance devices is called The Food and Drug Administration (FDA), and the current regulation dictates two Specific Absorption Rate (SAR) limits for RF heating ("whole body" SAR limit and "local" SAR limit). These limits are based on current International Electrotechnical Commission (IEC) standard. To be precise, these limits are 8 W/kg in any gram of tissue in the extremities for 15 minutes [21] and 2 degrees temperature rise [22].

Although it is possible to theoretically estimate the expected heating, the straightforward method is to measure the temperature rise within the body during the examination. Since it is not ethical to do these tests on patients, it is customary to use phantoms imitating human body. With this motivation, we designed a semi-cylindrical gel (Dr. Oetker Fruit Gelatin with NaCl: 1gr/lt, $CuSO_4$: 3gr/lt) phantom as shown in Figure 2.40. The electrical properties of the phantom are very close to the cervix.

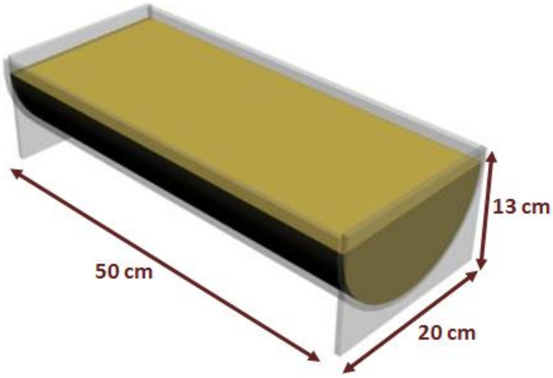

Figure 2.40: A simple drawing of the phantom gel with (Dr. Oetker Fruit Gelatin with NaCl: 1gr/lt, $CuSO_4$: 3gr/lt) solution that was used in the heating experiment with endocervical loopless probe. The dimensions of the phantom are as shown in the figure.

In order to expose the probe to an extreme condition, the semi cylindrical phantom was placed at the edge of the MRI scanner and the probe was placed at the edge of phantom. The exact location of the probe with respect to the scanner can be seen in Figure 2.41. All of the experiments were made under GE 1.5T excite MR scanner. The temperature rise was measured using Neoptix ReFlex four-channel signal conditioner and T1 fiber optic temperature sensors (Neoptix, Inc., Quebec City, QC, Canada).

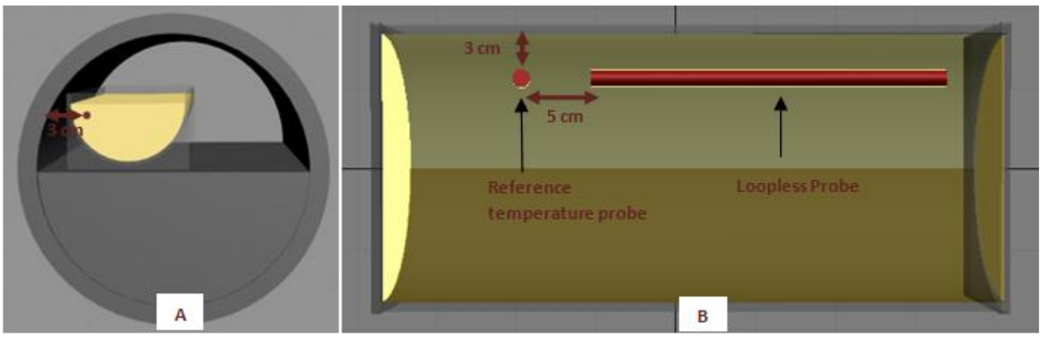

Figure 2.41: The place of the endocervical MR probe inside the MR scanner. (a) The position of the phantom inside the scanner. The total distance between

the probe and MR wall is about 3 cm. (b) The position of the loopless probe inside the phantom. An additional reference temperature probe was used in order to measure the heat increase of the phantom.

Four temperature probes are located on the endocervical loopless probe as shown in Figure 2.42. The highest temperature increase was measured on the 3rd channel (Figure 2.42). This probe was located at the distal end of the coaxial portion. An additional probe was placed in the phantom as shown in Figure 2.41 as a reference.

The applied SAR (Specific Absorption Rate) was calculated using the data obtained from the reference probe. Note that the SAR values reported by the scanner can be misleading since the scanner SAR reporting software assumes a human body is present in the scanner and the mass of the phantom used in these experiments was significantly smaller than the mass of a human body.

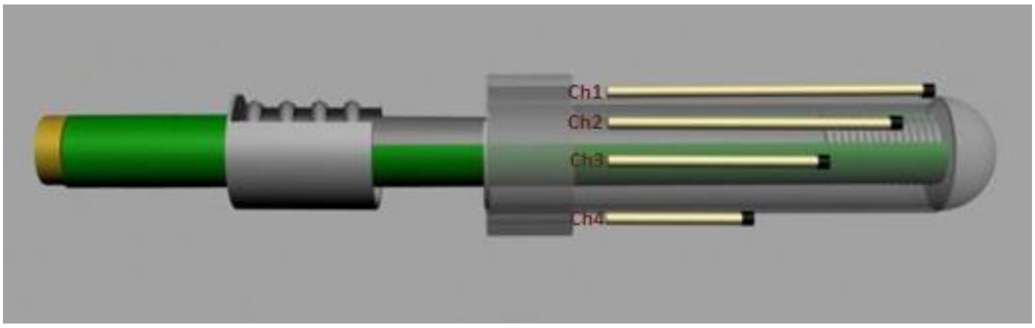

Figure 2.42: Locations of the temperature probes on the tandem applicator which house loopless probe.

Heating experiment was conducted using SPGR pulse sequence with the following imaging parameters: TR = 6.25ms, flip angle = 90^{o} and scan time = 720 seconds. Other imaging parameters were TE = 1.7ms, 256x128, NEX = 60, BW = 62.5 kHz, FOV = 48cm, slice thickness = 20mm, 15 repetition.

Using the above parameters, two independent experiments were conducted. Experiment results are shown in Figure 8. Temperature rise of the channels and the temperature rise observed on the temperature probe need to be interpreted separately.

The temperature rise values observed using reference temperature probe were 2.1 and 2.6 degrees in 720s. Assuming a heat capacity of 4200 J/kg/K, the applied SAR values can be calculated as 8.75W/kg and 9.25W/kg, respectively.

Figure 2.43 demonstrates that after 720s, the temperature was not in its steady state value. This is because the phantom that we used did not have perfusion, but if we conduct an in vivo experiment, the temperature is expected to reach the steady state value in a short period of time. This difference was studied earlier and a method of estimation of in vivo temperature rise on a perfusionless phantom has been demonstrated [23]. According to that study, the temperature on the perfusionless phantom is always higher than in vivo temperature rise and the value of the temperature recorded at the specific time (perfusion time constant) is approximately equal to the expected in vivo temperature rise. The same study suggests that the maximum perfusion time constant in body is in fat and it is around 400s [23]. Therefore, one may report the temperature rise on a perfusionless phantom at 400^{th} second after application of the power, as the estimated maximum in vivo temperature.

The IEC and FDA regulations limit the maximum temperature rise to 2 degrees Celcius and the SAR value to 10W/kg. In our case, the applied SAR values for these cases were 8.75W/kg and 9.25W/kg, and the in vivo maximum temperature rise for these two experiments can be estimated as 1.5 and 1.6 degrees Celcius, respectively. Note that because of the whole body power tolerance limits, this power is never actually applied to the patients during an MR examination. To conclude, this design can be safely used in MR scanner without an excessive RF heating concern.

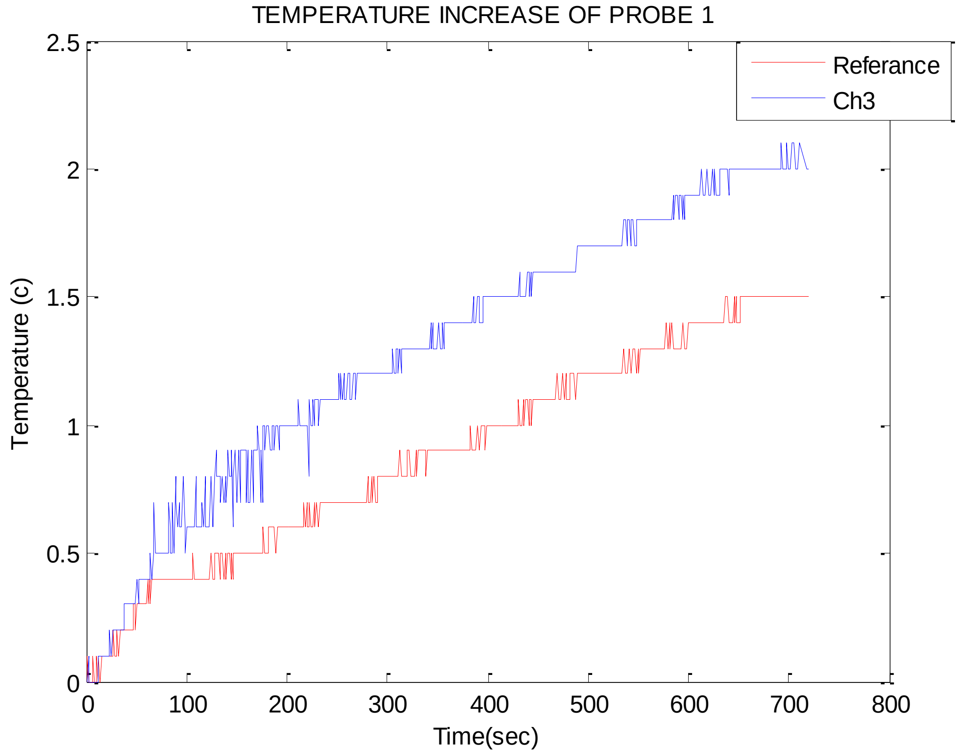
TEMPERATURE INCREASE OF PROBE 1
Referance
Ch3
Temperature (c)
Time(sec)
0
0.5
1
1.5
2
2.5
100
200
300
400
500
600
700
800

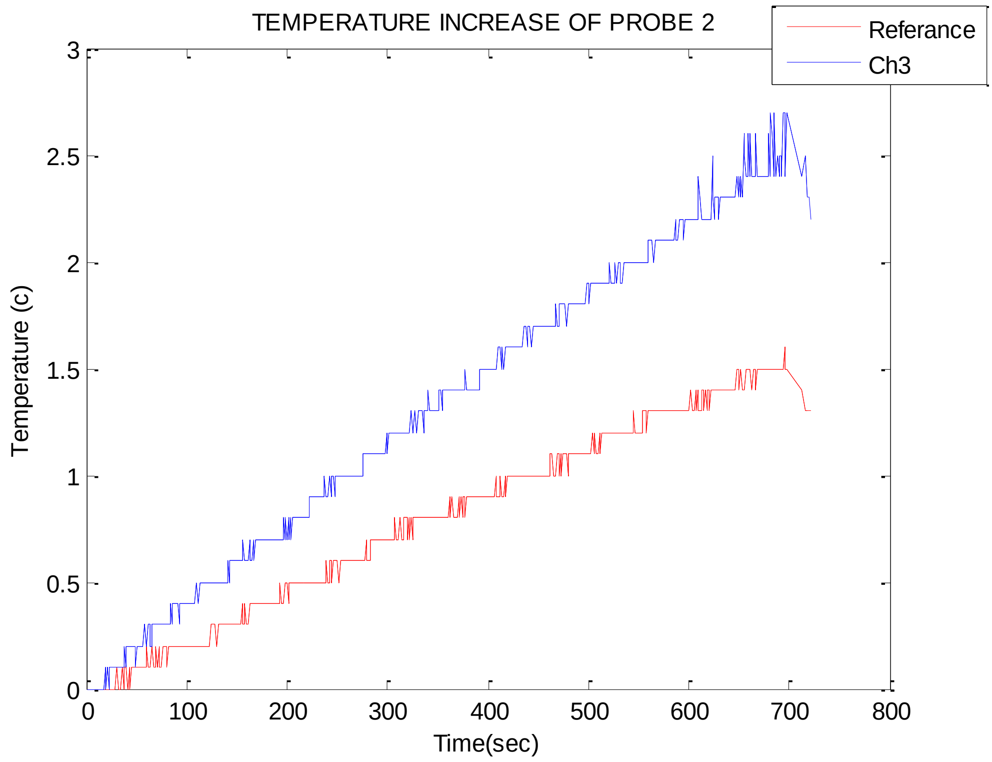
TEMPERATURE INCREASE OF PROBE 2
Referance
Ch3
Temperature (c)
Time(sec)
0
0.5
1
1.5
2
2.5
3
100
200
300
400
500
600
700
800

Figure 2.43: Graphs for the temperature increase of the endocervical magnetic resonance imaging probes.

2.4.2 Visibility Performance Testing Under the MRI

To test the imaging performance of the probe, a cylindrical phantom, with a diameter of 22 cm and a length of 35 cm, filled with a copper sulphate solution (NaCl: 1gr/lt, $CuSO_4$: 3gr/lt, Agar: 4gr/lt) was used to simulate loading conditions (ϵ_r =75, $\boldsymbol{\sigma}$ =0.56 S/m). The applicator was placed in the phantom as shown in Figure 2.45. Then the phantom was filled with the solution and aligned with the z-axis inside the MR scanner. The applicator was carefully fixed with striking plaster so that the surface normal of the ring applicator would be parallel to the z-axis. The endocervical loopless probe was placed into the tandem applicator and both of the channels were connected to the MR scanner by a proposed preamplifier connection box. The phantom was imaged with Turbo Spin Echo (TSE) with the following imaging parameters: TR=6000, TE=12, slice thickness=2 mm, FoV=256 mm x 256 mm, BW=200Hz/pixel. A coronal image was obtained 2 cm away from the ring wall of the ring applicator. The images were saved uncombined.

The resultant images are given in Figure 2.44. On the left is an image of the endocervical loopless probe. As expected, the signal intensity is high around antenna and decreases rapidly as the distance to the coil increases. The figure at the center is an image of the loop coil. The null region at the center can be easily observed. On the right side, the image obtained with the combined structure is shown. The null region at the center of the loop coil was compensated with loopless coil and a nearly homogeneous region was achieved.

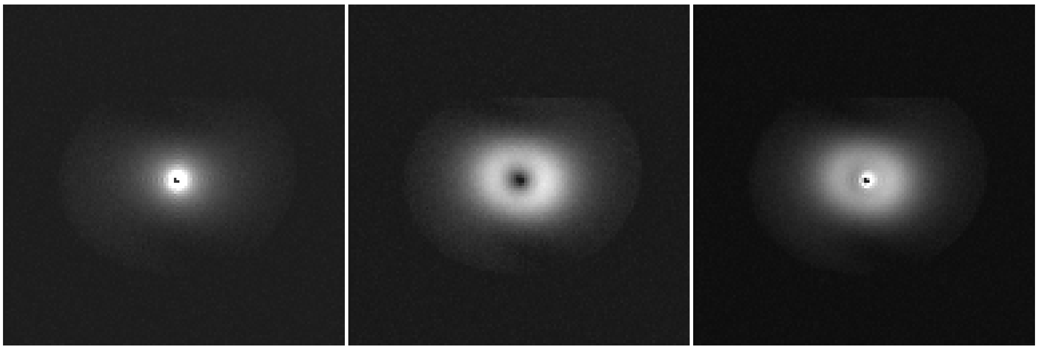

Figure 2.44: On the left side a phantom image obtained with endocervical loopless probe, in the middle an image obtained with loop coil and on the right side an image obtained by the two channel combined structure are given. The images were obtained 2 cm away from the ring applicator.

So far, the best method for cervix imaging was by body matrix coil. So, in order to compare the performances of the two channels, endocervical coil and body matrix coil in the ROI, the following experiment is conducted. A kiwi was used in order to simulate the cervix (ROI). The tandem applicator was inserted through the center of the kiwi and placed into the center of the cylindrical phantom explained above. The phantom was filled with the same solution that was used in the previous experiment (Figure 2.45) and aligned with the z-axis inside the MR scanner. The applicator was carefully fixed with striking plaster so that the surface normal of the ring applicator would be parallel to the z-axis (Figure 2.45). The kiwi inside the phantom was imaged with both two channel endocervical coil and the body matrix coil using T1-weighted Turbo Spin Echo with the following imaging parameters: TR=800, TE=12, slice thickness=2.6mm, FoV=150mm x 150mm, BW=260Hz/pixel.

Figure 2.45: On the left is a picture of the empty cylindrical phantom with a diameter of 22 cm and a length of 35 cm. The two channel endocervix coil was inserted into the kiwi and placed at the center of the phantom. On the right is the phantom filled with a copper sulphate solution (NaCl: 1gr/lt, $CuSO_4$: 3gr/lt, Agar: 4gr/lt).

The obtained image of the kiwi is shown in Figure 2.46. Although a thorough SNR analysis was not conducted, using expressions of [24] we could conclude that approximately 5-fold SNR increase in the kiwi images was observed with the two channel endocervical coil compared to the images obtained by the Siemens body matrix coil. The image quality obtained by the proposed endocervical coil is significantly better as can be detected in Figure 2.46. The null region at the center of the loop coil was successfully compensated by the loopless coil.

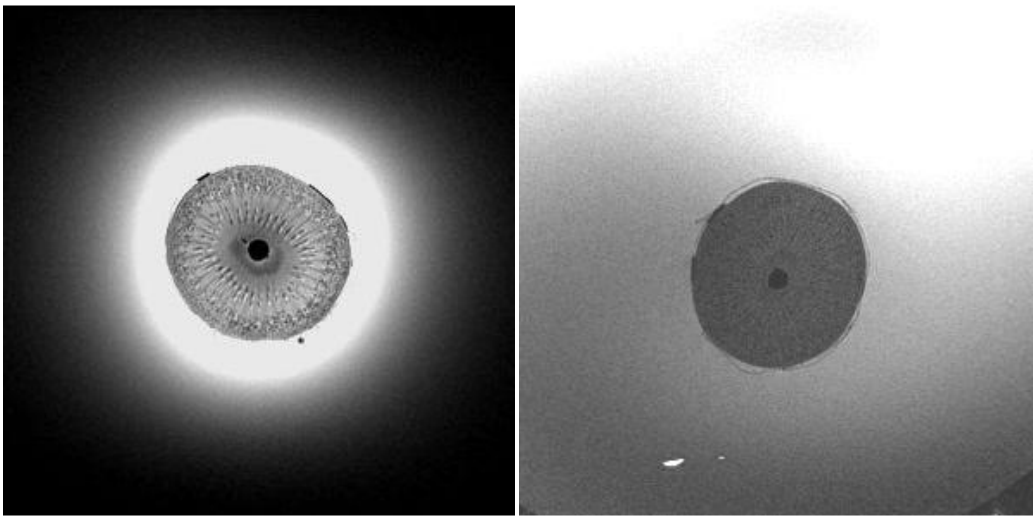

Figure 2.46: Image obtained endocervical loopless probe.T1-weighted Turbo Spin Echo images of a kiwi submerged in a copper sulphate solution. The imaging parameters are: TR=800, TE=12, slice thickness=2.6mm, FoV=150mm x 150mm, BW=260Hz/pixel. Images were acquired using (A) with the proposed endocervical coil and (B) with a Siemens body matrix coil.

2.5 DISCUSSION

In the phantom experiments explained above, it was shown that the endocervical loopless probe successfully compensated for the null region in the center of the loop. The image quality achieved by this design can be further improved by using it in combination with an external coil, which may result in extended FOV and increased SNR. Finally, in order to completely understand the performance of the design, animal experiment should be conducted.

2.6 CONCLUSION

In this chapter, development of the two channel endocervical MR coil for HDRB was explained. This coil was embedded inside a Nucletron CT/MR ring applicator without interfering with its functionality. It also provided high quality MR images of the cervix, which can be used in assisting accrued radiation dose calculation for HDRB. In order to test the performance of the proposed endocervical coil and compare its performance with Siemens body matrix coil, kiwi was used as a model of the cervix in phantom experiments. So far, Siemens body matrix coil was accepted as a gold standard in imaging of the cervix; however, the proposed coil was more successful in showing the anatomical details on the kiwi images. This result is also supported by the SNR calculation of the phantom.

Chapter 3

3. MRI GUIDEWIRE and MR EP CATHETER for the TREATMENT of ATRIAL FIBRILLATION (AF)

3.1 Introduction

Atrial Fibrillation (AF) is a disorder caused by the arrhythmia in the two upper chambers (the atria) of the heart [25]. The statistics show that the AF is the most common type of arrhythmia which increases the stroke risk up to 7 folds among the general population [26]. At the age 40, the risk of the AF is as common as 26% among the men and %23 among the women. At the age of 80, on the other hand, the risk of the AF is 22.7% for the men and 21.6% for the women [27].

In patients with the AF, the upper atria are fibrillated due to the disrupted electrical activities in the region. In a heart with a normal beating rate, the electrical activities originate from two contraction centers: the sinoatrial (SA) node and the atrioventricular (AV) node. The electrical signal first triggers the sinoatrial (SA) node to contract and then it is transferred through the electrically active cells to the atrioventricular (AV) node. The synchronized activities of these two centers result in rhythmic heart beat. In patients suffering from the AF, the electrical impulses generated by the SA node are distorted by the disorganized electrical impulses causing an arrhythmia, which might then increase the risk of the stroke as the blood may pool and form clots [28].

A common way of treatment for the AF patients is by medication, which is rarely enough for a complete cure [29]. In case the drug therapy is not successful, a surgical operation called Cox Maze is made [25]. The Cox Maze operation is performed with multiple linear and transmural incisions to isolate the electrical activities in the atrial chamber and avoid abnormal electrical interactions with the environment. The procedure, however, is not common due to its technical difficulty and the significant operative risks it possesses [30]. Alternatively, a less invasive, catheter-based X-ray fluoroscopy guided RF ablation method was developed. In this method RF energy is delivered to the tissues which results in incision like scars. Although this method was relatively more promising, because of the poor soft tissue contrast, difficulties were experienced in creating linear and continuous lesions. Moreover these result in an extremely long procedure time, inappropriate ablation and excessive X-ray exposure both for the patients and the surgeons [31]. The limitations described above necessitate the development of a new method in the treatment of the AF.

An MRI technique has been proposed as a fair alternative for the RF ablation since it offers several attractive features for the interventionalist. First, the heart and the landmarks could be visualized during the procedure. This anatomical information is crucial for the identification of the ablation sites of the AF [32]. Second, the MRI offers three-dimensional visualization of the cardiac chambers and the thermal lesions of the ablated tissue. Since the lesions are invisible in the x-ray fluoroscopy, it is very difficult to decide if the tissue is completely ablated. An incomplete ablation could even make the entire operation unsuccessful [33]. Third, unlike the RF ablation, the MRI carries no risk of exposure to the ionizing radiation for the patient and the operator. Although most of the patients are exposed to the radiation once in their lives, the operators experience the exposure multiple times, which might cause serious consequences.

There is a certain number of research on the development of catheters for the MRI guided RF ablation especially for the cardiovascular diseases. In 2005, Bensheng Qui et al., developed a 0.0014-inch MRI guidewire with the same physical characteristics of the endovascular guidewire, which provided high resolution intravascular MR images [34]. In 2002, R. C. Susil et al., developed a multifunctional interventional device which contained an electrophysiology catheter and an MR imaging catheter in the same package [35]. In this thesis work we redesign and develop an MRI EP catheter and an MRI guidewire to carry the technology further and be able to perform the RF ablation under the guidance of the MRI.

The catheter needs to meet multiple criteria to be used in the EP interventions under the MRI. The entire catheter body must be easy to visualize and track under the MRI and at the same time, catheter must record the intracardiac electrocardiogram (IECG) signal with minimum coupled noise. This is very important as the MR room is a very noisy environment and this noise needs to be paid special attention to. In this study, we develop a combined MRI EP catheter which records the IECG signal and receives the MR signal simultaneously for active catheter tracing. The catheter has two electrically isolated electrodes for the IECG recording and a loopless antenna [1] placed into it to provide whole shaft visibility.

Intravascular guidewire for interventional MRI procedures must have imaging as well as mechanical capabilities. The device must be able to navigate diseased structure without causing any disruption to it. Furthermore, it should keep the mechanical integrity. The device tip requires special attention due to the risk of disintegrating diseased tissue. And finally the device body must be able to deliver a range of interventional devices with different physical properties [36]. Therefore, we develop a guidewire for interventional cardiovascular MRI that possesses mechanical characteristics necessary for the complex interventional procedures and the loopless antenna for whole shaft visibility in a compact 0.035-inch package.

3.2 MANUFACTURING PRINCIPLES

3.2.1 GUIDEWIRE

3.2.1.1 METHOD

The guidewire included a loopless antenna so that it can be used to obtain high resolution MR images. The size and the handling properties of the guidewire were also similar to the common intravascular guidewire. Similar to a previously designed endocervical loopless probe, the design of the MRI guidewire was based on a coaxial cable, with extended inner conductor. The combination of the extended inner conductor and the outer conductor enable MR signal reception (Figure 3.1). The guidewire was designed as 0.035-inch diameter wide and 112 cm long, and was constructed with one receiver channel. Basically the MRI guidewire consist of three main parts; loopless antenna, balun and decoupling circuit. The guidewire is designed to have the loopless antenna at the distal end and a balun and decoupling circuits at the proximal end. These electrical circuits will be explained in detail in the following sections.

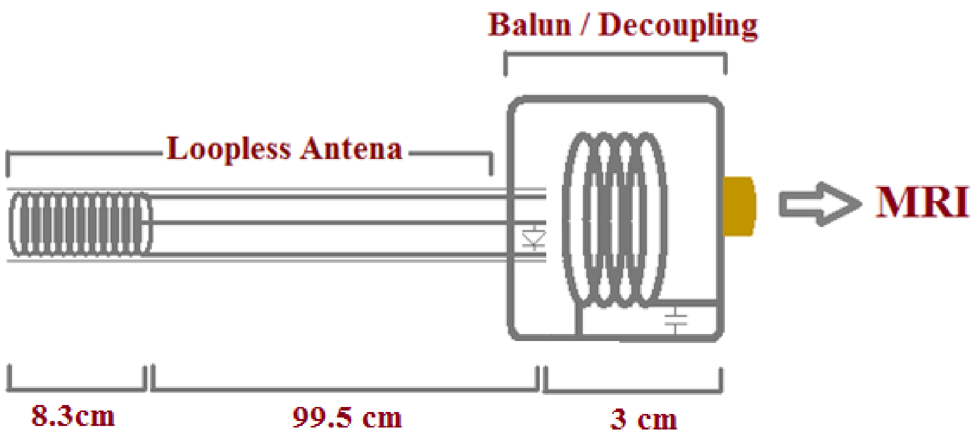

Figure 3.1: The basic design of a 0.035-inch MRI guidewire with a loopless antenna on one end and a balun/decoupling box on the other end.

The detailed design of the proposed guidewire is shown in Figure 3.2. All the materials were chosen to match the characteristics of a common X-ray catheter. First, an 8.3mm long and 0.89mm wide distal solenoid coil (Figure 3.2-2) was attached to a 0.25mm gold plated nitinol rod (Epflex, Dettingen, Germany) over the entire length of the guidewire (Figure 3.2-3). This nitinol rod, which served as the inner conductor of the coaxial portion of the loopless antenna, was then inserted into a polytetrafluoroethylene tubing (PTFE, Adtech, Gloucestershire, England) with 0.4 mm inner and 0.7 mm outer diameter (Figure

3.2-4). The PTFE tubing enabled isolation between the inner and outer conductor of the coaxial portion as well as providing circuit stability. Next, this portion was inserted through a nitinol hypotube (Vascotube, Birkenfeld, Germany) with 0.78 mm inner and 0.89 mm outer diameter (Figure 3.2-5), which formed the outer conductor of the coaxial portion of the loopless antenna. The whole assembly was finally covered with polyester heatshrink (Advanced Polymer, Salem, NH) with 0.96 mm outer diameter and 0.006 mm wall thickness (Figure 3.2-1). At this stage the construction of the loopless antenna was complete. The free end of the solenoid coil was sealed with liquid silicon and the antenna was connected to the balun and decoupling circuit. Construction of these circuits will be explained in detail in the following sections. At the final step, a nonmagnetic female SMA connector (Kun Shan Xiangde Precesion Electronics, Shenzhen, China) was used to connect the guidewire to the MR scanner.

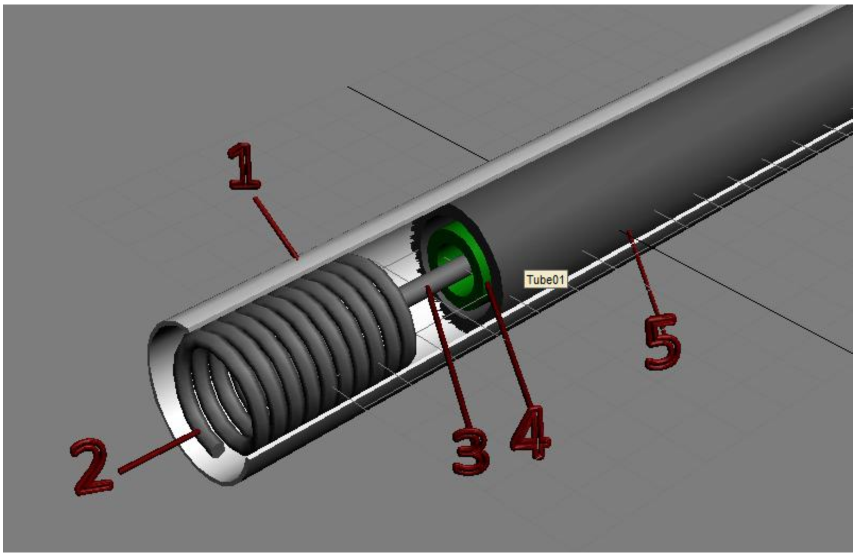

Figure 3.2: Guidewire schematic: (1) Heat-shrink tubing, (2) solenoid coil, (3) inner conductor rode, (4) PTFE tubing, (5) nitinol hypotube.

3.2.1.2 MATERIALS

Solenoid Coil

The mechanical and imaging performance of the intravascular devices for the interventional MRI are strictly dependent on the solenoid coil design. As the device tip is more likely to injure or perforate the target tissue, it should be made up of superelastic, MRI compatible materials such as nitinol. Although the superelasticity of the nitinol satisfy the mechanical requirements, its electrical conductivity (σ=1 x 10^6 S/m) is too low to achieve high quality MR imaging. When transmitted through the MRI guidewire, the MR signal was attenuated due to the electrical resistance of the thin coaxial cable. To solve this problem, the solenoid coil can be modified by plating highly electrically conductive materials, such as silver (σ=6.28 x 10^7 S/m), cupper (σ=5.8 x 10^7 S/m) or gold (σ=4.26 x 10^7 S/m), on the surface of the nitinol. Although, the electric conductivity of the silver and copper is higher than gold, because of their high corrosions we decide to use gold for plating the nitinol.

The depth of the RF penetration on the surface of the inner conductor depends on the RF frequency and the electrical conductivity of the materials to be used, and is limited to a few microns. The RF skin depth of the gold plating at 123.23 MHz was calculated as 6.94 μm, using the following formula,

$$\delta s = \sqrt{\frac{2}{\omega\, \mu\, \sigma}}$$

where μ is the permeability ($4 \times \pi \times 10^{-7}$ H/m), σ is the conductivity of the gold ($\sigma = 4.26 \times 10^{-7}$ S/m) and ω is the radian frequency ($2 \times \pi \times 123.23 \times 10^{6}$ rad/sec). Thus, we can decrease the electrical resistance by plating highly conductive metal such as gold, on the outer surface of an inner conductor, which was made up of superelastic materials.

Taking the data above into consideration, a solenoid coil was designed as shown in Figure 3.3. A 0.25 mm nitinol rod is initially covered with 7 μm gold and then with 2 μm PTFE for the electrical isolation. Next, one end of the rod was curled up making a coil of 0.89mm diameter and 10 cm length. The other end of the rod was left 150 cm long to be used as an inner conductor of the coaxial portion. The lengths of the inner conductor and coil would be optimized during the electrical design. One of the main advantages of this design is the absence of the welding between the coil and the inner conductor of the coaxial portion. This improves the mechanical properties of the guidewire significantly as the junction (Figure 3.3) point could be broken during the procedure very easily. A picture of the constructed solenoid coil is shown in Figure 3.4

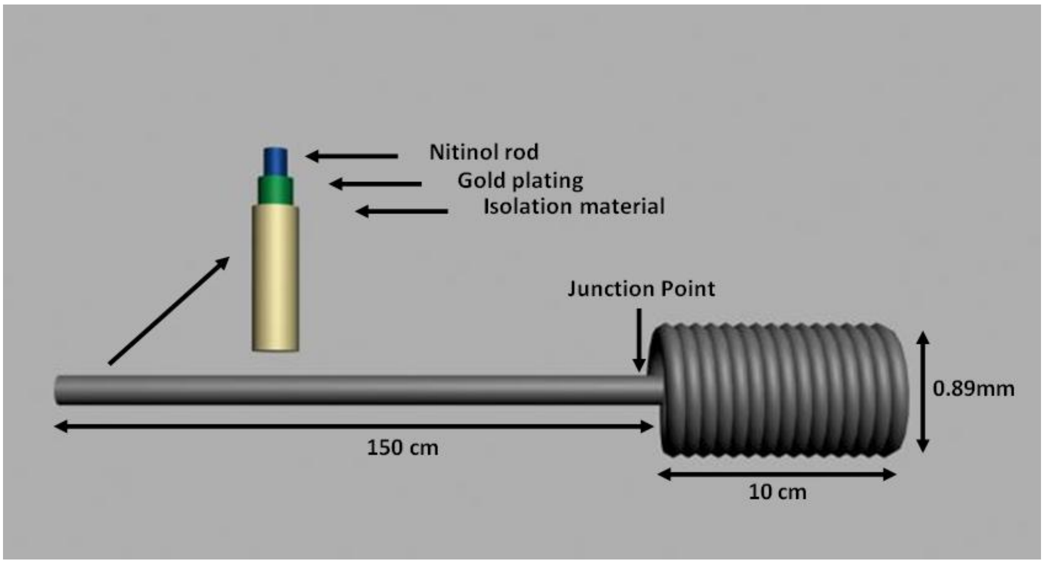

Figure 3.3: Design of the solenoid coil for the MRI guidewire.

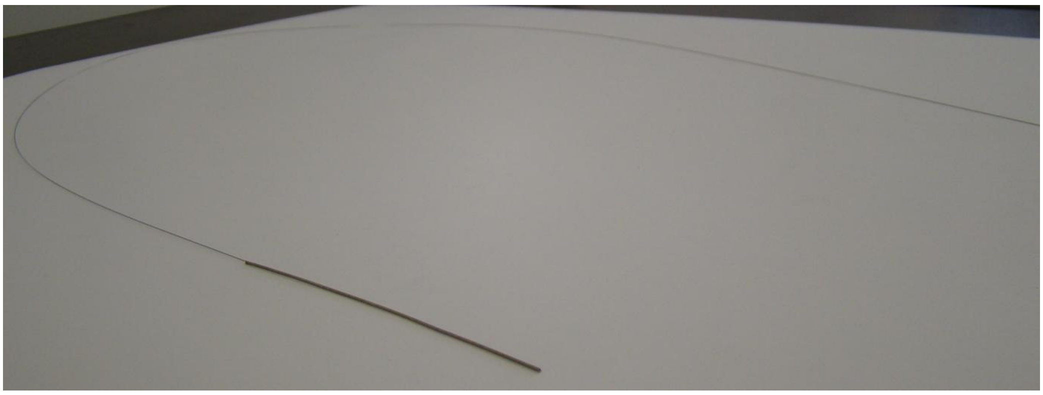

Figure 3.4: A picture of the solenoid coil used for the guidewire.

Polytetrafluoroethylene (PTFE)

The polytetrafluoroethylene tubing (PTFE, Adtech, Gloucestershire, England) with 0.4 mm inner and 0.7 mm outer diameter (Figure 3.2-4) was used to provide isolation between the inner and the outer conductors of the coaxial portion of the loopless antenna. This tube provides circuit stability of the guidewire. The PTFE has excellent dielectric properties (ϵ_r=2 or less), especially under high RF, which makes it perfectly suitable for being used as an insulator in cables. Another advantage of the PTFE is its low friction constant and therefore it simplifies the assembly of the guidewire. As the inner diameter of the nitinol hypotube is 0.78 mm and the outer diameter of the PTFE tube is 0.7 mm, it is very important to use a material with a low friction coefficient so that the polymer tube could be efficiently inserted through the nitinol hypotube. A picture of the PTFE tube is shown in Figure 3.5.

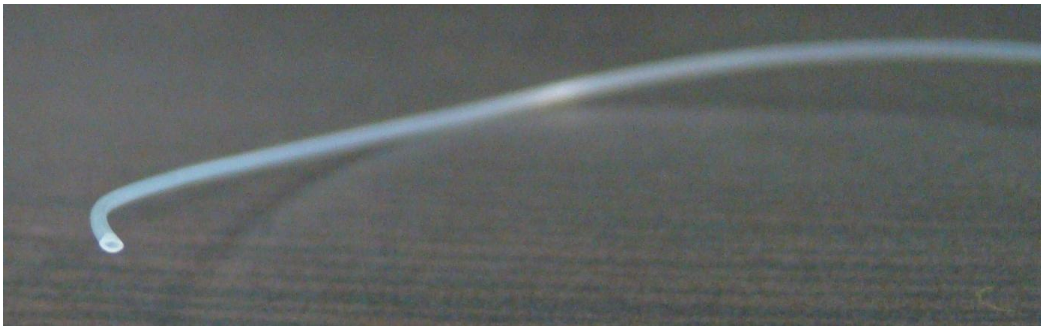

Figure 3.5: A picture of the PTFE tubing used as an isolator between the inner and outer conductor of the coaxial portion of the MRI guidewire.

Heat Shrink Tubing

Polyester heat-shrink tubing (Advanced Polymer, Salem, NH) with 0.96 mm outer diameter, 0.006 mm wall size and an extension ratio of 2/3 was used as an outer isolator to provide both electrical and liquid isolation. This is one of the thinnest heat-shrink tubing in the world. This tubing provides integrity to the guidewire combining all components together. A picture of the heat-shrink tubing is shown in the following figure.

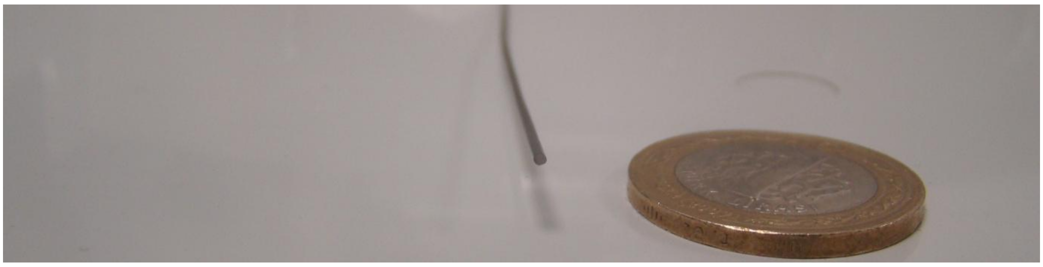

Figure 3.6: A picture of the polyester heat-shrink tubing with 0.96 mm outer diameter and 0.006 mm wall thickness.

Nitinol Hypotube

Nitinol superelastic hypotube (Vascotube, Birkenfeld, Germany) with 0.76 mm inner, 0.89 mm outer diameter and 150 cm length was used as an outer conductor of the coaxial portion of the loopless antenna. The superelasticity of this nitinol tube provides the required mechanical properties of an MRI guidewire, but the low conductivity of the nitinol may cause a decrease in the SNR. Although, the image performance of the MRI guidewire satisfied the clinical requirements, it is recommended to plate its inner surface with the gold. A picture of the used nitinol hypotube is shown in Figure 3.7.

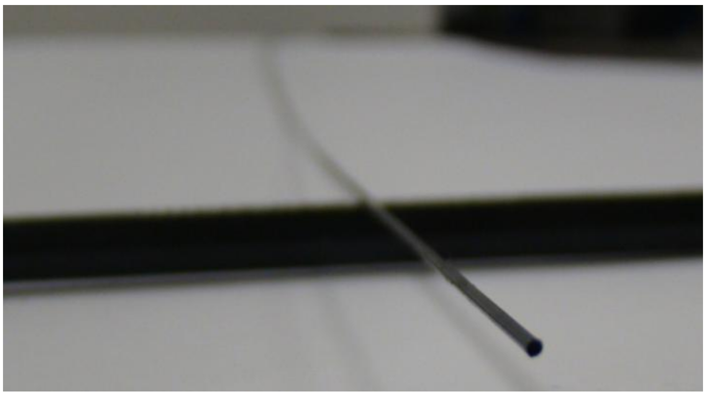

Figure 3.7: A picture on the superelastic nitinol hypotube used as an outer conductor of the MRI guidewire.

A picture of the constructed guidewire before being covered by heat shrink is given in Figure 3.8. The length of the solenoid coil in the picture is not optimized yet.

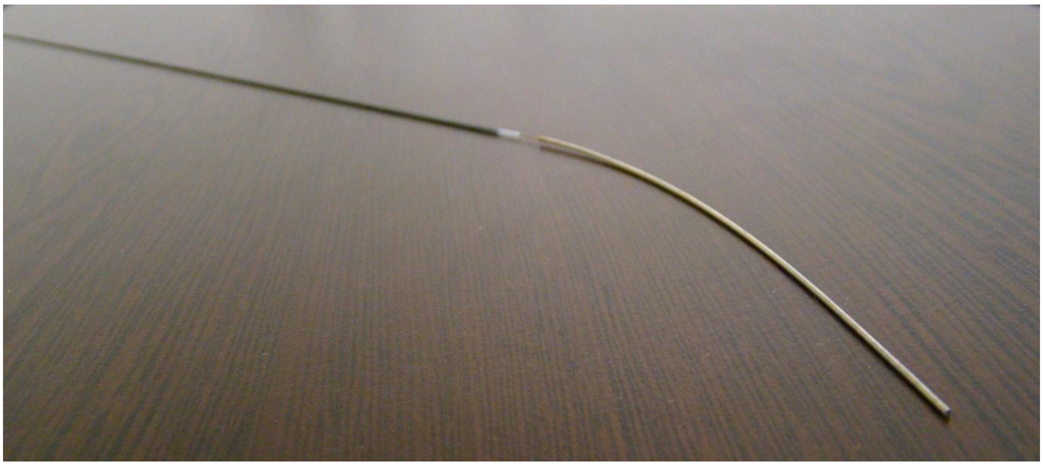

Figure 3.8: A picture of the assembled guidewire before being covered with heat shrink.

3.2.1.3 Electrical Circuit Design

Currently, since the MRI guidewire is a thin loopless antenna, its electric design is very similar to the endocervical MRI loopless probe. It consists of balun, matching/tunning and decoupling circuits. All the functions of these circuits were explained in detail in the previous chapter.

Balun

For the MRI guidewire, we used a very similar design to the one we used for the endocervical MR imaging probe except small differences. This time a 3mm cupper semi-rigid coaxial cable (Rosenberger micro-coax, Berkshire, UK) was used for the construction of the balun. The semi-rigid coaxial cable was curled up 4 times to create a solenoid coil with 2.7 cm outer diameter and 2.5 cm length. To build a balun, the solenoid coil was initially inserted into a cylindrical copper box (same as the one used for the endocervical probe). Then the copper box was shortened to the outer conductor at one end. The outer conductor and the outer shield would make a transmission line. By adjusting the length of this transmission line to the quarter wavelength, the short impedance at one end would be transformed to open impedance at the other end of the balun. Since this side would be connected to the guidewire, the flow of unbalanced currents on the outer conductor would be prevented. We followed the same steps as we did for the construction of the balun for endocervical loopless probe. The impedance of the constructed balun was measured as 3 k ohms. The balun was placed to the proximal end of the guidewire. A simple picture of the constructed balun circuit is shown in Figure 3.9.

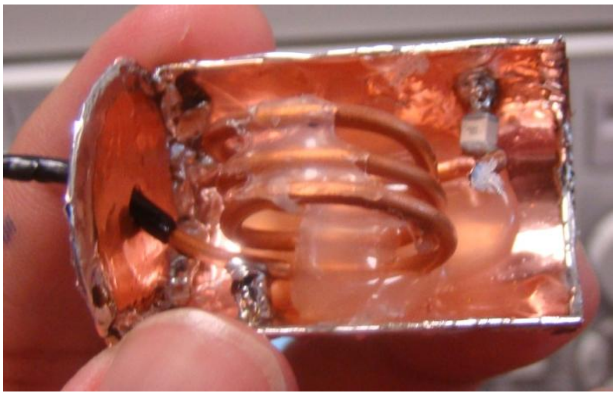

Figure 3.9: A picture of the inner construction of the balun that was built for the MRI guidewire.

Matching and Tunning Circuit

The loopless antenna's impedance has to be matched to 50 ohms at 123.23 MHz (Larmor frequency) to avoid reflections. As explained in the previous chapters, the reflections seen from the coil side due to a large non-zero reflection coefficient may cause losses on the transmission line and therefore increase the noise of the images acquired by this design. Therefore, it is crucial that the coil is well matched to the characteristic impedance of the coaxial portion of the guidewire. Again in this design we didn't use an extra tuning and matching circuits as the impedance of the solenoid coil was optimized to a very close value to the characteristic impedance.

In order to understand the performance of the design, we measured the antenna impedance of the guidewire under the loading conditions similar to the cardiac vessel. A semi cylindrical phantom filled with saline gel solution (0.35% NaCl) was used to simulate loading conditions ($\epsilon r = 77$, $\sigma = 0.6$ S/m). In order to optimize the impedance of the solenoid coil, the length of the coil was shortened until minimal real impedance was observed at 123.23 MHz. The minimum real impedance was measured as 68 ohms when the length of the coil was 8.3 cm. Then the characteristic impedance of the coaxial portion of the loopless antenna was measured as 61 ohms, using the same method that was used for the endocervical loopless probe. As this value is very close to the impedance of the solenoid coil there is no need for the additional tuning and matching circuit.

Decoupling

As the MR scanner transmits RF waves, current is induced on the matched and tuned coil. This induced current creates additional magnetic field and changes the orientation of the spins around it, which results in a decoupling artifact on the MR images. In order to avoid this situation, the loopless coil should be decoupled so that no current is induced during the transmission of RF pulses.

For the decoupling of the MRI guidewire we use a very similar method to the one we used for the endocervical loopless probe. The total length of the coaxial portion of the guidewire was adjusted to the $3\lambda/4$ wavelength which was 99.5 cm at 123.23 MHz. Subsequently a non-magnetic PIN diode (MA4P7461F-1072T, Macom, Lowell, Massachusetts) was placed at the proximal end of the coaxial portion of the loopless coil (Figure 3.10). Note that during the radio-frequency pulse transmission, the scanners provide a DC bias current, the PIN diode turns on and its RF impedance becomes low. Three quarter wavelength coaxial cable transforms this low impedance value to the high impedance value at the distal end and hence it serves reduce the induced RF currents on the guidewire. The impedance value may vary depending on the loss of the coaxial portion. Notably, the effectiveness of the decoupling circuit highly depends on this impedance.

In order to understand the performance of the decoupling circuit, distal end of the coaxial portion was shortened and the impedance detected from the proximal end was measured with network analyzer, which was 524 ohms. This value is significantly lower than the measured decoupling impedance of the endocervical loopless probe. The reason for the decrease is the loss of the coaxial portion of the loopless antenna. The performance of this decupling circuit was then tested by a heating experiment, which is presented in the following section.

A picture of the complete MRI guidewire is shown in Figure 3.11.

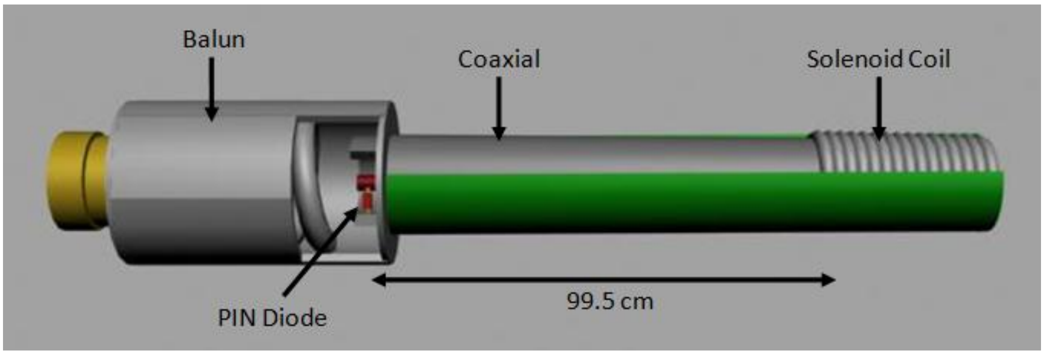

Figure 3.10: A drawing showing the scheme of the decoupling circuit used for the MRI guidewire.

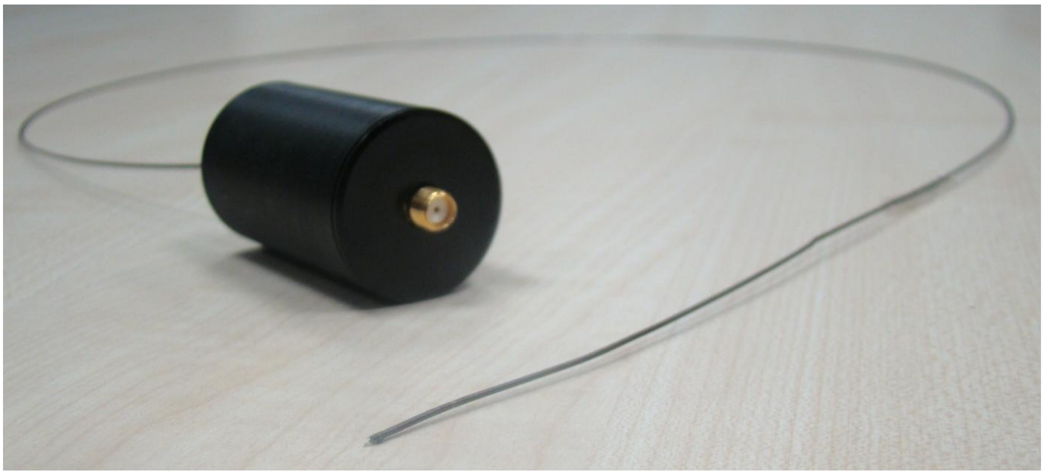

Figure 3.11: A picture of the complete MRI guidewire.

3.2.2 Combined MR EP Catheter

3.2.2.1 Materials and Methods

Typical structure of a common EP catheter is shown in Figure 3.12a. The catheter is formed of a medical tube, which is the shaft of the catheter, and two electrodes (one tip and one ring), which are located at the distal end of the catheter. These two electrodes are connected to the connector at the proximal end via two wires. The electrical structure of the catheter is shown in the Figure 3.12 b. In this study, we slightly modified the common structure of the EP catheter so that all the components used were nonmagnetic. Also to be able to bring in visualization and tracking capabilities to the catheter, we place a loopless antenna inside, which provides high SNR in a local region.

To this end, a solenoid coil with an extended proximal end was placed inside the catheter. This extended proximal wire forms the inner conductor of the coaxial portion of the loopless antenna. Additionally, a copper breaded tube was used to form the outer conductor of the loopless antenna. The wire leads were connected to the electrodes via resistors. The resistors were specially connected in series with the surface and tip electrodes, to improve the safety and decrease an excessive heating during the RF transmission. Furthermore, in order to decrease the coupled noise on the intracardiac electrocardiogram (IECG) signal, the wire leads were twisted.

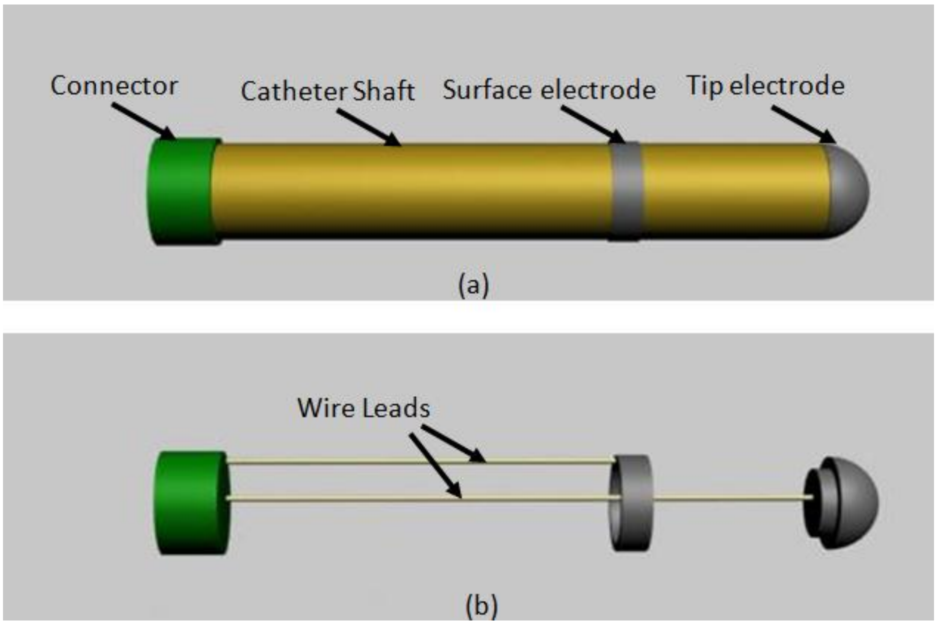

Figure 3.12: (A) Typical structure of the common EP catheter. (B) Typical Electrical structure of the common EP catheter.

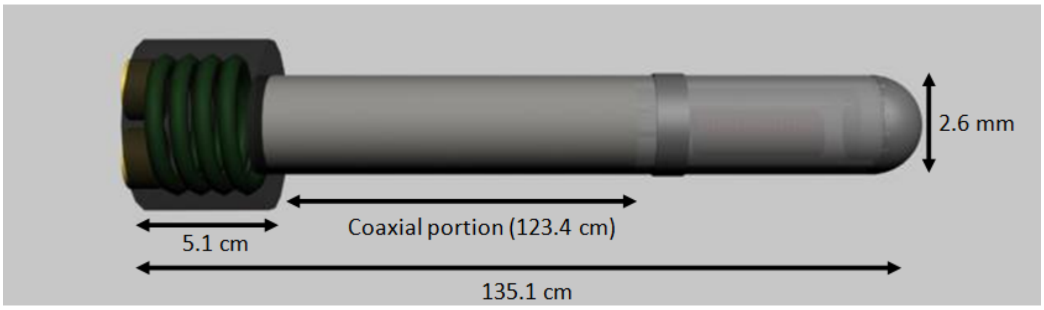

Figure 3.13: A simple drawing showing the dimensions of the MR EP catheter.

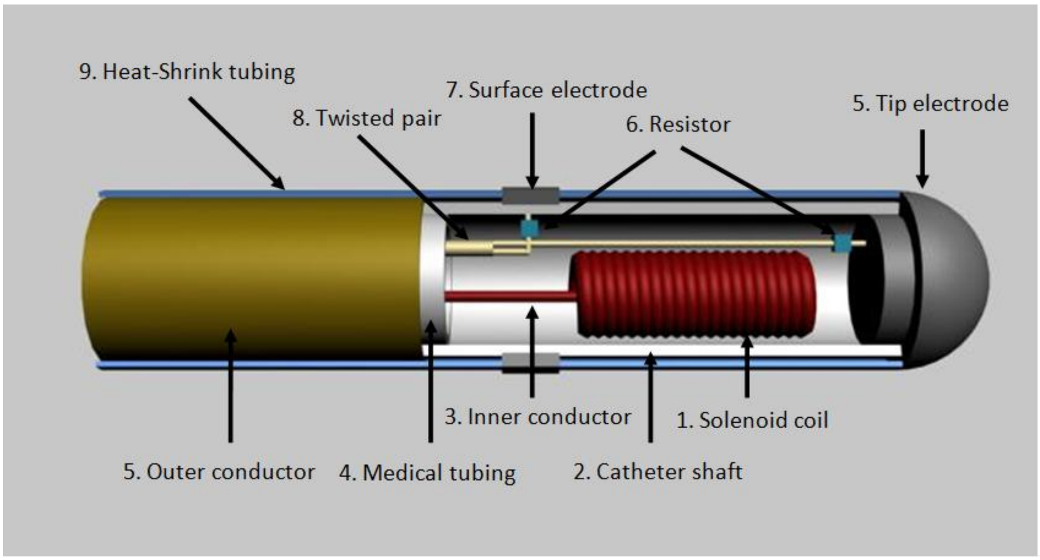

Figure 3.14: A detailed design of distal end of the MR EP catheter.

The detailed design of the proposed MR EP catheter is shown in Figure 3.14. The MR EP catheter was designed as 2.6 mm diameter wide and 135.1 cm long, and constricted with two separated electrodes (Figure 3.13). The distal solenoid coil, on the other hand, was 5.1 cm long and 1.8 mm wide (Fig. 3.14-1). The coil was attached to a 0.4 mm coated cupper wire (Newark, Palatine, IL) over the entire length of the EP catheter (Figure 3.14-3). This wire constitutes the inner conductor of the coaxial portion of the loopless antenna and was inserted in through a polytetrafluoroethylene tubing (PTFE, Adtech, Gloucestershire, England), which has a 1 mm inner and a 1.4 mm outer diameter (Figure 3.14-4). The PTFE tube is required to fix the coil and the wires in their place. Next, the entire assembly was inserted in through another polytetrafluoroethylene tubing (PTFE, Adtech, Gloucestershire, England) with a 1.58 mm inner and a 2.4 mm outer diameter (Figure 3.14-4), which constitutes the shaft of the catheter. The catheter shaft was then inserted into a copper breaded tube (Newark, Palatine, IL), which forms the outer conductor of the coaxial potion. Two handmade silver electrodes (Yusuf Kuyumculuk, Ankara Turkey) was placed on the catheter shaft (Figure 3.14-5,7) and soldered to the twisted pair (Figure 3.14-8) via 10 k nonmagnetic resistors (SRT Resistor Technology, Cadolzburg, Germany) (Figure 3.14-6). Finally the whole assembly including the surface electrode was covered with polyester heatshrink tubing (Advanced Polymer, Salem, NH) 0.07 mm wall thickness (Figure 3.14-9). The heatshrink tubing was cut at the place of the surface electrode and the edges were isolated with glue.

The catheter was connected to the signal splitting box (Figure 3.15), which includes decoupling and balun circuits. The signal splitting box receives IECG signal via twisted pair from the electrodes and MR imaging signals from the loopless antenna. The IECG signal was directly connected to the SMA connector at the proximal end of the balun, which is then transformed to the ECG amplifier after being filtered by the low-pass filter (LPF). The MR imaging signal, on the other hand, was first connected to the decoupling and balun circuits, then to the SMA connector and finally reached the MR scanner.

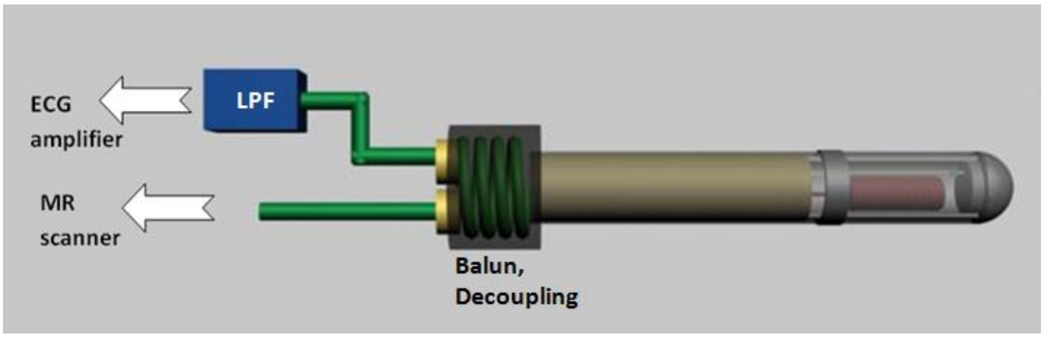

Figure 3.15: A schematic diagram of the connection diagram of the EP MR catheter. The MR Signal is decoupled matched and connected to the balun and the transferred to the MR scanner. The leads carrying the IECG signal are directly connected to the SMA connector at the proximal end of the catheter.

3.2.2.1 Electrical Circuit Design

Matching

The electrical design of the MR EP catheter is very much like the endocervical loopless probe. Similar to it, the impedance of the solenoid coil was optimized to a value in the vicinity of 50 ohms. The impedance of the antenna was measured as 58 ohms under the loading conditions of the cardiovascular veins. The characteristic impedance of the coaxial portion of the MR EP catheter was adjusted to a value in the vicinity of 50 ohms. Since the impedances of the antenna and the coaxial portion are very close, there is no need for an additional matching circuit.

Balun

Balun circuit is very crucial in terms of safety issues since the electrodes have a direct contact with the tissue. Balun of the MR EP catheter was constructed by curling up the coaxial portion of the loopless antenna 4 times and then placing it into the cylindrical copper box (similar to the one used for the endocervical loopless probe). After the balun was matched to the resonance frequency, the whole assembly was put into a plastic cylindrical box. The balun was then placed at the proximal end of the coaxial cable and its impedance was measured as 2.3k ohms at Larmor frequency.

Decoupling

As mentioned before, safety is a major concern in the MR EP catheter use as the electrodes have direct contact with the tissue. The main threat is the excessive heating, which could be prevented by a high performance decoupling circuit. The performance of this decoupling circuit was tested by the heating experiments, the results of which are explained in the following sections. The decoupling circuit was constructed by adjusting the length of the coaxial portion of the loopless antenna to the $3\lambda/4$ and placing a PIN diode (Macom) at the proximal end.

Analog Low Pass Filter (LPF)

The MR room is a very noisy environment, so a significant noise is coupled to the IECG signal. Generally, the main sources of the noise are the RF and gradient fields. The bandwidth of the RF signal is very high compared to the bandwidth of the IECG signal, consequently we tried to minimize the high frequency RF noise by using a simple 5 stage RC LPF with cutoff at 1 kHz. The diagram of the designed filter is shown in Figure 3.16 and the frequency response of the filter is shown in Figure 3.17.

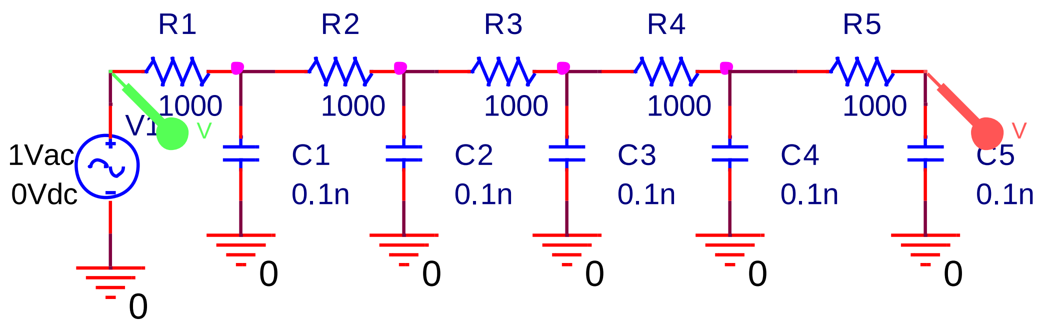

Figure 3.16: The electrical diagram of the five stages LPF.

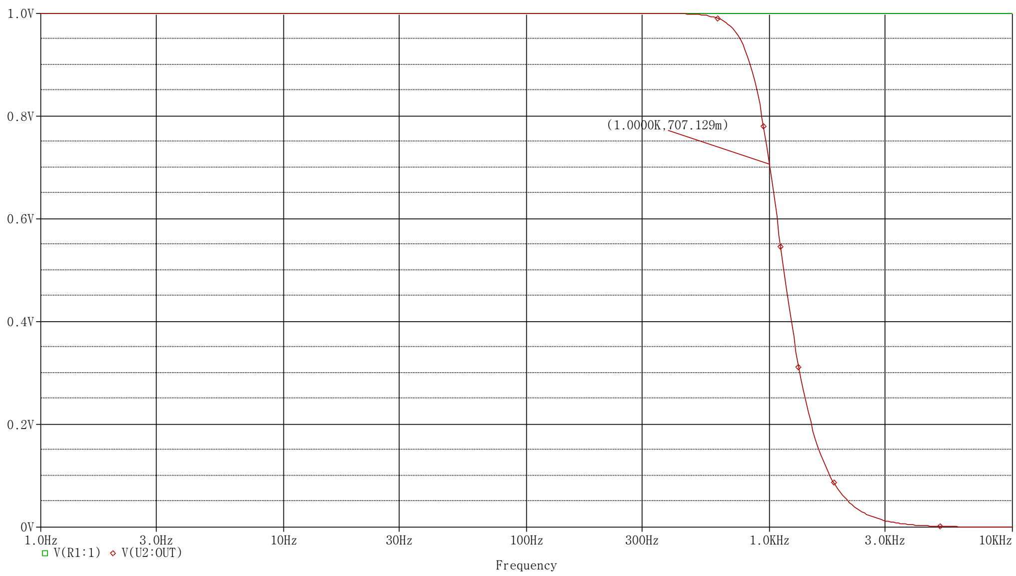

Figure 3.17: Frequency response of the 5 stages LPF.

The whole filter is made up of nonmagnetic elements since it would be used inside the MR room. The filter was constructed inside a cylindrical copper box (similar to the one used for the balun construction) using 1 kohm resistors (SRT Resistor Technology, Cadolzburg, Germany) and 0.1 nF b type capacitors (ATC). Next, this copper box was placed inside the cylindrical plastic box and the SMA connector was placed at both ends of the filter.

The picture of the proposed MR EP catheter is shown in Figure 3.18.

Figure 3.18: A picture of the proposed MR EP catheter.

3.3 EXPERIMENTS

In this section, the experimental methods for testing the performances of the MRI guidewire and MR EP catheter are explained. Similar to the endocervical loopless probe, all the heating tests were performed in a 1.5 T GE scanner for the same reason. All the imaging, ECG recording and animal tests were done in the 3 T (TimTrio) MR scanner at UMRAM. Both of the coils were connected to the MR scanner using a 2 channel preamplifier interface (Figure 2.39).

3.3.1 Heating Experiments

As explained in the previous chapter, during the RF transmission of the body coil in the interventional MRI, the body coil and metallic interventional devices may result in an electromagnetic coupling which may cause excessive heating and tissue damage. The maximum allowed temperature increase for the interventional device in the body is 2 degrees celcius, as determined by the FDA and IEC [21,22].

In order to test the temperature rise of the proposed MRI guidewire and MR EP catheter during the RF transmission, phantom experiments were conducted. To this end, we used the same phantom that was used for the heating experiment in the previous section (Figure 2.40). However this time the phantom was filled with saline gel solution (0.35% NaCl) to simulate loading conditions (ϵr = 77, σ = 0.6 S/m), simulated device advancement under MRI.

Because of the same reason that was explained in the previous chapter, MRI guidewire and the MR EP catheter were placed separately into the semi-cylindrical phantom, close to its wall. Then the phantom was placed in the bore of the scanner, against the wall (as shown in the Figure 2.41), so that the distance between the guidewire (or the catheter) to the inner wall of the MR scanner is 3 cm. Temperature rise was measured using Neoptix ReFlex four-channel signal conditioner (Neoptix, Inc., Quebec City, QC, Canada,).

The expected excessive heating points on the MRI guidewire and the MR EP catheter are different from each other. On the MRI guidewire the maximum temperature increase is expected at distal end of the coaxial portion of the loopless antenna. For this reason, the three temperature probes were placed on the MRI guidewire as shown in Figure 3.18. On the other hand, the maximum temperature increase on the MR EP catheter is expected to be on the electrodes. Thus, the temperature probes were located on the MR EP catheter as shown in Figure 3.19.

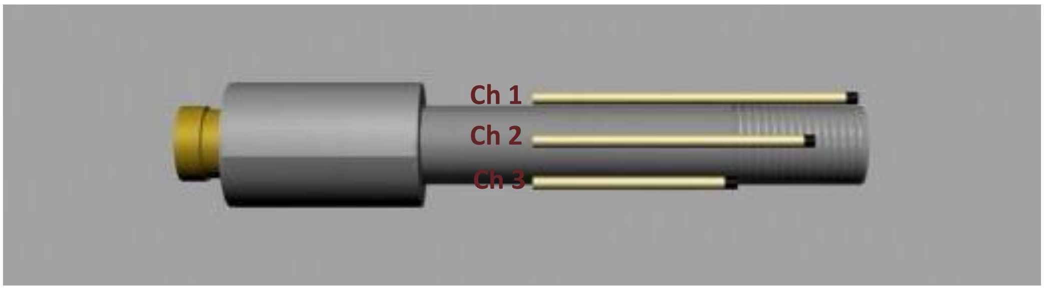

Figure 3.18: The placement of the temperature probes on the MRI guidewire.

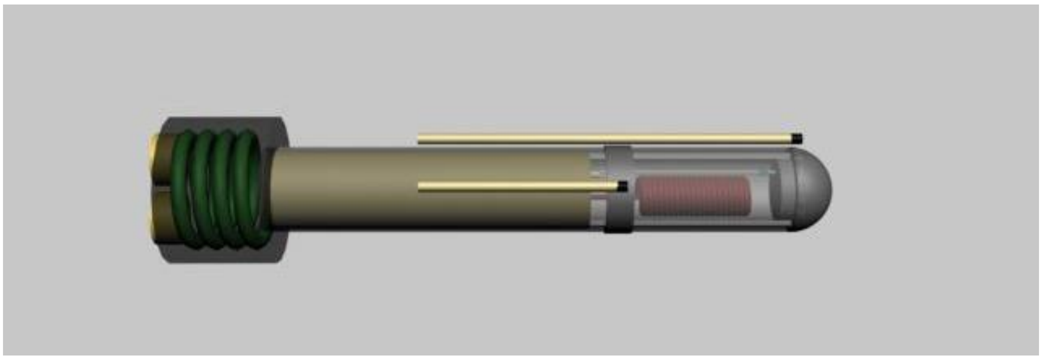

Figure 3.19: The placement of the temperature probes on the MR EP catheter.

Heating experiments of both MRI guidewire and the MR EP catheter were conducted using the same imaging parameters. SPGR pulse sequence was used with the following imaging parameters: TR = 6.25ms, flip angle = 90^{o} and scan time = 720 seconds. Other imaging parameters were TE = 1.7ms, 256x128, NEX = 60, BW = 62.5 kHz, FOV = 48cm, slice thickness = 20mm, 15 repetition.

Results

Heating Experiment Results for MRI Guidewire

The results for the heating experiment of the MRI guidewire are shown in Figure 3.20. The maximum temperature rise was observed on channel 3 and measured as 1.9 Celsius degree. This result is not surprising as the temperature probe of the channel 3 was placed at the distal end of the coaxial portion of the loopless antenna, where the field intensity is at its maximum.

Although this experiment was made under extreme conditions, which can never come true, the temperature rise of the MRI guidewire is within the safety limits determined by FDA and IEC. Consequently, the guidewire can be used safely in the interventional procedures under the MRI.

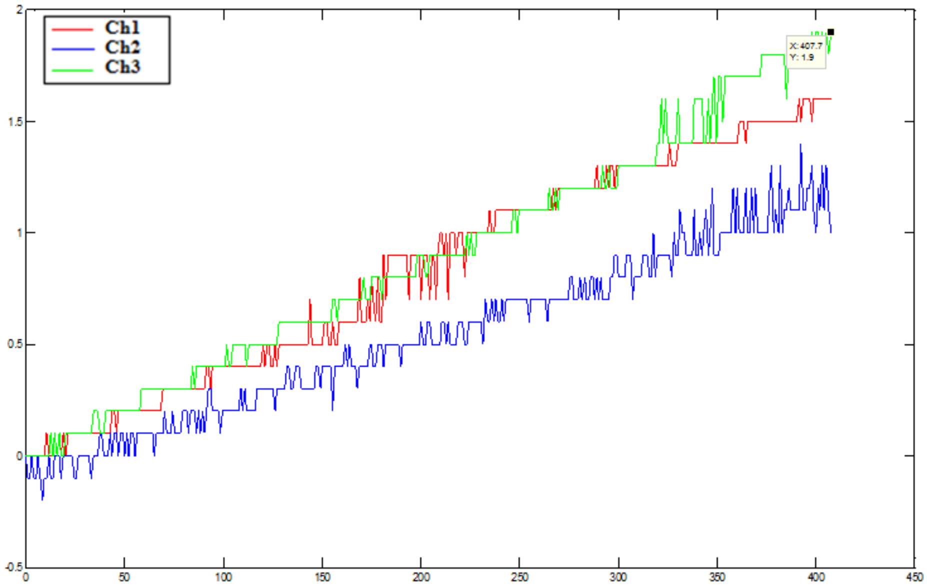

Figure 3.20: A temperature increase graph of the MRI Guidewire. The maximum temperature increase was observed on channel 3.

Heating Experiment Result for MR EP Catheter

The temperature rise of the MR EP catheter is shown in Figure 3.21. The maximum temperature rise was observed on the temperature probe connected to the ring electrode. The measured temperature rise is within the safety limits since it does not exceed the 2 degree Celsius limit determined by FDA and IEC.

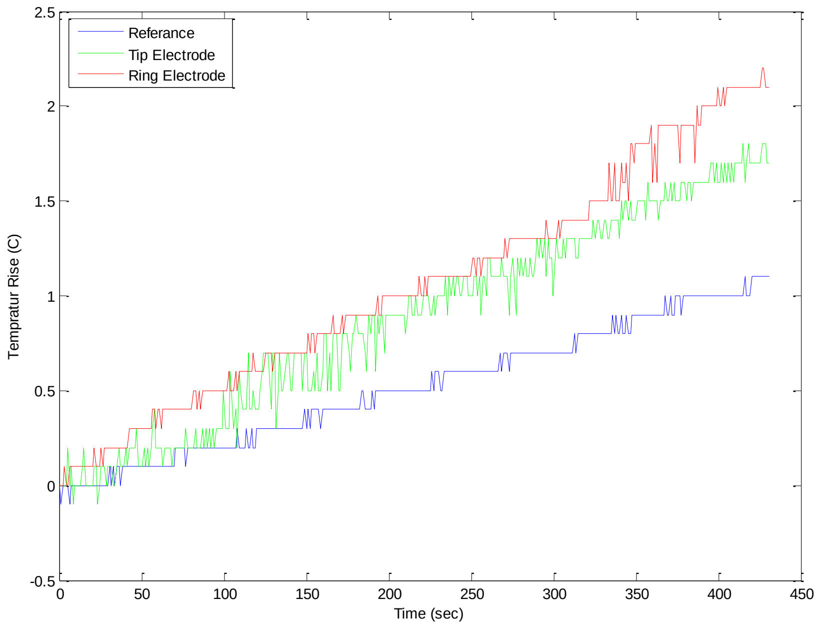

Figure 3.21: The graph for the temperature rise of the MR EP catheter.

3.3.2 Phantom imaging Experiments

To test the imaging performance of the probe, we used the same phantom that we used in heating experiments. However, this time the phantom was filled with a copper sulphate solution with similar electrical properties to the blood ($\epsilon r = 77$, $\sigma = 0.6$ S/m). Both the MRI guidewire and MR EP catheter were placed separately at center of the cylindrical phantom and the phantom was then placed at the center of the MR scanner. Both the MRI guidewire and the MR EP catheter were imaged using the following imaging parameters: Gradient Echo (GRE), TR/TE=82/4, Echo train length=1, BW=260 kHz, 256x256, NEX=1, FOV=28cm, slice thickness=5 mm.

Experiment results

A transversal image obtained using the MRI guidewire is shown in Figure 3.22-a. The image observed has the common characteristics of an image obtained by a loopless antenna: High signal was concentrated around the wire and the signal intensity decreases rapidly with the distance. Although the signal intensity of the MRI guidewire is not very high, the whole shaft of the catheter is clearly visible. The sagittal image of the guidewire is shown in Figure 3.22-b.

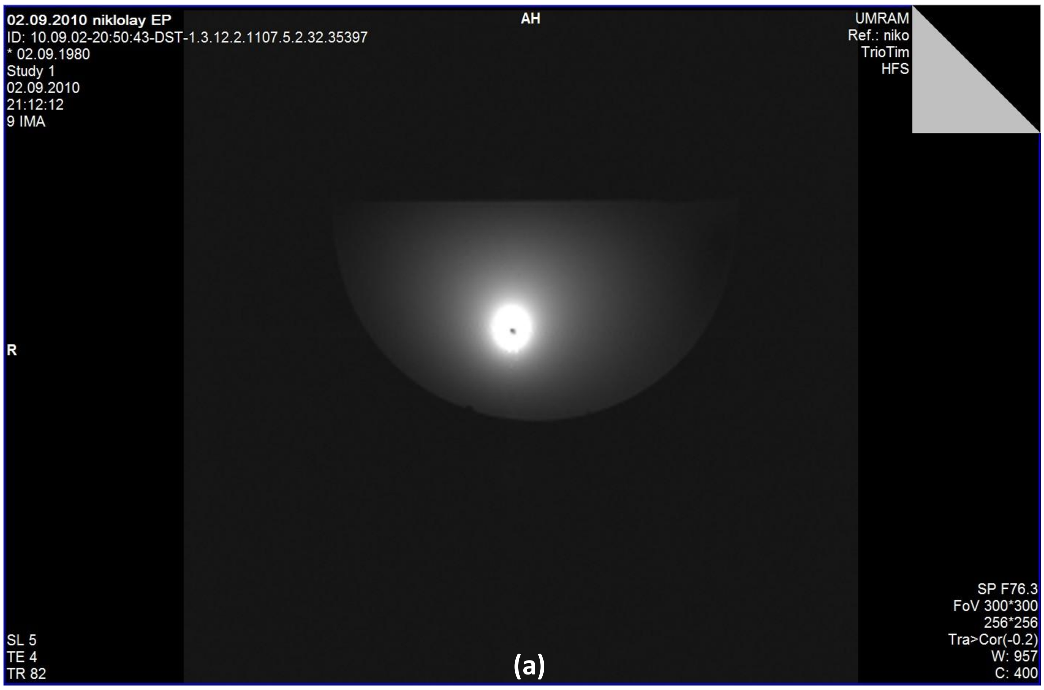

(a)

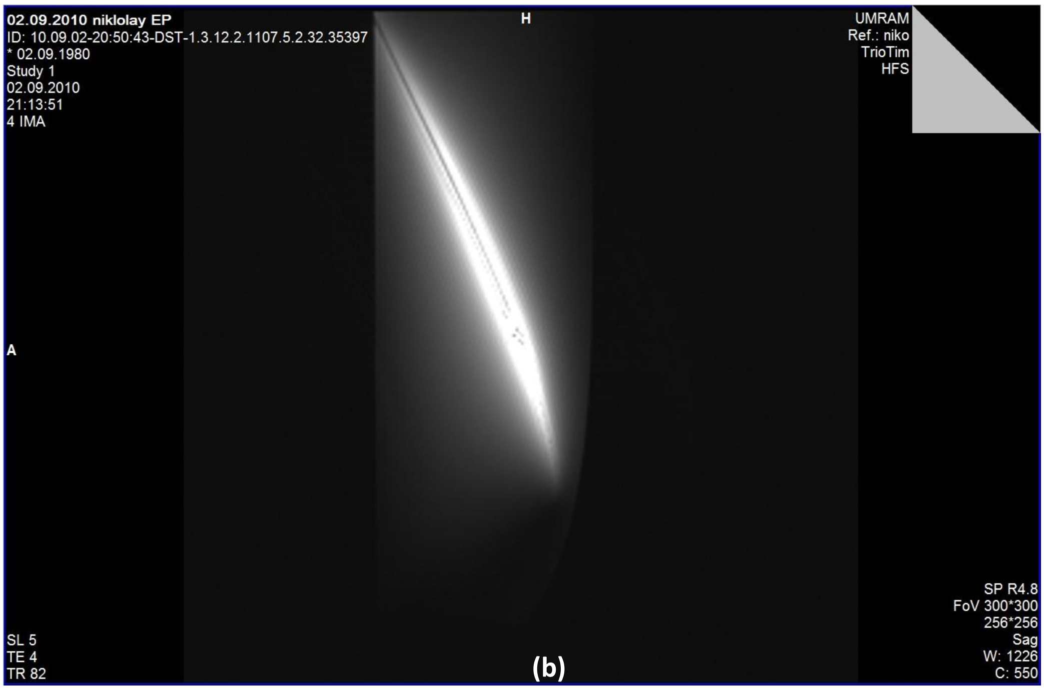

Figure 3.22: (a) Transversal image of the MRI guidewire inside the phantom. (b) A sagittal image of the guidewire inside the phantom.

A transversal and sagittal images of the MR EP catheter is shown in Figure 3.23.

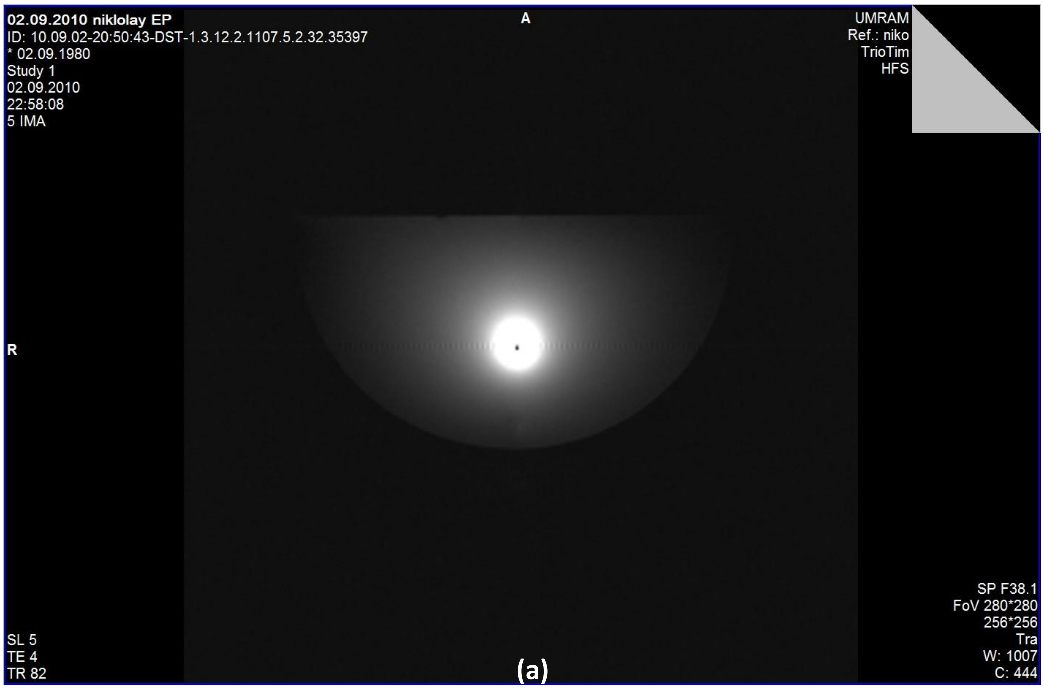

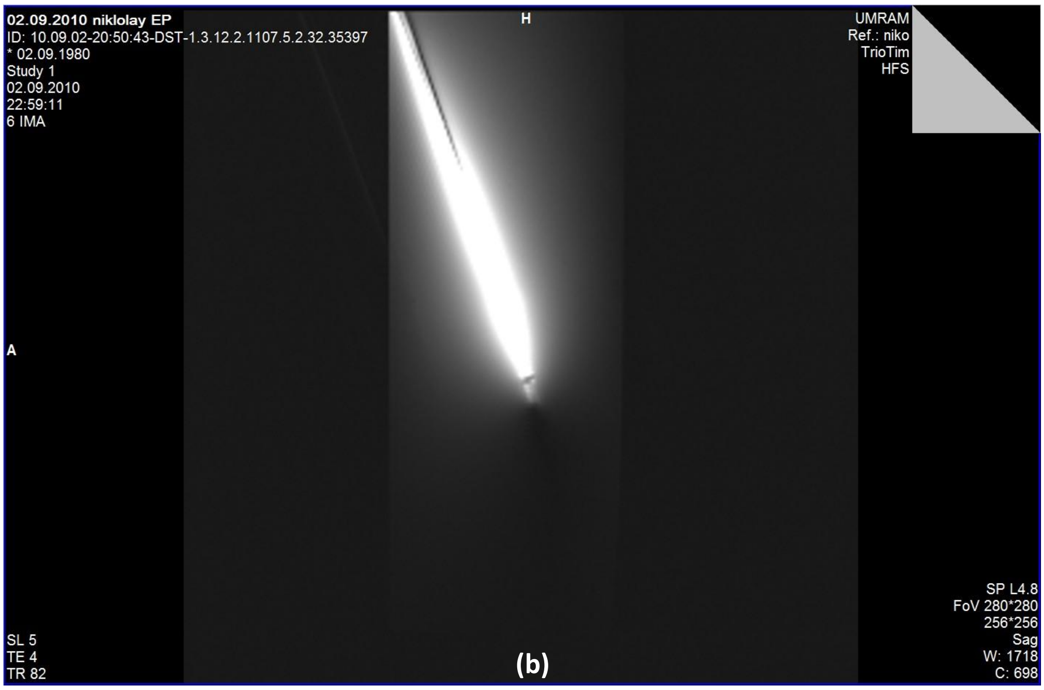

Figure 2.23: (a) Transversal image of the MR EP catheter inside the semi-cylindrical phantom. (b) A sagittal image of the MR EP catheter inside the phantom.

3.3.3 ECG Recording Experiments

Three main experiments were conducted to test the ECG recording performance of the MR EP catheter. First, the performance of the entire experimental set up was tested outside the MR room using the MR EP catheter and an ECG simulator. Second, an animal experiment was conducted outside the MR room to record ECG signal from the heart of a rabbit. Third, the MR noise coupled to the MR EP catheter was recorded inside the MR room.

First, in order to test performance of all the experimental setup and the MR EP catheter the ECG simulator was used. Second, the animal experiment was conducted outside of the MR room and ECG signal was recorded from the heart of the rabbit. Third, the MR noise coupled on the MR EP catheter was recorded inside the MR room.

3.3.3.1 Simulator experiments

The aim of this experiment was to test the functionality of catheter and whole ECG recording system and then record the coupled noise on the ECG signal. This helped to analyze the coupled noise and modified the experimental setup such that the coupled noise would be kept at the minimum level.

The experimental setup is given in Figure 3.24. In this experiment, an ECG simulator (Ferronato, Toledo, Spain) was used (Figure 3.25) to generate the ECG signal (Figure 3.25). This simulator has three outputs; V+, V- and G. Since our catheter was bipolar (had two electrodes), we shorted the V- and G signals and connected them to the ring electrode of the catheter. V+ signal of the simulator was connected to the tip electrode. The IECG signal was recorded by biopac MP 150 16 channel data acquisition system (Biopac, Goleta, CA) with ECG amplifier module. The IECG signal generated at the distal end of the catheter was transformed by the twisted pair to the SMA connector at the proximal end of the catheter. The ground signal coming from the ring electrode connected to the outer conductor of the connector and the positive signal coming from the tip electrode was connected to the inner conductor of the SMA. Then, this signal was transmitted to the ECG amplifier with low noise 3 mm coaxial cable (Siemens). As the ECG amplifier has three inputs (V+, V- and G), the V- signal was connected to both G and V- input and V+ signal was connected to the V+ input of the amplifier. The biopac data acquisition system was connected to the computer. The monitoring and processing of the ECG signal was achieved using the 4.1 software.

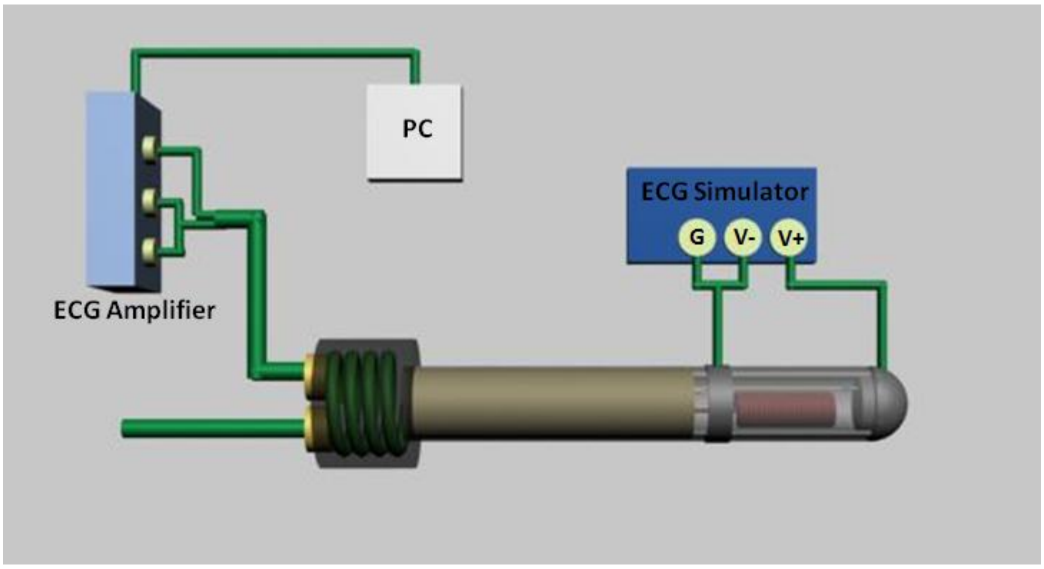

Figure 3.24: The diagram of the experimental setup used for ECG recording using ECG simulator.

Figure 3.25: A picture of the ECG simulator which was used to test the functionality of the complete system

The obtained ECG signal is shown in Figure 3.26-a. The graph of Fast Furrier Transform (FFT) of the signal is shown in Figure 3.27. It can be easily observed that there is too much high frequency noise coupled to the ECG signal. In order to get rid of the noise without degrading the ECG signal, we applied a LPF with 150 Hz cutoff frequency. The obtained ECG signal is shown in Figure

3.26-b. As can be observed in Figure 3.27, there is a high noise on 50 Hz and 100 Hz. Hence we applied a band stop filter to the signal at these frequencies and the resulting clear signal is shown in Figure 3.26-c.

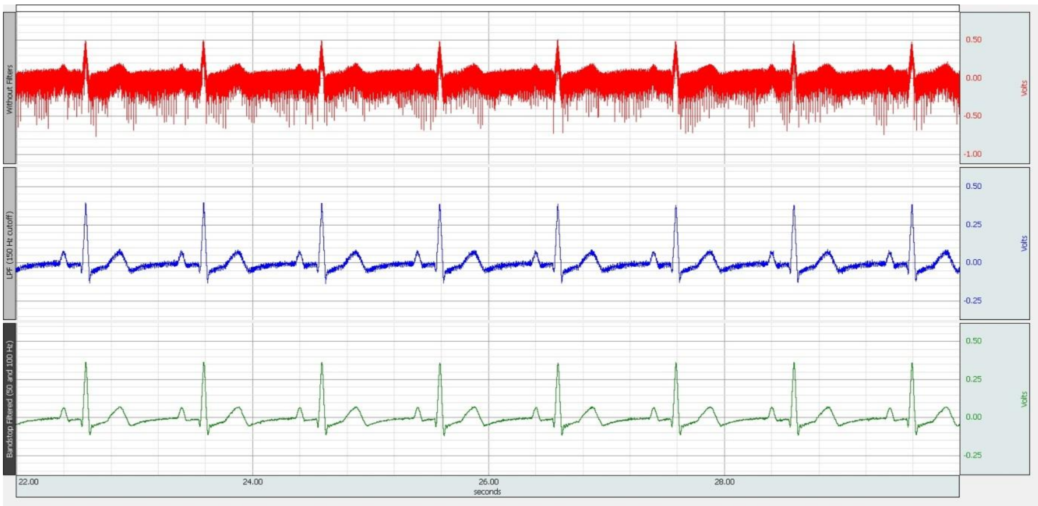

Figure 3.26: a: The original signal obtained using the ECG simulator.

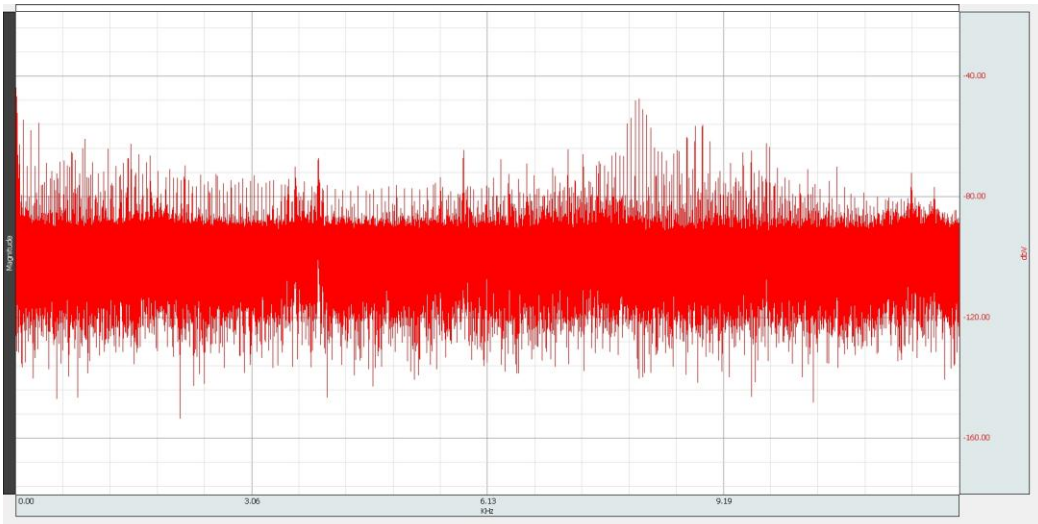

Figure 3.27: The graph of the frequency response of the original ECG signal obtained from ECG simulator.

3.3.3.2 Animal Experiment

The aim of this experiment is to test the functionality of the catheter in receiving the IECG signal. A rabbit experiment was conducted at the Bilkent University Molecular Biology and Genetics Department. A rabbit was initially anesthetized and the designed MR EP catheter was placed through the neck of the animal to the arteria and through this arteria to the right ventricle of the heart. The IECG signal was recorded using the same hardware as the one used in the simulator experiment. The obtained IECG signal is shown in Figure 3.28-a. In order to further clear the signal, we filtered it by an LPF with cutoff frequency of 150 Hz. The resulting noise level of the filtered signal was very low as can be seen in Figure 3.28-b.

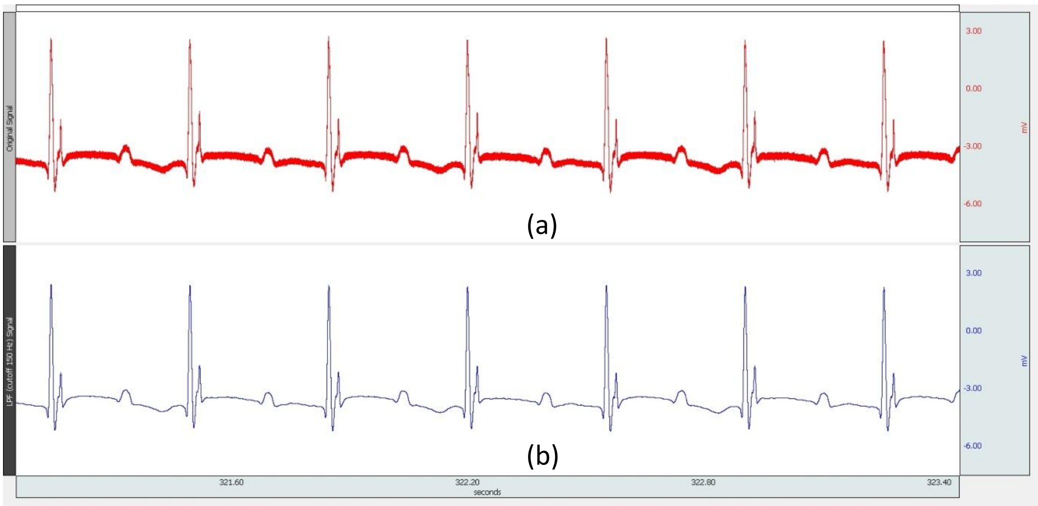

Figure 3.28: ECG signal obtained using the proposed MR EP measurement catheter. (a) The original signal. (b) The original signal filtered with LPF with 150 Hz cutoff frequency.

3.3.3.3 Noise Recording in MR Room

The aim of this experiment is to record the noise coupled to the catheter during the MR scan. The experimental setup is shown in Figure 3.29. The MR EP catheter was placed inside the gel phantom and the gel phantom was placed inside the MR scanner. An LPF was then placed at the proximal end of the catheter. The signal was transmitted to the penetration panel with a low noise 3 mm coaxial cable (Siemens), which was connected to the second LPF mounted into the penetration panel. In the control room, all the signals were transferred with the same coaxial cable. The signal coming from catheter was transmitted to the Biopac data acquisition system and connected to the ECG amplifier module.

Additionally, the output of the gradient signals on the main cabinet was connected to the biopac in order to simultaneously record the applied gradient waveform. Thereby, the catheter signal (noise) and three gradient signals (Gx, Gy and Gz) were recorded simultaneously.

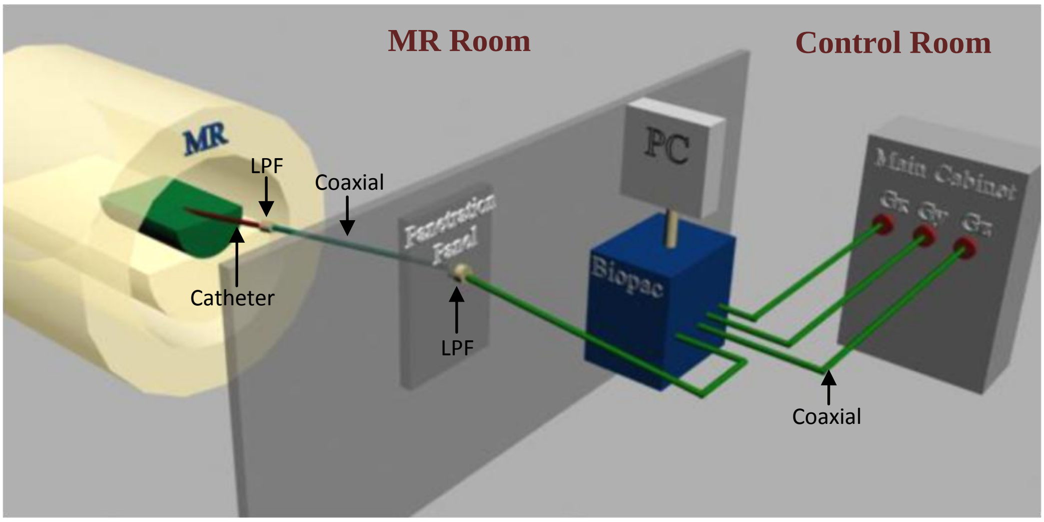

Figure 3.29: Experimental setup used for the noise recording during the MR scan.

The obtained signals (noise) were shown in Figure 3.30. It is observed that the coupled noise is very much correlated with the applied gradient fields as the noise is a combination of the derivatives of the gradient fields.

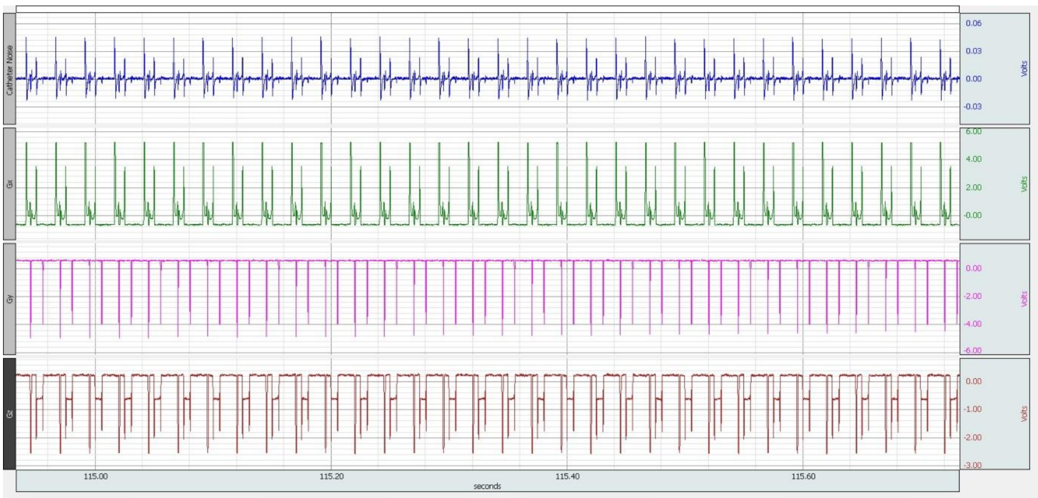

Figure 3.30: (A) The noise coupled to the MR EP catheter during the MRI. (B) Gradient field of x axis. (C) Gradient field of y axis. (D) Gradient field of z axis.

3.3.3.4 Analysis and Filtering of the Obtained IECG Signal

In order to observe the effect of the noise coupled to the catheter during the MRI, on the IECG signal, the noise was added to the IECG signal obtained from the rabbit heart. (The signals are shown in Figure 3.31). Figure 3.31-a shows the IECG signal recorded from the heart of the rabbit and Figure 3.31-b shows the noise coupled to the EP catheter during the MR scan. The sum of these two signals is given in Figure 3.31-c, where the effects of the gradient noise on this signal can be easily observed. In order to get rid of the coupled noise, the signal was filtered and the clean version of the IECG is given in Figure 3.31-d.

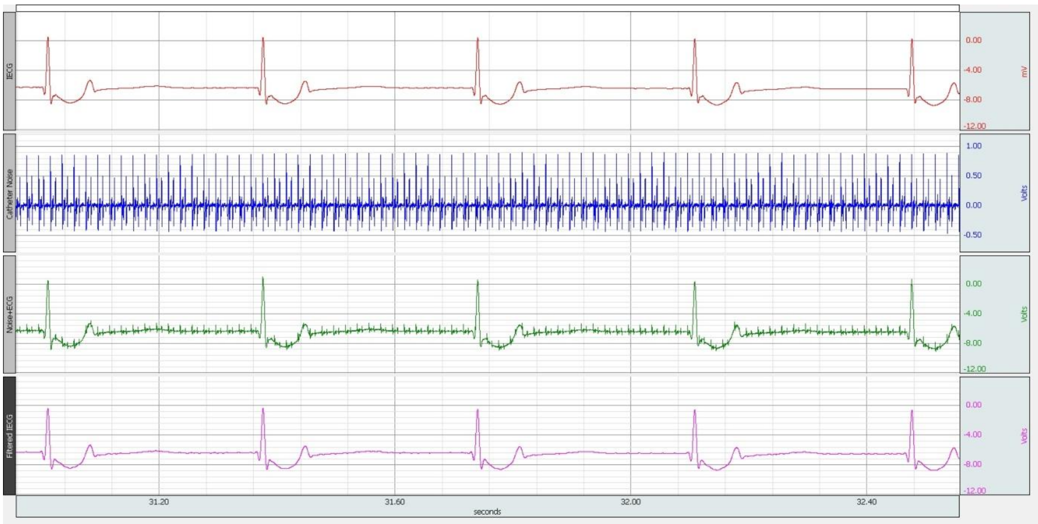

Figure 3.31: (a) An IECG signal obtained from the rabbit heart. (b) Noise coupled to the MR EP catheter during the MR imaging. (c) the summation of the signals given in (a) and (b). (d) The filtered version of the signal given in (c).

3.4 DISCUSSION

As the solenoid coil was manufactured from a superelastic material, the tip end of the MRI guidewire is very soft, which prevents the possibility of injuries or perforation of the target region. Also the solenoid coil was made up of gold and PTFE plated nitinol, which improves the imaging performance of the MRI guidewire. As the inner conductor of the coaxial portion of the MRI guidewire and solenoid coil was designed as a single piece material, there is no junction point between them, which decrease fragility of the device. Due to the absence of an additional decoupling and matching circuit, the size of the circuitry box at the proximal end of the MRI guidewire was reduced and the manufacturing of the GW becomes easier. Although, the quality of the images obtained by the MRI guidewire may be sufficient to navigate the guidewire in the human body and acquire high SNR images of the heart, plating the inner surface of the nitinol with gold or any other conductive material would decrease the resistance of the coaxial portion and consequently increase the SNR. Despite the superelasticity of the nitinol tube, it could be broken off during the application due to its small wall sizes. Thus, the wall size of the nitinol tube could be increased as a future work.

The electrodes are connected to the wire leads by the resistors, which prevent the induced current to flow to the body. Consequently, excessive heating is avoided with this design. Although this resistor works efficiently, there is still room for improvement in terms of stiffness. To this end, these resistors could be replaced with resistive wires. Also in our design we achieved minimized coupled noise by twisting the wire leads carrying the ECG signal. Finally, due to the absence of an additional matching and decoupling circuit, the electric circuitry box can be built in a smaller size without sacrificing the image quality. Although the functionality of the catheter in terms of imaging and IECG recording was proved with separate experiments, to truly evaluate the performance of the catheter, an animal experiment should be conducted to test these two functions simultaneously, under the MRI. Finally, for the clinical applications, both MRI guidewire and MR EP catheter need improvement in the liquid isolation.

3.5 CONCLUSION

In this chapter, development of an MRI guidewire and an MR EP catheter, which are used in the treatment of AF under the guidance of MRI, was explained. The MRI guidewire satisfies two criteria in the 0.9mm compact package. First, owing to the loopless antenna embedded inside, it enables navigation inside the body. Second the device shaft delivers interventional devices, which may be large and inflexible. The MR EP catheter also meets two different criteria. First, providing high SNR images of the heart chambers, it provides guidance in the creation of linear and continuous lesions during the RF ablation and at the same time it provides navigation of the catheter. Second, it records the IECG signal with minimum coupled noise.

In conclusion, we believe this technology contributes to the improvement of the interventional MRI as well as making the AF treatable under the guidance of MRI.

Chapter 4

4. CONCLUSION

In this study we designed and constructed novel MRI coils to be used for interventional procedures under the guidance of MRI. The first coil we developed is a two channel endocervical coil for the treatment of cervical cancer. Second, we developed an MRI Guidewire and MR EP catheter for the treatment of AF.

As the current imaging techniques don't provide sufficient imaging qualities, we developed a two channel endocervical coil, which was embedded into the brachytherapy applicator without interfering with its functions. It provides high SNR images of the cervix that is required for a more accurate radiation dose calculation in the treatment of cervical cancer with HDRB. The performance of this coil was tested with phantom experiments and the results proved that the design worked properly. For the better understanding of the performance of the coil, kiwi was used as a model of the cervix. The image of kiwi obtained with endocervical coil was compared with the images obtained with Siemens body matrix coil, which has been considered as the gold standard of cervix imaging. Although, the performance of the endocervical coil is better than Siemens body matrix coil, in order to increase signal intensity and achieve images of large FOV, it could be used in a combination with Siemens body matrix coil. Despite the fact that the anatomical details of the kiwi are much better observed in the image obtained with the endocervical coil, for the better understanding of the performance, animal experiments must to be conducted.

The most common method currently used in the AF treatment involves X-Ray fluoroscopy, which provides poor soft tissue contrast and evokes serious safety concerns due to the exposure to ionizing radiation. In order to develop an alternative method, which not only provides high soft tissue contrast but is also safe to use with no ionizing radiation, we designed MRI guidewire and MR EP catheter for the treatment of the AF. The MRI guidewire was designed in a way that it has similar physical properties with the common cardiovascular guidewires. The MR EP catheter, on the other hand, was designed to obtain clean IECG signal during the MR scan. Thanks to the loopless antenna embedded inside both of these catheters, they could be navigated in the body under the MRI. Since these catheters provide high SNR images of the heart, they can also be used to guide complex interventional procedures such as RF ablation. Even though the performance of these catheters was tested and confirmed with in vitro experiments, to fully understand its performance, animal experiments should be conducted.

To conclude, we hope that these two new technologies will play a significant role in the development of the interventional MRI and pave the way for the treatment of the two mortal diseases, cervical cancer and AF.

Bibliography

[1] O. Ocali, and E. Atalar, Intravascular Magnetic Resonance Imaging Using a Loopless Catheter Antenna. Magnetic Resonance in Medicine, 1997. 37(1): p. 112-118.

[2] A. Yung, Y. Oner, J. M. Serfaty, M. Feleney, X. Yang, E. Atalar, Phased array MRI of canine prostate using endorectal and endourethral coils, Magnetic Resonance in Medicine, 49(4) 710-715, 2003.

[3] Perez CA. Uterine cervix. In: Perez CA, Brady LW (eds.). Principles and practice of radiation
oncology. Philadelphia: Lippincott-Raven, 1997; 1733-834.

[4] Gerbaulet A, Lartigau E, Haie-Meder C, et al. Le Cancer du col uterin de la femme jeune.
Contracep Fertil Sex 1994; 22: 1-11.

[5] Bergeron C, Barrasso R, Beaudenon S, et al. Human papilloma viruses associated with
cervical intraepithelial neoplasia. Great diversity and distinct distribution in low- and high-grade
lesions. Am J Surg Pathol 1992; 16(7): 641-9.

[6] Barillot I, Horiot JC, Pigneux J, et al. Carcinoma of the intact uterine cervix treated with
radiotherapy alone: a French cooperative study: update and multivariate analysis of prognostic
factors. Int J Radiat Oncol Biol Phys 1997; 38: 969-78.

[7] Alain Gerbaulet, Richard Pötter, Christine Haie-Meder. Cervical Canser.

[8] Gerbaulet A et al. (2005). “General aspects”. İn Gerbaulet A, Pötter R, Mazeron J, Limbergen EV. The GEC ESTRO handbook of brachytherapy. Belgium: ACCO.

[9] Stewart Aj et al. (2007). “radiation concepts for brachytherapy”. İn Devlin P. Brachytherapy. Appications and Techniques. Philadelphia: LWW

[10] Kim SH, Choi BI, Han JK, Kim HD, HP, Kang SB, Lee JY, Han MC. Preoperative staging of uterine cervical carcinoma: comparison of CT and MRI in 99 patients. Journal of computer assisted tomography 1993;17(4):633-640.

[11] Wachter-Gerstner N, Wachter S, Reinstadler E, Fellner C, Knocke TH, Potter R. The impact of sectional imaging on dose escalation in endocavitary HDR-brachytherapy of cervical cancer: results of a prospective comparative trial. Radiother Oncol 2003;68(1):51-59.

[12] Haie-Meder C, Potter R, Van Limbergen E, Briot E, De Brabandere M, Dimopoulos J, Dumas I,Hellebust TP, Kirisits C, Lang S, Muschitz S, Nevinson J, Nulens A, Petrow P, Wachter- Gerstner N. Recommendations from Gynaecological (GYN) GEC-ESTRO Working Group(I): concepts and terms in 3D image based 3D treatment planning in cervix cancer brachytherapy with emphasis on MRI assessment of GTV and CTV. Radiother Oncol 2005;74(3):235-245.

[13] Viswanathan AN, Dimopoulos J, Kirisits C, Berger D, Potter R. Computed tomography versus magnetic resonance imaging-based contouring in cervical cancer brachytherapy: results of a prospective trial and preliminary guidelines for standardized contours. International journal of radiation oncology, biology, physics 2007;68(2):491-498.

[14] Krieger A et al., IEEE Transactions on Biomedical Engineering, 52(2):306-313 (2005).

[15] Quick HH, Ladd ME, Zimmermann-Paul GG, Erhart P, Hofmann E, von Schulthess GK, Debatin JF. Single-loop coil concepts for intravascular magnetic resonance imaging. Magn Reson Med 41:751-758, 1999

[16] http://encyclopedia2.thefreedictionary.com/Reciprocity+principle

[17] Simple Analytic Expressions for the Magnetic Field of a Circular Current Loop, James Simpson, John Lane, Christopher Immer, and Robert Youngquist, 2, 2001

[18] D. K. Cheng. Fundamentals of Engineering Electromagnetics. Pierson Edison Wesley, 1993.

[19] Balanis C. Advanced Engineering Electromagnetics. New York:Wiley;

[20] Thomas Lee, The design of CMOS Radio- Frequency Integrated Circuits, Cambridge University Press; 2004

[21] U.S. Department of Health and Human Services, Food and Drug Administration, Center for Devices and Radiological Health. Guidance for the Submission of Premarket Notifications for Magnetic Resonance Diagnostic Devices, November 14, 1998.

[22]C. Yeung, E. Atalar, RF Transmit Power Limit for the Barewire Loopless Catheter Antenna, J. Magnetic Resonance Imaging, Journal of Magnetic Resonance Imaging, 12:86-91, 2000.

[23] I. B. Akca, O. Ferhanoglu, C. J. Yeung, S. Guney, T. O. Tasci, E. Atalar, “Measuring Local RF Heating in MRI: Simulating Perfusion in a Perfusionless Phantom”, Journal of Magnetic Resonance Imaging 26(5):1228-1235, 2007.

[24] Celik H, Eryaman Y, Altintas A, Hafez IA, Atalar E. Evaluation of Internal MRI Coils using Ultimate Intrinsic SNR. Magn Reson Med 52:640-649, 2004.

[25] Mitchell, M.A., I.D. McRury, and D.E. Haines, Linear atrial ablations in a canine model of chronic atrial fibrillation: morphological and electrophysiological observations. Circulation, 1998. 97(12): p. 1176-85.

[26] Benjamin EJ, Wolf PA, D'Agostino RB, Silbershatz H, Kannel WB, Levy D (1998). "Impact of atrial fibrillation on the risk of death: the Framingham Heart Study". Circulation 98 (10): 946–52

[27] Rosamond, W., et al., Heart disease and stroke statistics--2007 update: a report from the American Heart Association Statistics Committee and Stroke Statistics Subcommittee. Circulation, 2007. 115(5): p. e69-171.

[28] Blackshear JL, Odell JA (February 1996). "Appendage obliteration to reduce stroke in cardiac surgical patients with atrial fibrillation". Ann. Thorac. Surg. 61 (2): 755–9.

[29] Cox, J.L. and T.M. Sundt, 3rd, The surgical management of atrial fibrillation. Annu Rev Med, 1997. 48: p. 511-23.

[30] Chiappini, B., R. Di Bartolomeo, and G. Marinelli, Radiofrequency ablation for atrial fibrillation: different approaches. Asian Cardiovasc Thorac Ann, 2004. 12(3): p. 272-7.

[31] Albert C. Lardo, Henry Halperin, Christopher Yeung, Pitayadet Jumrussirikul, Ergin Atalar and Elli ot McVeigh, Magnetic Resonance Guided Radiofrequency Ablation: Creation and Visualization of Cardiac Lesions. Lecture Notes in Computer Science, 1998, Volume 1496/1998, 189

[32] C. J. Yeung, R. C. Susil, E. Atalar, RF Heating due to Conductive Wires During MRI Depends on the Phase Distribution of the Transmit Field, Magnetic Resonance in Medicine 48:1096–1098, 2002

[33] Singer I. Interventional electrophysiology. Baltimore: Williams and Wilkins; 1997.

[34] B. Qiu, P. Karmarkar, C. Brushett, F. Gao, R. Kon, S. Kar, E. Atalar, X. Yang. Development of An 0.014-Inch Magnetic Resonance Imaging-Guidewire, Magnetic Resonance in Medicine, Vol 53, 986-990, 2005.

[35] R. C. Susil, C. J. Yeung, H. R. Halperin, A. C. Lardo, E. Atalar, Multifunctional Interventional Devices for MRI: A Combined Electrophysiology / MR Imaging Catheter, MRM 47(3):594-600, 2002

[36] Ozgur Kocaturk, Msc, Ann H. Kim, Christina E. Saikus, Michael A. Guttman, Anthony Z. Faranesh, Cengizhan Ozturk; Active Two-Channel 0.035" Guidewire for interventional Cardiovascular MRI. J. Magn. Reson. Imaging 2009;30:461-465

[37] Susil RC, Yeung CJ, Atalar E, "Intravascular extended sensitivity (IVES) MR imaging antennas." Magnetic Resonance in Medicine, 2003; 50(2): 383-390.

[38]Yiğitcan Eryaman Design and Implementation of Internal MRI coils Using Ultimate Intrinsic SNR 2007; MS Thesis Ankara Bilkent University